

On the evolution of small scale Cosmic structure

Dissertation der Fakultät für Physik
der
Ludwig-Maximilians-Universität München

vorgelegt von Liang Gao
aus Henan, China

München, den 1. October 2004

1. Gutachter: Prof. Dr. Simon D. M. White
2. Gutachter: Prof. Dr. Gerhard Börner

1. Gutachter: Prof. Dr. Simon D. M. White
2. Gutachter: Priv.-Dr. Gerhard Börner
Tag der mündlichen Prüfung: 1. Oktober 2004

Contents

Zusammenfassung (Summary in German)	3
Summary	5
1 Thesis objectives and framework	7
1.1 Motivation	7
1.2 The standard Cosmology	7
1.3 Linear and quasi-linear theory	9
1.3.1 Primordial density fluctuations and transfer function	9
1.3.2 Dynamics of linear perturbations	10
1.3.3 The Zel'dovich Approximation	11
1.3.4 The spherical "Top-Hat" Collapse	12
1.3.5 The statistics of hierarchical clustering	13
1.4 Nonlinear evolution	17
1.4.1 N -body simulation	17
1.4.2 Dark halo and subhalo	19
1.4.3 Galaxy Formation	20
1.5 Outline	21
2 The subhalo populations of ΛCDM haloes	27
2.1 Introduction	27
2.2 The Simulations	29
2.2.1 The GIF2 cosmological simulation	29
2.2.2 Higher resolution simulations of individual halos	30
2.3 The mass function of haloes	31
2.4 Subhalo populations	31
2.4.1 A convergence study of subhalo populations	31
2.4.2 Is the population of subhaloes similar in all haloes?	34
2.4.3 The mass fraction in subhaloes	38
2.4.4 Dependence of subhalo populations on halo concentration and formation time	39
2.4.5 The evolution of the subhalo mass function	41
2.4.6 The spatial distribution of subhaloes	43
2.5 The evolution of subhaloes	48
2.5.1 The history of present subhaloes	48
2.5.2 Mass loss from subhaloes as a function of time	48
2.5.3 The fate of accreted haloes	49

Contents

2.5.4	Radial dependence of accretion time and mass loss	51
2.6	Summary and discussion	52
3	Galaxies and subhaloes in ΛCDM galaxy clusters	61
3.1	Introduction	61
3.2	The Simulations and the Semi-analytic Model	62
3.3	Number density and velocity dispersion profiles for galaxies and subhaloes .	63
3.4	Summary and discussion	67
4	Earlier formation and later merging of the Giant Galaxies	71
4.1	Introduction	71
4.2	Formation of Mass Concentrations Characteristic of the Most Massive Galaxies	72
4.3	High Resolution Simulations of Massive Halo Assembly	74
4.4	Mergers and Relaxation at Low Redshifts	79
4.4.1	Rearrangements of the Dark Matter	79
4.4.2	The Distributions of Stars	81
4.4.3	The Attractor Hypothesis	84
4.5	Open Issues	88
5	The first structures in a CDM Universe	95
5.1	Introduction	95
5.2	Simulations details	96
5.2.1	The simulations	97
5.2.2	Halo finders	98
5.3	Large scale structure at high redshift	100
5.3.1	Morphology	100
5.3.2	Biased structure formation at high redshift	100
5.4	Evolution of massive halo structure and environment	102
5.4.1	Visualization	104
5.4.2	Density profile of dark haloes as a function a redshift	104
5.4.3	Properties of Substructure	104
5.5	Discussion	108
5.6	Concluding remarks	112
	Conclusion	117

Zusammenfassung

In dieser Arbeit verwenden wir eine Reihe von hochauflösenden kosmologischen N -body Simulationen, um die Bildung und Entwicklung von hochgradig nichtlinearen Objekten in unserem Universum zu untersuchen.

In Kapitel 2 beschäftigen wir uns mit der Systematik von Subhalo Populationen Dunkler Materie, deren Evolution wir hier zum ersten mal veranschaulichen können: ein beträchtlicher Teil der Masse der meisten Halos kam erst bei einer relativ niedrigen Rotverschiebung dazu, und dieser Massenzuwachs erfolgt in klumpiger Form mit einer Halomassenverteilung ähnlich jener des gesamten Universums. Da Tidal Stripping die Masse der Subhalos rasch reduziert, wird die Population bei jeder gegebenen Masse von Objekten dominiert, die erst kürzlich in den Halo gestürzt sind und die daher Vorgänger geringerer Masse (und somit höherer Häufigkeit) hatten. Die Umlaufbahnen erst kürzlich dazugekommener Halos verbringen die meiste Zeit im äußeren Halo, sodaß Subhalos einer gegebenen Masse deutlich weniger im Zentrum konzentriert sind, als die Gesamtheit der Dunklen Materie. Subhalos, die in der Nähe des Zentrums beobachtet werden, haben kürzere Umlaufperioden und müssen daher schon früher hineingestürzt sein. Sie behalten somit nur einen relativ kleinen Anteil ihrer ursprünglichen Masse. Unsere Ergebnisse weisen darauf hin, daß jeglicher Vergleich mit Galaxien in realen Galaxienhaufen nur möglich ist, wenn die Bildung der sichtbaren, Licht abstrahlenden Komponente geeignet modelliert wird.

In Kapitel 3 erweitern wir die Arbeit aus Kapitel 2 dahingehend, daß wir den Zusammenhang zwischen der Subhalo- und der Galaxienpopulation untersuchen, indem wir zehn hochauflösende Resimulationen von Dunklen Halos der Größe eines Galaxienhaufens mit semi-analytischen Galaxienbildungsmodellen kombinieren. Im Besonderen vergleichen wir Anzahldichten und Geschwindigkeitsprofile von Haufengalaxien mit denen von Subhalos. Während die Radialverteilung von Galaxien jener der Dunklen Materie folgt, ist die Verteilung der Subhalos viel weniger zum Zentrum hin konzentriert. Wir beobachten, daß es eine komplexe und stark ortsabhängige Beziehung gibt zwischen den Galaxien und den Subhalos in denen sie sich befinden. Diese Beziehung kann nur durch eine adäquate physikalische Behandlung des Galaxienbildungsprozesses korrekt modelliert werden.

In Kapitel 4 untersuchen wir den Aufbau der Dichtekonzentration im Zentrum von Λ CDM Halos. Die primäre Schlußfolgerung ist, daß die inneren Kerne von Galaxien durch mehrfache Verschmelzungen zu einem universellen Dichteprofil ihrer kollisionsfreien Mischung aus Sternen und Dunkler Materie tendieren. Unser Ergebnis könnten auch helfen, einige der scheinbaren Schwierigkeiten mit dem CDM Model der Strukturbildung zu lindern. Erstens könnte es im Prinzip das beobachtete Fehlen einer Spitze der Verteilung der Dunklen Materie im Zentrum von nahen Galaxien und Galaxienhaufen erklären. Zweitens würde es eine Übereinstimmung von mitbewegter Anzahldichte der massereichen Halos als

Funktion der Geschwindigkeitsdispersion mit SDSS Beobachtungen der Galaxienanzahl als Funktion der stellaren Geschwindigkeitsdispersion zulassen.

Im letzten Kapitel haben wir eine Reihe von N -body Resimulationen einzelner Halos bei verschiedenen Rotverschiebungen in einem *kosmologischen Volumen* $(0.68 \text{ Gpc})^3$ durchgeführt, mit dem Ziel, die ersten gebundenen Objekte aufzulösen, in denen die ersten Sterne in einem von kalter Dunkler Materie dominierten Universum geboren worden sein könnten. Unsere Simulationen haben erfolgreich seltene aber relativ massereiche Halos aufgelöst, wobei ein sehr weiter Rotverschiebungsbereich [$z = 80, z = 0$] mit ultrahoher Auflösung abgedeckt wurde. Die höchste davon in unserer letzten Stufe mit einer Teilchenmasse von $0.8 M_\odot$. Unsere ersten Resultate zeigen, daß die anfängliche Strukturbildung extrem stark zu überdichten Regionen hin beeinflußt war, und diese Bias Relation kann von der erweiterten Press-Schechter Theorie reproduziert werden. Die interne Struktur dieser frühen Halos ist jener ihrer Gegenstücke bei niedriger Rotverschiebung sehr ähnlich, allerdings ist der Fit mit einem NFW Profil weniger gut. Die Halomassenfunktion wurde bei den Rotverschiebungen $z \sim 50$ und $z \sim 30$ untersucht. Wir finden eine exzellente Übereinstimmung zwischen Vorhersage und Simulation. Da unser Simulationsvolumen keine kleine periodische Box ist, sind wir in der Lage, bei jeder gegebenen Rotverschiebung seltenere und massereichere Halos zu simulieren, als vorhergehende Arbeiten. Wir beobachten, daß effektives radiatives Kühlen von atomarem Wasserstoff in Halos unserer Simulation schon bei $z = 32$ stattfinden kann. Die Häufigkeit solcher Halos würde laut Vorhersage heute in mitbewegten Einheiten jener von Halos der Masse $10^{14} h^{-1} M_\odot$ entsprechen. Fall sich die ersten Sterne in einem Halo der Masse $10^6 M_\odot$ gebildet haben sollten, könnte eine große Anzahl Sterne schon bei $z \sim 45$ geboren worden sein, mit einer mitbewegten Häufigkeit vergleichbar jener von M_* Halos heute.

Summary

In this thesis, we use a variety of high resolution cosmological N -body simulations to study the formation and evolution of highly non-linear objects in our universe.

In Chapter 2, we study the systematics of dark matter subhalo populations. For the first time, we give a picture for the evolution of subhalo populations: a substantial fraction of the mass of most haloes has been added at relatively recent redshifts, and this mass is accreted in clumpy form with a halo mass distribution similar to that of the Universe as a whole. Since tidal stripping rapidly reduces the mass of subhaloes, the population at any given mass is dominated by objects which fell in recently and so had lower mass (and thus more abundant) progenitors. The orbits of recently accreted objects spend most of their time in the outer halo, so that subhaloes of given mass are substantially less centrally concentrated than the dark matter as a whole. Subhaloes which are seen near halo centre have shorter period orbits and so must have fallen in earlier. They thus retain a relatively small fraction of their initial mass. Our results suggest that any comparison with galaxies in real clusters is only possible if the formation of the luminous component is modelled appropriately.

Extending the work of Chapter 2, in Chapter 3 we study the relationship between the subhalo and the galaxy population by combining 10 high resolution resimulations of cluster-sized dark haloes with semi-analytic galaxy formation modelling. In particular, we compare the number density and velocity profiles of cluster galaxies and those of subhaloes. While the radial distribution of galaxies follows closely that of the dark matter, the distribution of dark matter subhaloes is much less centrally concentrated. We find there is a complex and strongly position-dependent relation between galaxies and the subhaloes in which they reside. This relation can be properly modelled only by appropriate physical representation of the galaxy formation process.

In Chapter 4, we study the assembly of the central cusps of Λ CDM haloes. The primary conclusion is that the inner cores of galaxies tend to a universal density profile for their collisionless mixture of stars and dark matter through multiple mergers. Our result may alleviate some apparent challenges to the CDM model for structure formation. Firstly, it could in principle explain the observed absence of a cusp in the central dark matter distribution of nearby galaxies and galaxy clusters. Secondly, it would allow consistency of the comoving number density of massive haloes as a function of velocity dispersion with SDSS observations of the counts of galaxies as a function of stellar velocity dispersion.

In the final Chapter, we have carried out a sequence of N -body resimulations of individual haloes at various redshifts within a *cosmological volume* $(0.68\text{Gpc})^3$ with the aim of resolving the first bound objects which could potentially host the first stars in a cold dark matter dominated universe. Our simulations succeed in resolving rare but relatively massive haloes spanning a very broad redshift range [$z = 80$, $z = 0$] with ultra-high resolution.

Summary

The highest resolution achieved in our final level simulation has a particle mass of $0.8M_{\odot}$ and a force softening of $\epsilon = 7.8\text{pc}$ in comoving units. Our results indicate that initial structure formation was extremely strongly biased to overdense regions, and that this can be well understood within the framework of extended Press-Schechter(EPS) theory. The internal structure of these early haloes are quite similar to their low redshift counterparts, although the NFW profile does not fit as well. The halo mass function is examined at redshift $z = 50$ and $z = 30$. We find an excellent agreement between the predictions and the simulations. Because our simulation volume is not a small periodic box we are able to simulate rarer and more massive halos at any given redshift than previous work. We find that bound-free cooling from atomic hydrogen can take place in haloes as early as $z = 32$ and that the comoving abundance of these halos is predicted to be the same as for $10^{14}h^{-1}M_{\odot}$ halos today. If the first stars did form in haloes with mass $\sim 10^6M_{\odot}$, a large number would be born already at $z \sim 45$ with a comoving abundance matching that of haloes with mass M_* today.

1 Thesis objectives and framework

Abstract

In this chapter we provide the relevant background for this thesis. The scientific objective for each project is presented in the last section.

1.1 Motivation

I have to admit I knew nothing about *scientific* Astronomy before I decided to pursue a PhD in Astrophysics. However something in my deep heart lured me. I had dreamt of being a theoretical cosmologist when I was in high school, where I constructed a model for our cosmology during a *biological* course. After some training in Physics I realized that my model was more philosophical than scientific and thus could never be proved or falsified. Thus I was happy when the opportunity arose to study scientific Cosmology.

In the current standard cosmological model, around 90 per cent of the matter content of our universe today is composed of dark matter, which we cannot detect directly. Nevertheless, there is firm dynamical evidence for its existence in galaxy halos, and even more direct evidence has now been added by the phenomenon of gravitational lensing which has now been detected around galaxies, and in the general mass field. This dark matter is believed to interact with other matter only by gravity. Without dark matter, the current structure of our Universe could not form. In the last twenty years progress in the both theoretical and observational Astronomy has lead to a “concordance” cosmological model of a flat Λ CDM universe. However there has been a growing controversy on the small scales where nonlinear dynamics and complex baryonic process dominate. My research in the past three years has mainly concentrated on investigation of such small scale and highly nonlinear objects. In what follows I give the most relevant theoretical background for the research presented in this thesis.

1.2 The standard Cosmology

The current standard cosmological model is based on the assumption that our universe is homogeneous and isotropic on large scales (roughly $> 100\text{Mpc}$). The space–time for such universe can be described by the Robertson–Walker Metric:

$$ds^2 = (cdt)^2 - a(t)^2 \left[\frac{dr^2}{1 - Kr^2} + r^2(d\theta^2 + \sin^2\theta d\phi^2) \right]. \quad (1.1)$$

Here c denotes the speed of light, (r, θ, ϕ) are the comoving spherical polar coordinate system, t denotes the proper time, $a(t)$ is expansion factor (often defined as unity today

1 Thesis objectives and framework

by convention), and the curvature parameter K is a constant which can be scaled in such a way so that it only take the values 1, 0 or -1 .

The assumption of the Robertson–Walker Metric results in enormous simplifications of Einstein’s field equations

$$\ddot{a} = -\frac{4\pi G}{3}a\left(\rho + \frac{3p}{c^2}\right) + \left[\frac{1}{3}\Lambda ac^2\right], \quad (1.2)$$

$$\dot{a}^2 = \frac{8\pi G\rho}{3}a^2 - \frac{kc^2}{a^2} + \left[\frac{1}{3}\Lambda a^2c^2\right]. \quad (1.3)$$

Here Λ is the cosmological constant which represents the vacuum energy. Simplifying equation(1.3) can be written as

$$H(a)^2 = \left(\frac{\dot{a}}{a}\right)^2 = \frac{8\pi G}{3}\rho + \frac{\Lambda}{3} - \frac{k}{a^2} \quad (1.4)$$

and is usually referred to *Friedman’s equation*. It indicates that the expansion of Universe is actually driven by a matter term, a cosmological constant term and a curvature term. $H(a)$ is the hubble parameter, which is time dependent and has a value $H_0 = 72 \pm 8$ km/s/Mpc (Freedman et al. 2001) at present. By convention, H_0 is usually parameterized as $H_0 = 100hkms^{-1}Mpc^{-1}$, where h is a dimensionless factor.

The matter content of the universe is usually expressed in terms of the critical density

$$\rho_c = \frac{3H(a)^2}{8\pi G}, \quad (1.5)$$

which allows the definition of three useful cosmological parameters:

$$\Omega_M = \frac{\rho}{\rho_c}, \quad \Omega_\Lambda = \frac{\Lambda^2c^2}{3H_0^2}, \quad \text{and} \quad \Omega_c = -\frac{kc^2}{R_0H_0^2}. \quad (1.6)$$

The latest Cosmic Microwave Background(CMB) experimental results by the *WMAP* collaboration (Spergel et al. 2003) suggest we are living in a flat universe with the following cosmological parameters: $\Omega_m = 0.29 \pm 0.087$, $\Omega_\lambda = 0.69 \pm 0.05$ and $\Omega_c \cong 0$. The expression for the critical density includes the Hubble parameter $H(t)$, thus it evolves with time. Today it has a value

$$\rho_{c0} \equiv 2.7755 \times 10^{11}h^2M_\odot Mpc. \quad (1.7)$$

It is convenient to introduce a new astrophysical variable called the redshift: $z(t) = 1/a(t) - 1$. The energy of photons emitted by distant sources is reduced by the expansion of the Universe, where more distant light results in higher redshift due to earlier emission. Thus redshift is often used as a time variable in Cosmology.

The second *Friedman equation* can then be transformed into

$$\frac{H^2(z)}{H_0^2} = \Omega_m(1+z)^3 + \Omega_k(1+z)^2 + \Omega_\Lambda. \quad (1.8)$$

If we know the values of the present–day density parameters of universe, we can integrate this equation to derive lookback time for the Universe:

$$t_0 - t_1 = H_0^{-1} \int_0^z (1+z_1)^{-2} [(1+z_2)^2(1+\Omega_M z_1) - z_1(2+z_1)\Omega_\lambda]^{-1/2} dz_1.$$

When $z = \infty$, this integration gives the age of our Universe. Results from the *WMAP* collaboration suggests our Universe is $13.4 \pm 0.3Gyr$ old.

1.3 Linear and quasi-linear theory

Our standard cosmological model assumes that structure in the universe originates from small amplitude quantum fluctuations imprinted as an initially homogeneous and isotropic *Gaussian random* field during an epoch of inflationary expansion shortly after the Big Bang. In this case, the linear density is completely determined by its power spectrum, or equivalently its two-point correlation function. When the fluctuations are small (i.e. density contrast $\delta\rho = (\rho - \bar{\rho})/\bar{\rho} \ll 1$) linear and quasi-linear theories are very powerful tools to study the formation and the evolution of large scale structure.

1.3.1 Primordial density fluctuations and transfer function

The initial perturbation spectrum is commonly assumed to be a power law,

$$P(k) = k^n, \quad (1.9)$$

where n can be considered an effective power index even when $P(k)$ is not a pure power law. For the special case where $n = 1$, i.e. for the Harrison-Zel'dovich scale-invariant spectrum, equation (1.9) has the property that the density contrast had the same amplitude on all scales when the perturbations come through the horizon. Proponents of the inflationary picture of the early Universe find that fluctuations with the Harrison-Zel'dovich spectrum occur rather naturally.

Inflation is believed to be produced by the dominant presence of a quantum scalar field which rolls slowly from a false to the true vacuum, maintaining an approximately constant energy density and causing the early Universe to expand exponentially for a brief period of time. Quantum fluctuations in the inflation field are thus blown to macroscopic scales. Models of inflation predict the general properties of the resulting fluctuation field: it has Gaussian distributed amplitudes and a near scale-invariant power spectrum.

The primordial power spectrum was believed to change during the evolution of the early universe until the end of the epoch of recombination by various processes including, growth under self-gravitation, the effects of pressure, and dissipative processes. In general, modes of short wavelength have their amplitudes reduced relative to those of long wavelength in this way. The overall effect can be encapsulated in the transfer function, $T(k)$, which gives the ratio of the later-time amplitude of a mode to its initial value:

$$P(k, z) = P_0(k)T^2(k)\frac{D(z)}{D(z_0)}, \quad (1.10)$$

Where

$$T(k) = \frac{\delta_k(z_0)}{\delta_k(z)D(z)}. \quad (1.11)$$

Here $D(z)$ is the linear growth factor extrapolated to the present to be discussed later in this chapter. The normalization redshift is arbitrary, so long as it refers to a time before any scale of interest has entered the horizon. Once we possess the transfer function it is a most valuable tool. The evolution of linear perturbations back to the surface of last scattering obeys the simple growth laws given in equation (1.10), and it is easy to see then how structure in the universe will have changed during the matter-dominated epoch.

1 Thesis objectives and framework

It is a challenge to calculate accurate results for transfer functions, mainly because we have a mixture of matter and relativistic particles. Accurate results require a solution of the Boltzmann equation to follow the evolution in detail. CMBFAST is commonly considered one of the best publicly available Boltzmann codes for this task (Sejank & Zaldarriaga 1996). There are also several fitting formulae available for the transfer function of the CDM model. One of the most widely used ones is given by Bardeen et al. (1986; BBKS)

$$T(k) = \frac{\ln(1 + 2.34q)}{2.34q} [1 + 3.89q + (16.1q)^2 + (5.46q)^3 + (6.71q)^4]^{-1/4}, \quad (1.12)$$

with $q = k/[(\Omega_{\text{CDM},0} + \Omega_{\text{B},0})h^2\text{Mpc}^{-1}]$.

To completely specify $P(k)$ we also need to fix its overall amplitude. For $P(k)$ with a given shape, the amplitude is fixed if we know the value of $P(k)$ at any k , or the value of any statistic that depends on $P(k)$. One historically popular prescription for normalizing a theoretical power spectrum involves the variance of the galaxy distribution when sampled with randomly placed spheres of radius R :

$$\sigma^2(R) = \frac{1}{2\pi^2} \int_0^\infty k^3 P(k) \tilde{W}(kR) \frac{dk}{k}, \quad (1.13)$$

where $\tilde{W}(x) = 2(\sin kR - kR \cos kR)/(kR)^3$ is the Fourier transform of a spherical top-hat filter with radius R . The value of $\sigma(R)$ derived from the distribution of normal galaxies is approximately unity in spheres of radius $R = 8h^{-1}\text{Mpc}$. Alternately, the normalization can be obtained by COBE or WMAP observations of the cosmic microwave background (CMB) anisotropy.

1.3.2 Dynamics of linear perturbations

The problem of the growth of small perturbations under gravity dates back to the work of Jeans (1902), who applied first order perturbation theory to study the instabilities in evolving clouds of gas in the context of a static background fluid. Since the evolution of dark matter in an expanding background behaves like collisionless fluid, Jeans theory can be easily extended to discuss the time evolution of perturbations in an expanding Universe. Here it is convenient to use the comoving coordinates, \mathbf{x} , defined as

$$\mathbf{r} = \mathbf{a}(\mathbf{t})\mathbf{x}. \quad (1.14)$$

The proper velocity, $\mathbf{u} = d\mathbf{r}/d\mathbf{t}$, at point \mathbf{x} can then be written as

$$\mathbf{u} = \dot{\mathbf{a}}(\mathbf{t})\mathbf{x} + \mathbf{v}, \quad \mathbf{v} = \mathbf{a}\dot{\mathbf{x}}. \quad (1.15)$$

where \mathbf{v} is the peculiar velocity describing the motion of the fluid relative to the fundamental observer (one comoving with the background) at \mathbf{x} . We can also express the density, ρ , in terms of the density perturbation against the background,

$$\rho(\mathbf{x}, \mathbf{t}) = \bar{\rho}(\mathbf{t})[1 + \delta(\mathbf{x}, \mathbf{t})]. \quad (1.16)$$

The time evolution of an ideal fluid is given by the equation of continuity (which describes mass conservation), Euler's equation (the equation of motion), and Poisson's equation (describing the gravitational field):

$$\frac{\partial \delta}{\partial t} + \frac{1}{a} \nabla \cdot [(1 + \delta) \mathbf{v}] = 0, \quad (1.17)$$

$$\frac{\partial \mathbf{v}}{\partial t} + \frac{\dot{a}}{a} \mathbf{v} + \frac{1}{\mathbf{a}} (\mathbf{v} \cdot \nabla) \mathbf{v} = -\frac{\nabla \phi}{\mathbf{a}} - \frac{\nabla \mathbf{P}}{\mathbf{a} \bar{\rho} (1 + \delta)}, \quad (1.18)$$

$$\nabla^2 \phi = 4\pi G \bar{\rho} a^2 \delta. \quad (1.19)$$

where $\nabla \equiv \nabla_x$ and $\partial/\partial t$ is in *Eulerian space*, ϕ denotes the potential, $\bar{\rho}$ is the mean background density.

In cases where both δ and \mathbf{v} are small and pressure is negligible, so that the nonlinear terms in the above equations can be neglected, we obtain:

$$\ddot{\delta} + 2a\dot{\delta} = 4\pi G \bar{\rho} \delta. \quad (1.20)$$

The solutions of equation(1.20) depend on the cosmological model relative to which the perturbations are defined. For the simplest matter-dominated Einstein-de sitter universes, one can obtain the exact result which has two modes, one growing,

$$\delta_+ \propto t^{2/3}, \quad (1.21)$$

and the other decaying,

$$\delta_- \propto t^{-1}. \quad (1.22)$$

The general growing solution $D(t)$ for all dust cosmogonies is given by integration

$$D(z) = H(z) \int_z^\infty dz \frac{1+z}{H^3(z)}. \quad (1.23)$$

$D(z)$ is usually referred to as the growth factor. Given a density field of perturbations, $\delta_0(x, z_0)$, its late time growth is determined by the growth factor as long as $\delta \ll 1$

$$\delta(x, z) = \delta_0(x, z_0) \frac{D(z)}{D(z_0)}. \quad (1.24)$$

1.3.3 The Zel'dovich Approximation

Once the fluctuation evolves into the non-linear regime ($\delta \gg 1$), the linear growth theory discussed above breaks down. Although the full development of the gravitational instability cannot be solved exactly without resorting to numerical simulations, there are some very useful special cases and approximations that can help us to understand the general case. As a first-order *Lagrangian* perturbation theory, the Zel'dovich approximation can be used in the development of perturbations into the non-linear regime. Rather than working out the development of the perturbation in some external *Eulerian* reference frame, the motion of particle's in a comoving coordinate frame is followed. If we denote \mathbf{x} and \mathbf{r} as the proper

1 Thesis objectives and framework

and comoving position vectors of the particles of the fluid, the Zel'dovich approximation can be written

$$\mathbf{x} = \mathbf{a}(t)\mathbf{r} + \mathbf{b}(t)\mathbf{P}(\mathbf{r}) . \quad (1.25)$$

The first term on the right-hand side describes the uniform expansion of the background model and the second term the perturbations as a function of the particles *Lagrangian* coordinate \mathbf{r} . In the coordinate system of the principal axes of the local distortion tensor, the motion of the particles in comoving coordinates can be described by a deformation tensor D :

$$D = \begin{bmatrix} a(t) - \alpha b(t) & 0 & 0 \\ 0 & a(t) - \beta b(t) & 0 \\ 0 & 0 & a(t) - \gamma b(t) . \end{bmatrix} \quad (1.26)$$

Mass conservation requires the density ρ in the vicinity of any particle to satisfy

$$\rho[a(t) - \alpha b(t)][a(t) - \beta b(t)][a(t) - \gamma b(t)] = \bar{\rho}a^3(t) . \quad (1.27)$$

Here $\bar{\rho}$ is the mean density of matter in the Universe. In the case of $\alpha > \beta > \gamma$, collapse occurs most rapidly along the x -axis and the density becomes infinite when $a(t) - \alpha b(t) = 0$. At this point, the ellipsoid will have collapsed to a pancake and the solution breaks down for later times. Although the density becomes formally infinite in the pancake, the surface density remains finite, and so the solution still gives the correct result for the gravitational potential at points away from the caustic surface. The results of numerical N-body simulations have shown that the Zel'dovich approximation is remarkably effective in describing the evolution of the non-linear stages of the collapse of large scale structures up to the point at which caustics are formed (Coles et al. 1993).

The advantage of the Zel'dovich approximation is that it normally breaks down later than Eulerian linear theory. This method is usually used to set up initial conditions for cosmological simulations.

1.3.4 The spherical ‘‘Top-Hat’’ Collapse

The spherical ‘‘Top-Hat’’ collapse model is a simple and useful approximation to study the nonlinear evolution of the cosmic density field. For a spherical perturbation in the expanding Universe, the *Eulerian* radius R of a mass shell which had initial *Lagrangian* radius R_0 and mean linear overdensity δ_0 is given by

$$\frac{R(z)}{R_0} = \frac{1+z}{5/3|\delta_0|} \frac{(1 - \cos \theta)}{2} , \quad (1.28)$$

$$\frac{1}{1+z} = \left(\frac{3}{4}\right)^{2/3} \frac{(\theta - \sin \theta)^{2/3}}{0.6|\delta_0|} , \quad (1.29)$$

Where δ_0 denotes the initial density δ_{init} extrapolated to the present time given by equation (1.24). In the case $\delta_{\text{init}} < 0$, then $(1 - \cos \theta)$ should be replaced by $(\cosh \theta - 1)$ and $(\theta - \sin \theta)$ by $(\text{sinc} \theta - \theta)$.

In the spherical collapse model, initially overdense regions begin their collapse at $\theta = 0$, turn around at $\theta = \pi$, and collapse completely at $\theta = 2\pi$. With the above equations, the size of an overdense region evolves as

$$\frac{R_0}{R(z)} = \frac{6^{2/3} (\theta - \sin \theta)^{2/3}}{2 (1 - \cos \theta)}. \quad (1.30)$$

At the point of turnaround the overdensity is given by $\delta = (R_0/R_z)^3 - 1 = (3\pi/4)^2 - 1 \sim 4.55$. The final size at collapse is infinite, and so the density of this region is infinite as well. In practice the region virialises at some non-zero size rather than collapsing to infinite density. The average density within the virialized object is usually estimated by assuming that the object virializes at half the value of the turn around radius in physical units. This occurs when the density reaches

$$\Delta_{\text{vir}} = 18\pi^2 \simeq 178 \quad (1.31)$$

times the density of the background at virialization.

According to equation (1.28), the extrapolated linear overdensity of such a collapsed object would have had a critical value, δ_{sc} , given by

$$\frac{\delta_{\text{sc}}(z)}{1+z} = \frac{3}{5} \left(\frac{3\pi}{2} \right)^{2/3} \simeq 1.686, \quad (1.32)$$

at the moment of collapse. Thus, a collapsed object is one in which the initial overdensity, extrapolated using linear theory to the time of collapse, was $\delta_{\text{sc}}(z)/D(z) = 1.686$. At this time, the actual overdensity is about 178. That is the reason that the bound objects (dark haloes) in N -body simulations are usually defined as spherical regions with overdensity 178 times the cosmic mean.

1.3.5 The statistics of hierarchical clustering

1.3.5.1 The Mass Function

In the Cold Dark Matter scenario, galaxies and larger scale structures are built up by the process of hierarchical clustering. A simple but quite useful description of this process was first developed by Press & Schechter (1974). Their objective was to provide an analytic formalism for the process of structure formation once the density perturbations had reached such an amplitude that they could be considered to have formed virialized objects.

Recall that the primordial density perturbations are believed to be *Gaussian fluctuations*. Thus the phases of the waves which make up the density distribution are random and the distribution of the amplitudes of the perturbations of a given mass M can be described by a Gaussian function

$$p(\delta) = \frac{1}{\sqrt{2}\sigma(M)} \exp\left[-\frac{\delta^2}{2\sigma^2(M)}\right], \quad (1.33)$$

where $\delta = \delta\rho/\rho$ is the density contrast associated with perturbations of mass M . For a Gaussian distribution, the mean value is zero and the variance, $\sigma^2(M)$, i.e the mean square fluctuation, is

$$\langle \delta^2 \rangle = \left\langle \left(\frac{\delta\rho}{\rho} \right)^2 \right\rangle = \sigma^2(M), \quad (1.34)$$

1 Thesis objectives and framework

Thus at a given time t , the fraction of points which are surrounded by a sphere of radius R , within which the mean overdensity exceeds δ_c is given by

$$f(\delta > \delta_c) = \frac{1}{2} \left[1 - \operatorname{erf} \left(\frac{\delta_c}{\sqrt{2}\sigma(R)} \right) \right] \quad (1.35)$$

Press & Schechter suggested that this fraction be identified with the fraction of particles which are part of collapsed lumps with masses exceeding $M = 4\pi\bar{\rho}a^3R^3/3$. There is, however, a problem here. As $M \rightarrow 0$, then $\sigma(R) \rightarrow \infty$ and thus $f \rightarrow 1/2$. This formula thus predicts that only half of the particles are parts of lumps of any mass. Press & Schechter solved this by multiplying the mass fraction by an arbitrary factor of 2. The number density of collapsed lumps with mass in the range $M \rightarrow M + dM$ is then

$$n(M, t) = -2 \frac{\bar{\rho}}{M} \frac{\partial F_{1/2}}{\partial R} \frac{dR}{dM} dM \quad (1.36)$$

$$= -\sqrt{\frac{2}{\pi}} \frac{\bar{\rho}}{M} \frac{\delta_c(t)}{\sigma^2} \exp\left[-\frac{\delta_c^2(t)}{2\sigma^2}\right] dM \quad (1.37)$$

where $\delta_c(t) = \delta_c/D(t)$ is the critical overdensity linearly extrapolated to the present time.

A substantially better fit to mass function in N -body simulation is obtained if the error function in equation(1.35) is replaced by a function of slightly different shape. Sheth & Tormen (1999) suggested the following modification:

$$n(M, z)dM = A \left(1 + \frac{1}{\nu'^{2q}} \right) \sqrt{\frac{2}{\pi}} \frac{\bar{\rho}}{M} \frac{d\nu'}{dm} \exp\left(-\frac{\nu'^2}{2}\right) dM \quad (1.38)$$

where $\nu' = \sqrt{a}\nu$, $a = 0.707$, $A = 0.322$ and $q = 0.3$. In a detailed comparison with a wide range of simulations, Jenkins et al. (2001) confirmed that the model is indeed a good fit providing that haloes are defined at the same density contrast relative to the mean in all cosmologies. However, Jenkins et al. (2001) point out that the Sheth & Tormen formula does overestimate the number density of extremely rare objects, a more accurate fitting formula is given in their paper.

1.3.5.2 The extended Press–Schechter theory

Bond et al. (1991) developed an alternative approach based on excursion sets to derive the Press & Schechter formulism, which gives an analytic explanation to the original arbitrary factor of 2 in equation (1.36). An advantage of the excursion sets approach is that it provides a description of how a collapsed object was built up by the accretion and merger of smaller objects.

Consider a spherical region of mass M_2 with linear overdensity $\delta_c/D(t_2)$ that forms a collapsed object at time t_2 . By this approach, the fraction of M_2 that was in collapsed objects of certain mass at an earlier time $t_1 < t_2$ is given by

$$f(S_1, D_1 | S_2, D_2) dS_1 = \frac{1}{\sqrt{2\pi}} \frac{\delta_1 - \delta_2}{(S_1 - S_2)^{3/2}} \exp\left[-\frac{(\delta_1 - \delta_2)^2}{2(S_1 - S_2)}\right] dS_1, \quad (1.39)$$

Where $S_1 = \sigma^2(M_1)$, $S_2 = \sigma^2(M_2)$, $\delta_1 = \delta_c/D(t_1)$, and $\delta_2 = \delta_c/D(t_2)$. The formulae give the fraction of material in objects of mass M_2 at time t_2 which were in objects of mass M_1 at the earlier time t_1 . The mass distribution of the progenitors of objects of mass M_2 is therefore

$$n(M_1, t_1 | M_2, t_2) dM_1 = \frac{M_2}{M_1} f(S_1, D_1 | S_2, D_2) \frac{dS_1}{dM_1} dM_1. \quad (1.40)$$

There is also a conditional mass function corresponding to ellipsoidal collapse (Sheth & Tormen 2002), the conditional probability is replaced by the following formula:

$$f_{S_1}(S_1, D_1 | S_2, D_2) dS_1 = \frac{|T(S_1, D_1 | S_2, D_2)|}{\sqrt{2\pi}(S_1 - S_2)^{3/2}} \times \exp \left\{ -\frac{[B(S_1, D_1) - B(S_2, D_2)]^2}{2(S_1 - S_2)} \right\} dS_1, \quad (1.41)$$

and

$$T(S_1, D_1 | S_2, D_2) = \sum_{n=0}^5 \frac{(S_2 - S_1)^n}{n!} \frac{\partial^n [B(S_1, D_1) - B(S_2, D_2)]}{\partial S_1^n}, \quad (1.42)$$

where the moving barrier $B(S, z) = \sqrt{aS_*} [1 + \beta(S/aS_*)^\alpha]$ with $S_* \equiv \delta_c^2(z)$. The parameters are obtained from fitting the mass function to N-body simulations, $a = 0.707$, $\alpha = 0.485$, $\beta = 0.615$. Sheth & Tormen (2002) argued that this is an improved fit to simulation data. However, their formalism is somewhat arbitrary in the sense that the series in equation(1.42) is not well motivated and the parameters of the model are adjusted by comparison with N -body simulations rather than derived from their theory.

1.3.5.3 Spatial clustering and Bias

The PS formalism only provides the mass distribution for the bound objects (dark haloes). It contains no any information about the spatial distribution of these objects. Extending this theory, Mo & White (1996) constructed a model for the spatial clustering of dark haloes.

The basic mechanism of clustering bias is that an object of given mass will collapse earlier if it lies in a region of large-scale overdensity, leading to an enhanced abundance of haloes in such regions with respect to the mean.

In deriving the conditional probability equation (1.39 and 1.40), it is not necessary that M_2 itself be a halo; in fact this equation holds even if M_2 is an uncollapsed spherical region. In this case, equation (1.40) can be interpreted as the average number of M_1 haloes identified at redshift z_1 in a spherical region with comoving radius $R_0 = (3M_2/4\pi\bar{\rho})^{1/3}$ and density contrast δ_0 . The overdensity of haloes in such region is

$$\delta_h^L(1|2) = \frac{N(1|2)}{n(M_1, z_1)} V_L - 1 \quad (1.43)$$

where $V_L = \frac{4\pi}{3} R_0^3$ and $N(M_1, z_1)$ is the mean number of halos of given mass at redshift z_1 . This expression becomes particularly simple when $M_0 \gg M_1$ (so that $S_0 \ll S_1$) and $\delta_0 \ll \delta_1$:

$$\delta_h^L(1|2) = \frac{\nu_1^2 - 1}{\delta_1} \delta_0, \quad \text{where } \nu_1 = \frac{\delta_1}{\sqrt{S_1}} \quad (1.44)$$

1 Thesis objectives and framework

here $\delta_1 = \delta_c/D(t_1)$ and δ_0 is the linear density contrast linearly extrapolated to the present time. This expression gives the over-abundance of haloes in *Lagrangian space*.

It is more convenient to model the clustering of dark haloes at given redshift in *Eulerian space*, since most quantities are measured in *Eulerian space*. Then one must be able to calculate their expected abundance in spheres which at the desired redshift z have radius R and non-linear overdensity δ . Based upon the spherical collapse model, Mo & White(1996) derived an analytical formulae which relates the nonlinear overdensity to the linear overdensity in Lagrangian space. Although their derivation was for an *Einstein-de Sitter* Universe, Sheth & Tormen later confirmed that it is reasonably accurate for all cosmologies (Sheth & Tormen, 2002).

$$\delta_0(\delta, z_0) = \frac{\delta_{sc}(z_0)}{1.68647} \times \left[1.68647 - \frac{1.35}{(1+\delta)^{2/3}} - \frac{1.12431}{(1+\delta)^{1/2}} + \frac{0.78785}{(1+\delta)^{0.58661}} \right] \quad (1.45)$$

With the above assumptions, the average overdensity of dark haloes in spheres with current radius R and current mass overdensity δ_c can be expressed as:

$$\delta_h(1|2) = \frac{N(1|2)}{n(M_1, z_1)V} - 1, \quad (1.46)$$

where $V = 4\pi R^3/3$, $R_0 = R(1+\delta)^{1/3}$, and δ_0 is determined from the nonlinear overdensity δ . When $R_0 \gg R_1$ and $|\delta_0| \ll \delta_1$, we have

$$\delta_h(1|2) = b_h(M_1, z_1)\delta = \left(1 + \frac{\nu_1^2 - 1}{\delta_1}\right)\delta \quad (1.47)$$

Here $b_h(M_1, z_1)$ is the bias factor at time t for haloes identified at time t_1 . Thus, the over-abundance of haloes is enhanced with respect to the background mass overdensity δ by a factor b_h , and this which depends both on the mass M_1 and the time t_1 when they are identified. We call b_h the linear bias relation for haloes. Haloes with mass $M_1 > M_*$ are biased ($b_h > 1$), while haloes with $M_1 < M_*$ are anti-biased ($b_h < 1$), relative to the mass density field.

As first pointed out by Jing (1998), the original Mo & White (1996) formula suffer from similar inaccuracies to the original PS mass function, and indeed the two discrepancies are closely related. A more precise formula can be obtained from the ellipsoidal collapse model (Sheth, Mo & Tormen 2001):

$$b = 1 + \frac{1}{\delta_c} \left[\nu'^2 + b\nu'^{2(1-c)} - \frac{\nu'^{2c}/\sqrt{a}}{\nu'^{2c} + b(1-c)(1-c/2)} \right], \quad (1.48)$$

where $\nu' = \sqrt{a}\nu$, $a = 0.707$, $b = 0.5$ and $c = 0.6$. Numerical simulations show that this revision is substantially more accurate than its spherical counterpart, especially for haloes with $M < M_*$. We will discuss biased clustering for the bound objects at early redshifts in Chapter 5.

1.4 Nonlinear evolution

1.4.1 N -body simulation

As mentioned above, for the full treatment of nonlinear evolution, we must resort to numerical simulation. Currently, N -body simulation is becoming a more and more important and powerful tool for understanding the formation and evolution of structure in the nonlinear regime. According to the standard cosmology model, over 90 percent of matter in our universe is dark matter, which is believed to interact with other matter only via gravity. Therefore, the gravitational interaction produced by the dark matter component is the dominant action influencing structure formation in our Universe, especially on large scales.

In cosmological N -body simulations, the dark matter is usually represented by particles. These are evolved forward in time by Newton's laws written in comoving coordinates

$$\frac{d\mathbf{x}}{dt} = \frac{1}{a} \mathbf{v}, \quad (1.49)$$

$$\frac{d\mathbf{v}}{dt} + H\mathbf{v} = -\nabla\phi, \quad (1.50)$$

$$\nabla^2\phi = -4\pi Ga[\rho(\mathbf{x}, \mathbf{t}) - \bar{\rho}], \quad (1.51)$$

1.4.1.1 Initial conditions

Initial conditions for large scale cosmological simulations are usually constructed by imposing perturbations on an initially uniform state represented by a “glass” or grid distribution of particles. The glass configuration was invented by White (1993). First, particles are placed randomly within the computational box. The cosmological N -body integrator is then used to follow their motion but with the sign of Newton's constant changed when calculating peculiar gravitational forces. After some time, the initial poisson distribution relaxes to a “glass” like distribution where the force on each particle is very close to 0, and this state shows no discernible order or anisotropy on scales beyond a few interparticle separations. The merit of the glass distribution is that it has no preferred direction of the kind present in a grid distribution. Once an initially uniform distribution of particles has been produced, fluctuations are imposed using the algorithm described in Efstathiou et al. (1985). Based on the Zel'dovich approximation, a Gaussian random field is set up by perturbing the positions of the particles and by assigning them velocities according to the growing mode solution of linear theory.

When one is interested in the formation and evolution of individual objects, extremely high resolution may be required, and large-scale cosmological simulation appears too expensive. The most economical approach to this task is to use resimulation techniques. Firstly, one needs to run a large-scale coarse-resolution simulation. Then one selects the interesting object to be studied further in detail, all particles belonging to the object and its immediate environment are traced back to the initial *Lagrangian* space. The region containing all these particles is then filled with a homogenous distribution of higher resolution particles. These particles are then perturbed using the waves of the parent simulation,

1 Thesis objectives and framework

together with the extra high frequency waves needed to fill out the power spectrum between the Nyquist frequencies of the old and new simulations. The regions outside the high resolution regions are coarsely sampled with degraded resolution in order to represent the large-scale tidal fields acting on the object of interest.

1.4.1.2 The codes

The central problem of N-body numerical simulation lies in the computational algorithm used to compute the gravitational force. Evaluating the forces by direct summation over all particle pairs is prohibitive for simulations involving huge numbers of particles. Fortunately, there are available quite a variety of much more efficient algorithms.

An older, widely used gravity solver is the particle-mesh (*PM*) algorithm. In this scheme, the forces are determined by assigning mass points to a regular grid and then solving Poisson's equation on it. The use of a regular grid with periodic boundary conditions naturally allows using Fast Fourier Transform (*FFT*) methods to recover the potential, and this results in a substantial increase in speed. A weakness with this method is the relatively poor force resolution on small scales due to the finite spatial size of the mesh. A hybrid "particle-particle-particle mesh" (*P³M*) method, was developed to fix this problem. It solves the short range force directly (*PP*) but uses the mesh to compute the longer range component (*PM*); Thus, the short-range resolution of the algorithm is improved by adding a correction to the mesh force, while keeping the speed of the longer range force calculation. The advantage of this algorithm is that it is quite efficient in estimating the force when particle sets are lightly clustered, and it has the relatively light memory requirements. Thus it was widely used for the last generation of cosmological simulations which needed to evolve large numbers of particles on computers with relatively less memory than available today. For example, a *P³M* code, HYDRA, was used to carry out one of the largest published cosmological simulations, the 1 billion particle Hubble Volume Simulations, performed by the Virgo consortium in 1998 (Evard et al. 2001) on the Cray T3E super computer. However, with the recent developments in computer hardware, memory is no longer a bottleneck for cosmological applications. Thus, the *P³M* algorithm is less used today.

An alternative gravity solver is the Barnes-Hut tree algorithm. This method divides space recursively into a hierarchical cells, each containing one or more particles. If a cell of size s and distance d (from the point where \mathbf{g} is to be computed) satisfies $s/d < \theta$ the particles in this cell are treated as one pseudo-particle located at the center of mass of the cell. Computation time is saved by replacing the set of particles by a low-order multipole expansion due to the distribution of mass in the cell. The advantage of the tree algorithm is that it is fully spatially adaptive, since the hierarchical tree automatically refines its resolution where needed, and hence it is efficient for highly clustered simulations. The main drawback of the tree algorithm is its relatively large memory requirement and its inefficiency in lightly clustered simulations. Hence it has only been widely used for high resolution simulation of individual objects. Currently, a technique exploiting the merits of both the *PM* and the tree algorithm is becoming fashionable for cosmological simulations. The long range force is computed by *PM*, whilst the short range force is computed by a traditional tree algorithm, thus it is quite efficient in both heavily and lightly clustered regimes.

For this thesis, the subhalo project presented in Chapter 2 uses a combination of a *P3M* based gravity solver HYDRA (Couchman et al. 1985) and a pure tree code GADGET-1.1; for the on the formation of the first structures presented in Chapter 5, the *TREE-PM* code GADGET-2.0(Springel 2004) is extensively used.

1.4.2 Dark halo and subhalo

One of the direct applications of dark matter simulations is to study the highly non-linear internal structure of dark matter haloes. A halo is often defined as a virialised system which has mean density 200 times the critical density of the universe, as suggested by “top-hat” spherical collapse model. Regardless of the detailed initial conditions, numerous high resolution simulations agree on that the radial mass distribution of dark haloes follows closely a universe profile (Navarro, Frenk & White 1996, 1997).

$$\frac{\rho(r)}{\rho_{crit}} = \frac{\delta_c}{(r/r_s)(1+r/r_s)^2} \quad (1.52)$$

Here r_s is a characteristic radius where the logarithmic profile slope is -2 , δ_c is a characteristic density. The *NFW* profile, with its logarithmic slope changing gradually from -1 near the centre to -3 at large radii, is close to $\rho \propto r^{-2}$ in the intermediate range of radius. However, whether the asymptotic inner dark matter density profile slope is $\rho \propto r^{-1}$ or $\rho \propto r^{-1.5}$ (as advocated by Moore et al. 1998) is still a matter of debate. The latest simulations from the different groups show dark halo inner profile with slopes at $r \sim 0.1r_s$ which vary from $\beta(r) = -1.1$ to $\beta(r) = -1.4$ (Navarro et al. 2003; Reed et al. 2003; Diemand et al. 2004). The inner profile of dark matter halos has particular interest since it may allows to constrain models for the dark matter. In Chapter 4, we will discuss the assembly of the central cusp of Λ CDM clusters.

High resolution N-body simulations indicate that the halo concentration parameter, $c = r_{200}/r_s$ is correlated with halo mass; at fixed halo mass, the value of c depends on halo formation time. The universal profile is apparently a result of some physical principles operating on a broad range of initial conditions rather than of some specific initial condition.

According to the standard CDM scenario, structure in our Universe formed hierarchically. Small-scale fluctuation were the first to collapse as virialised objects. These then merged to form larger systems. The inner regions of early virialised objects are very compact and often survive accretion onto a larger system to be self-bound and long-lived subhaloes of the host. Since galaxies form by the condensation of gas at the centres of early haloes, cluster galaxies are still likely associated with subhaloes in their host cluster. Only in recent years have numerical techniques and computer capabilities advanced to the point where it is possible to study in detail the properties of subhaloes. It seems that the overmerging problem has been largely resolved in current cosmological simulations. However, these suggested another problem: only a dozen dwarf galaxies are observed in our Milky Way, while many more subhaloes are resolved in current dark-matter-only simulations(Moore et al. 1998). This has often interpreted as a problem of the CDM model. Currently, there two different pictures for the suppression of galaxy formation on small scales to alleviate this problem. In the first case, visible satellites are rare objects (only one subhalo in 100 on the smallest scales). In the second case, dwarfs form with widely varying efficiency in the

dozen most massive subsystems, and galaxy formation stops altogether below some fairly high mass cutoff.

In Chapter 2, we study in detail the subhalo population with numerical simulation. In Chapter 3, we combine high resolution simulations and semi-analytic techniques to explore the relationship between galaxies and subhaloes. As we argue, the correspondence between subhaloes and galaxies is quite complicated, and thus the apparent discrepancy between subhaloes and observed galaxies are very likely due to incorrect interpretation of simulation and observation.

1.4.3 Galaxy Formation

In the previous sections we only discussed the evolution and formation of dark matter structure. However, observational astronomy mostly refer to luminous matter, like stars and galaxies, and it is important to realize that gravity alone does not provide a complete description of such observations. In the CDM paradigm, galaxies form when gas, initially well mixed with the dark matter, cools and condenses into emerging dark matter haloes. In addition to gravity, a non-exhaustive list of the processes that now need to be taken into account includes: the shock heating and cooling of gas into dark haloes, the formation of stars from cold gas and the evolution of the resulting stellar population, the feedback processes generated by the ejection of mass and energy from evolving stars, the production and mixing of heavy elements, the extinction and reradiation of stellar light by dust particles, the formation of black holes at the centres of galaxies and the influence of the associated quasar emission. These processes span an enormous range of length and mass scales. The best that can be done with current computing techniques is to model the evolution of dark matter and gas components with smoothed particle hydrodynamics (SPH). However, this method still suffers from the problem that it is quite inefficient. Moreover, every time the "baryonic" model is changed, a new simulation has to be run.

In the other approach known as semi-analytic modelling, the baryon physics is treated phenomenologically using a simple, spherically symmetric model to describe the accretion and cooling of gas into dark matter halos. It turns out that this simple model works quite well as judged by the good agreement with results of fully N -body/gas-dynamical simulations. The advantage of this approach is that it is quite efficient, and so it can be used to explore a large region of parameter space where the physics is unclear.

The standard galaxy formation picture is described by White & Rees (1978). In this picture, galaxy formation essentially proceeds in two stages. First, dark matter haloes form in a collisionless gravitational collapse, and then baryons sink to the center of these halos because the gas can dissipate energy by radiative process. A modern and more realistic description of galaxy formation process was presented by White and Frenk (1991). These authors argued that three baryonic processes are important for galaxy formation, (1) radiative cooling process. (2) star formation, and (3) feedback. Among these processes, the cooling process is the most important for galaxy formation.

Once gas begins to fall into a dark-matter haloes, shocks will heat it up to the virial temperature; in order for the gas to form stars, it must be able to undergo radiative cooling to dispose of this thermal energy. It is useful to introduce two time-scales. The

cooling time is the time scale on which gas radiates thermal energy

$$t_c = -\frac{E}{\dot{E}} \simeq \frac{3\rho k_B T}{2\mu\Lambda(T)}. \quad (1.53)$$

Where μ is the mean molecular weight for the ionized gas for primordial composition ($\mu \simeq 0.57$), k_B is the Boltzmann constant. The second time-scale is the dynamical time scale. For a uniform gas cloud with density ρ , this time-scale is

$$t_{dyn} = 1/\sqrt{G\rho}, \quad (1.54)$$

which represents the fastest time on which the cloud can collapse. These two time-scales together with the Hubble time $\tau_H = H^{-1}$, determine how the protogalaxy cools as it collapses. If $t_c > \tau_H$, then cooling cannot have been important and the cloud will have scarcely evolved since its collapse. If $\tau_H > t_c > t_{dyn}$, then the gas can cool on a cosmological timescale, but it cool so slowly that the gas cloud can adjust its pressure distribution to maintain the support of the cooling matter. There is thus a relatively quiescent quasi-static collapse on a timescale t_c . If $t_c < t_{dyn}$, the cloud cools so rapidly that dynamical processes are unable to adjust the pressure distribution in time: pressure support will be lost and the gas undergoes a rapid collapse on the free-fall timescale, accompanied by fragmentation to smaller and smaller scales as instabilities develop in the cloud.

1.5 Outline

The contents of this thesis are based upon three submitted papers and one almost completed paper in preparation for publication. Here I summarise the objective of each project as follows

Chapter 2 is the article, *The subhalo populations of Λ CDM haloes* by L. Gao, S. D. M. White, A. Jenkins, F. Stoehr, V. Springel, 2004, MNRAS, 355, 819. In this article, we use a large cosmological simulation and a variety of high resolution resimulations of individual cluster and galaxy haloes to study the systematics of subhalo populations in Λ CDM haloes.

The standard CDM theory allows for the existence of numerous subhaloes residing in a single virialised halo. Only in recent years have numerical techniques and computer capabilities advanced to the point where it is possible to study in detail the properties of such subhaloes. Most studies to date have been limited because their analysis has been performed on a small number of individual haloes. Since halo-to-halo variations are large, this may prevent the derivation of statistically significant results. Drawing from a large body of different simulations (including a large scale simulation and higher resolution simulations of individual objects) in this study we are able to examine the systematic properties of subhaloes as a function of host halo mass and redshift.

Chapter 3 is an extension of the work presented in Chapter 2, *Galaxies and subhaloes in Λ CDM clusters* by L. Gao, G. De Lucia, S. D. M White, A. Jenkins, 2004, MNRAS, 352, L1. In this article, we clarify the relationship between subhaloes and the galaxies.

1 Thesis objectives and framework

Studies of subhaloes are interesting because they are assumed to host galaxies. The most widely adopted assumption about the galaxy associated with a subhalo is that its luminosity (or its kinematics) are simply related to the mass (or potential well depth) of the corresponding subhalo. With this assumption, a variety of contradictory conclusions have been drawn from comparison with the observed properties of luminous objects in galaxy haloes and galaxy clusters. Extending by previous work by other authors and the subhalo study of Chapter 2, we combine 10 high resolution resimulations of cluster-sized dark haloes with semi-analytic galaxy formation modelling to explore the relationship between subhaloes and galaxies.

Chapter 4 is the article, *Early Formation and Late Merging of the Giant Galaxies* by L. Gao, A. Loeb, J. Peebles, S. D. M. White, A. Jenkins, 2004, ApJ, 614, 17. In this article, we study the assembly of the central cusps of Λ CDM clusters.

This work follows up on earlier work by Loeb & Peebles (2003). The principal goal is to understand how giant central cluster galaxies were assembled in the now-standard LCDM cosmogony, e.g. when were they assembled, and by what path?

Chapter 5 is an uncompleted article, *The first structures in CDM Universe* by L. Gao, S. D.M. White, A. Jenkins, V. Springel, C. S. Frenk. In this article, we perform a suite of high resolution simulations with the aim of resolving one of the earliest forming bound objects.

Current smoothed-particle-hydrodynamical simulations of the first stars suffer from the problem of unrealistic initial conditions. Thus the question: “when were the first stars born”? is still an open one. In this study, we devise a simulation recipe with correct cosmological boundary conditions in order to resolve the earliest collapsed objects in which the *PoP III* stars may be born.

References

- Barnes, J., Hut, P. (1986), *A hierarchical $O(N\log N)$ force-calculation algorithm*, Nature, 324, 446
- Bardeen, J., Bond, J. R., Kaiser, N., Szalay, A., S. (1986), *The statistics of peaks of Gaussian random fields*, ApJ, 304, 15
- Baugh, C. M., Cole, S., Frenk, C. S., Lacey, C. G. (1998), *The epoch of galaxy formation*, ApJ, 498, 504
- Bertschinger, E. (1998), *Simulation of structure formation in the universe*, Annu. Rev. Astron. Astrophys., 36, 599
- Bond, J. R., Kaiser, N., Cole, S., Efstathiou, G. (1991), *Excursion set mass functions for hierarchical Gaussian fluctuations*, ApJ, 379, 440
- Cole, S. (1991), *Modeling galaxy formation in evolving dark matter halos*, ApJ, 367, 45
- Coles, Peter, Melott, Adrian L., Shandarin, Sergei F. (1993), *Testing approximations for non-linear gravitational clustering*, MNRAS, 260, 765
- Coles, P., Lucchin, F. (1995), *Cosmology*, John Wiley & Sons
- Couchman, H. M. P. (1991), *Mesh-refined P^3M : A fast adaptive N -body algorithm*, ApJ, 368, 23
- Couchman, H. M. P., Thomas, P., Pearce, F. (1995), *Hydra: Adaptive-mesh implementation of P^3M -SPH*, ApJ, 452, 797
- Diemand, J., Moore, B., Stadel, J. (2004), *Convergence and scatter of cluster density profiles*, astro-ph/0402267
- Dubinski, J. (1996), *A parallel tree code*, New Astronomy, 1, 133
- Efstathiou, G., Davis, M., Frenk, C. S., White, S. D. M. (1985), *Numerical techniques for large cosmological N -body simulations*, ApJS, 57, 241
- Ghigna, S., Moore, B., Governato, F., Lake, G., Quinn, T., Stadel, J. (1998), *Dark matter haloes within clusters*, MNRAS, 300, 146
- Ghigna, S., Moore, B., Governato, F., Lake, G., Quinn, T., Stadel, J. (2000), *Density Profiles and Substructure of Dark Matter Halos: Converging Results at Ultra-High Numerical Resolution*, ApJ, 544, 616

References

- Gottlöber, S., Lokas, Ewa L., Klypin, A., Hoffman, Y. (2003), *The structure of voids*, MNRAS, 344, 715
- Hernquist, L., Katz, N. (1989), *TREESPH: A unification of SPH with the hierarchical TREE method*, ApJ, 70, 419
- Jenkins, A., Frenk, C. S., Pearce, F. R., Thomas, P. A., Colberg, J. M., White, S. D. M., Couchman, H. M. P., Peacock, J. A., Efstathiou, G., Nelson, A. H. (1998), ApJ, 499, 20
- Jenkins, A., Frenk, C. S., White, S. D. M., Colberg, J. M., Cole, S., Evrard, A. E., Couchman, H. M. P., Yoshida, N. (2001), *The mass function of dark matter haloes*, MNRAS, 321, 372
- Kauffmann, G., Colberg, J. M., Diaferio, A., White, S. D. M. (1999), *Clustering of galaxies in a hierarchical universe – I. Methods and results at $z = 0$* , MNRAS, 303, 188
- Kauffmann, G., White, S. D. M. (1993), *The merging history of dark matter haloes in a hierarchical universe*, MNRAS, 261, 921
- Klypin, A. A., Gottlöber, S., Kravtsov, A. V., Khokhlov, A. M., (1999), *Galaxies in N -body simulations: Overcoming the overmerging problem*, ApJ, 516, 530
- Klypin, A., Kravtsov, A. V., Valenzuela, O., Prada, F. (1999), *Where Are the Missing Galactic Satellites?*, ApJ, 522, 82
- Lacey, C., Cole, S. (1993), *Merger rates in hierarchical models of galaxy formation*, MNRAS, 262, 627
- Lacey, C., Cole, S. (1994), *Merger Rates in Hierarchical Models of Galaxy Formation - Part Two - Comparison with N -Body Simulations*, MNRAS, 271, 676
- Loeb, A., Peebles, P. J. E. (2003), *Cosmological Origin of the Stellar Velocity Dispersions in Massive Early-Type Galaxies*, ApJ, 589, 29
- Longair M. (1998), *Galaxy Fomation*, Springer, 1998
- Mo, H. J., White, S. D. M. (1996), *An analytic model for the spatial clustering of dark matter haloes*, MNRAS, 282, 347
- Mo, H. J., White, S. D. M. (2002), *The abundance and clustering of dark haloes in the standard Λ CDM cosmogony*, MNRAS, 336, 112
- Moore, B., Ghigna, S., Governato, F., Lake, G., Quinn, T., Stadel, J., Tozzi, P. (1999), *Dark Matter Substructure within Galactic Halos*, ApJ, 524, 19
- Navarro, J. F., Frenk, C. S., White, S. D. M. (1996), *The structure of cold dark matter halos*, ApJ, 462, 563
- Navarro, J. F., Frenk, C. S., White, S. D. M. (1997), *A universal density profil e from hierarchical clustering*, ApJ, 490, 493

-
- Navarro, J. F., Hayashi, E., Power, C., Jenkins, A. R., Frenk, C. S., White, S. D. M., Springel, V., Stadel, J., Quinn, T. R. (2004), *The inner structure of CDM haloes - III. Universality and asymptotic slopes*, MNRAS, 349, 1039
- Peacock, J. A. (1999), *Cosmological Physics*, Cambridge University Press
- Peebles, P. J. E. (1993), *Principles of physical cosmology*, Princeton University Press
- Reed, D., Gardner, J., Quinn, T., Stadel, J., Fardal, M., Lake, G., Governato, F. (2003), *Evolution of the mass function of dark matter haloes*, MNRAS, 346, 565
- Seljak, U., Zaldarriaga, M. (1996), *A Line-of-sight Integration Approach to Cosmic Microwave Background Anisotropies*, ApJ, 469, 437
- Sheth, R. K., Tormen, G. (1999), *Large-scale bias and the peak background split*, MNRAS, 308, 119
- Sheth, R. K., Mo, H. J., Tormen, G., (2001), *Ellipsoidal collapse and an improved model for the number and spatial distribution of dark matter haloes*, MNRAS, 323, 1
- Sheth, R. K., Tormen, G. (2002), *An excursion set model of hierarchical clustering: ellipsoidal collapse and the moving barrier*, MNRAS, 329, 61
- Spergel, D. N., Verde, L., Peiris, H. V., Komatsu, E., Nolta, M. R., Bennett, C. L., Halpern, M., Hinshaw, G., Jarosik, N., Kogut, A., Limon, M., Meyer, S. S., Page, L., Tucker, G. S., Weiland, J. L., Wollack, E., Wright, E. L. (2003), *First-Year Wilkinson Microwave Anisotropy Probe (WMAP) Observations: Determination of Cosmological Parameters*, ApJS, 148, 175
- Springel, V., Yoshida, N., White, S. D. M. (2001a), *GADGET: a code for collisionless and gasdynamical cosmological simulations*, New Ast. 6, 79
- Springel, V., White, S. D. M., Tormen, G., Kauffmann, G. (2001b), *Populating a cluster of galaxies - I. Results at $z = 0$* , MNRAS, 328, 726
- Stoehr, F., White, S. D. M., Tormen, G., Springel, V. (2002), *The satellite population of the Milky Way in a Λ CDM universe*, MNRAS, 335, L84
- White, S. D. M. (1978), *Core condensation in heavy halos - A two-stage theory for galaxy formation and clustering*, MNRAS, 183, 341
- White, S. D. M. (1991), *Galaxy formation through hierarchical clustering*, ApJ, 379, 52
- White, S. D. M. (1993), *Formation and Evolution of Galaxies: Lectures given at Les Houches, August 1993*, in Schaeffer R., Silk J., Spiro M., Zinn-Justin J., eds, Cosmology and Large Scale Structure, Les Houches Session LX. Elsevier, Amsterdam, P.77
- White, S. D. M. (1993), *The amplitude of mass fluctuations in the universe*, MNRAS, 262, 1023
- Zel'dovich, Y. B. (1970), *Gravitational instability: an approximate theory for large density perturbations*, A&A, 5, 84

References

2 The subhalo populations of Λ CDM haloes

Abstract

We investigate the subhalo populations of dark matter haloes in the concordance Λ CDM cosmology. We use a large cosmological simulation and a variety of high resolution resimulations of individual cluster and galaxy haloes to study the systematics of subhalo populations over ranges of 1000 in halo mass and 1000 in the ratio of subhalo to parent halo mass. The subhalo populations of different haloes are not scaled copies of each other, but vary systematically with halo properties. On average, the amount of substructure increases with halo mass. At fixed mass, it decreases with halo concentration and with halo formation redshift. These trends are comparable in size to the scatter in subhalo abundance between similar haloes. Averaged over all haloes of given mass, the abundance of low mass subhaloes per unit parent halo mass is independent of parent mass. It is very similar to the abundance per unit mass of low mass haloes in the universe as a whole, once differing boundary definitions for subhaloes and haloes are accounted for. The radial distribution of subhaloes within their parent haloes is substantially less centrally concentrated than that of the dark matter. It varies at most weakly with the mass (or concentration) of the parent halo and not at all with subhalo mass. It does depend on the criteria used to define the subhalo population considered. About 90 per cent of present-day subhaloes were accreted after $z = 1$ and about 70 per cent after $z = 0.5$. Only about 8 per cent of the total mass of all haloes accreted at $z = 1$ survives as bound subhaloes at $z = 0$. For haloes accreted at $z = 2$, the survival mass fraction is just 2 per cent. Subhaloes seen near the centre of their parent typically were accreted earlier and retain less of their original mass than those seen near the edge. These strong systematics mean that comparison with galaxies in real clusters is only possible if the formation of the luminous component is modelled appropriately.

2.1 Introduction

According to the standard CDM scenario, structure in our Universe formed hierarchically. Small-scale fluctuations were the first to collapse as virialised objects. These then merged to form larger systems. The inner regions of early virialised objects are very compact and often survive accretion onto a larger system to become self-bound subhaloes of their host. Since galaxies form by the condensation of gas at the centres of early haloes, most cluster galaxies may well be associated with subhaloes in their host cluster. Only in recent years have numerical techniques and computer capabilities advanced to the point where it is possible to study in detail the properties of such subhaloes (Moore et al. 1998, 1999; Tormen, Diaferio & Syer 1998; Klypin et al. 1999a,b; Ghigna et al. 1998, 2000; Springel et al. 2001; Stoehr et al. 2002, 2003). These studies indicate that the ‘overmerging’ problem in early simulations, i.e. the failure to resolve subhaloes corresponding to galaxies

2 The subhalo populations of Λ CDM haloes

in cosmological simulations of cluster haloes, was in part a result of insufficient mass and force resolution.

Using high resolution resimulations of individual cluster or galaxy haloes, it is possible to study the properties of subhaloes in detail. Recent papers by De Lucia et al. (2004), Diemand et al. (2004) and Gill, Knebe & Gibson (2004) discuss many aspects of this topic and present results compatible with but complementary to those presented below. Most studies to date have been limited because their analysis has been performed on a small number of individual haloes. Since halo-to-halo variations are large, this may prevent the derivation of statistically significant results. In addition, all studies are still affected at some level by numerical resolution. The available tests show that the subhaloes seen in a particular object are reproduced moderately well in mass, but not in position or velocity, when the same object is resimulated multiple times with varying resolution (Ghigna et al. 2000; Springel et al. 2001; Stoehr et al. 2002, 2003). This is a result of the well known divergence of neighboring trajectories in nonlinear dynamical systems.

In this paper, we carry out a systematic study of the properties of subhaloes in the halo population of a single, large-scale cosmological simulation, and we complement this by analysing a multi-resolution set of resimulations of a single ‘Milky Way’ halo, together with a set of high-resolution resimulations of eight different rich clusters. These resimulations allow us to investigate how numerical resolution and halo-to-halo variation affect the conclusions from our cosmological simulation. We do not, however, carry out a full study of the numerical requirements for fully converged numerical results for the properties of subhaloes.

Previous studies of subhaloes within haloes of different scale have emphasised similarities – to a large extent the internal structure of a ‘Milky Way’ halo looks like a scaled version of that of a rich cluster halo (Moore et al. 1999; Helmi & White 2001; Stoehr et al. 2003; De Lucia et al. 2004; Desai et al. 2004). We show below that this scaling is not exact, and that a better model assumes the mass distribution of low-mass subhaloes to be the same as in the Universe as a whole, once the differing definitions of an object’s boundary are accounted for. We show that galaxy haloes have fewer high-mass subhaloes than rich clusters because of their earlier formation times. Indeed, even among haloes of given mass, the number of massive subhaloes correlates well with formation time, as reflected in the halo’s central concentration.

The emphasis of earlier high resolution work on solving the ‘overmerging problem’ has given rise to the impression that the subhaloes are typically objects which formed at very early times. We demonstrate below that this is not the case. Even at low subhalo masses, most subhaloes were accreted onto the main halo at low redshift, in most cases well below $z = 1$. This is important when considering the formation paths of present-day cluster galaxies.

Our paper is organized as follows. We introduce our various simulation sets in Section 2. In Section 3, we compare the halo mass abundance function measured from our cosmological simulation with theoretical predictions and with earlier numerical data. In Section 4, we investigate the subhalo population as a function of halo mass and of redshift. The spatial distribution of subhaloes within haloes is also discussed in Section 4. In Section 5 we investigate the infall and mass-loss histories of present-day subhaloes, as well as the fate of objects that are accreted onto bigger clusters at early times. We discuss our results and

set out our conclusions in Section 6.

2.2 The Simulations

2.2.1 The GIF2 cosmological simulation

We have carried out a cosmological simulation of a Λ CDM universe in a periodic cube of side $110 h^{-1}\text{Mpc}$. The total number of particles is 400^3 , and the individual particle mass is $1.73 \times 10^9 h^{-1} M_{\odot}$. This is a factor of 8 better than the mass resolution of the GIF simulations published by Kauffmann et al. (1999) but otherwise the parameters and output strategy of the simulations are rather similar. We therefore call our new simulation GIF2. The cosmological parameters adopted are: $\Omega = 0.3$, $\lambda = 0.7$, $\sigma_8 = 0.9$, and $h = 0.7$; We choose initial fluctuation power spectrum index $n = 1$, with the transfer function produced by CMBFAST (Seljak & Zaldarriaga 1996) for $\Omega_b h^2 = 0.0196$.

Initial conditions were produced by imposing perturbations on an initially uniform state represented by a ‘glass’ distribution of particles. This we generated with the method developed by White (1993) which involves evolution from a Poisson distribution with the sign of Newton’s constant changed when calculating peculiar gravitational forces. Fluctuations are imposed using the algorithm described in Efstathiou et al. (1985). Based on the Zeldovich (1970) approximation, a Gaussian random field is set up by perturbing the positions of the particles and by assigning them velocities according to the growing mode solution of linear theory.

In order to save computational time, we performed the simulation in two steps. First, we ran the simulation from high redshift until $z = 2.2$ with the parallel SHMEM version of HYDRA (Couchman, Thomas & Pearce 1995; Macfarland et al. 1998). At these times the particle distributions are lightly clustered and thus the P3M based gravity solver is quite efficient. We then completed the simulation with a tree-based parallel code, GADGET (Springel, Yoshida & White 2001), which has better performance in the heavily clustered regime.

Since the two codes adopt different force-softening schemes, it is necessary to match the force shape at the time we switch from one code to the other. The softened force becomes Newtonian at a distance of about 2.3ϵ for HYDRA, while this occurs at a distance of 2.8ϵ for GADGET. Experimentation showed that a factor of 1.06, namely $\epsilon_{\text{Hydra}} = 1.06\epsilon_{\text{Gadget}}$, produces an excellent match of the two force laws. In practice, we started the simulation at $z = 49$ with $\epsilon = 7h^{-1}\text{kpc}$ in comoving units within HYDRA, and changed the softening to $\epsilon = 6.604h^{-1}\text{kpc}$ for the continuation with GADGET after redshift 2.2.

The simulation was carried out on 512 processors of the Cray T3E at the Rechenzentrum Garching, the supercomputer centre of the Max-Planck Society. We stored the data at 50 output times logarithmically spaced between $1 + z = 20$ and $1 + z = 1$. This enables us to construct halo and subhalo merging trees as in Springel et al (2001). These will be used in other work to model galaxy formation within the simulation, so that issues of galaxy assembly and galaxy clustering can be addressed. The numerical data for our GIF2 simulation are publicly available at <http://www.mpa-garching.mpg.de/Virgo>

2 The subhalo populations of Λ CDM haloes

Table 2.1: Numerical parameters for the GA-series simulations.

	<i>GA0</i>	<i>GA1</i>	<i>GA2</i>	<i>GA3n</i>
N_p	68323	637966	5953033	55564205
$m_p[h^{-1}M_\odot]$	1.8×10^8	1.9×10^7	2.0×10^6	2.5×10^5
$\epsilon[h^{-1}\text{kpc}]$	1.8	1.0	0.48	0.24

Table 2.2: Particle number in the high resolution region and final M_{200} for the 8 cluster simulations.

	<i>C1</i>	<i>C2</i>	<i>C3</i>	<i>C4</i>
N_p	8457516	7808951	13466254	9352943
$m_{200}[h^{-1}M_\odot]$	0.81×10^{15}	0.75×10^{15}	0.52×10^{15}	0.54×10^{15}
	<i>C5</i>	<i>C6</i>	<i>C7</i>	<i>C8</i>
N_p	9011020	8704504	10182210	8454580
$m_{200}[h^{-1}M_\odot]$	0.62×10^{15}	0.84×10^{15}	0.45×10^{15}	0.60×10^{15}

2.2.2 Higher resolution simulations of individual halos

In order to investigate the importance of numerical and resolution effects in the study of subhaloes, we have used a set of multi-resolution resimulations of a Milky Way sized halo carried out by Stoehr et al. (2002, 2003). The simulations studied here are the versions called GA1, GA2 and GA3n in the original papers. The final mass of the main halo studied here is $M_{200} = 2 \times 10^{12}h^{-1}M_\odot$ and its maximum circular velocity is 240 km s^{-1} . In this series of resimulations all perturbation modes present in the initial conditions of a given resimulation are exactly inherited by all higher resolution ones. Hence all significant structure in the low resolution systems should be reproduced at higher resolution. The number of particles in the high-resolution region, the particle mass and the gravitational softening are given for the GA simulations in Table 1.

We analyse in addition a set of 8 high-resolution resimulations of rich cluster halos previously studied in Gao et al. (2003) and Navarro et al. (2003). These simulations all have the same particle mass and force resolution, $5.12 \times 10^8 h^{-1}M_\odot$ and $\epsilon = 5h^{-1}\text{kpc}$, respectively. The clusters were originally chosen as all objects in a relatively narrow mass range within the $0.479h^{-1}\text{Gpc}$ cosmological simulation of Yoshida et al. (2001). The initial particle number in the high resolution region of each simulation and the mass of the final virialized object are listed in Table 2.

All these high-resolution resimulations assumed the same cosmological parameters as our GIF2 simulation, and all were all run with the publicly available code Gadget 1.1.

2.3 The mass function of haloes

We have used a friends-of-friends group-finding algorithm (Davis et al. 1985) with the standard linking length of 0.2 in units of the mean interparticle separation to identify virialised haloes in our GIF2 simulation. Only haloes which contain at least 20 particles are included in the halo catalogues we analyse below.

The halo mass function (the abundance of haloes as a function of their mass) is one of the fundamental quantities characterising the nonlinear distribution of mass in the Universe. Substantial effort has gone into building theoretical models for this function and into calibrating them with numerical simulations (Press & Schechter 1974; Bond et al. 1991; Lacey & Cole 1993, 1994; Mo & White 1996; Sheth & Tormen 1999; Sheth, Mo & Tormen 2001; Jenkins et al. 2001; Reed et al. 2003; Yahagi et al. 2004). Here we use our GIF2 simulation, which has a reasonable volume and good mass resolution, to compare the FOF halo mass distribution against published fitting formulae for halo masses down to $4 \times 10^{10} h^{-1} M_{\odot}$ and for redshifts up to $z = 5$.

In Fig. 2.1, we plot the differential halo mass function measured directly from the GIF2 simulation (red dotted line), the theoretical predictions from Press-Schechter theory (dotted line) and from Sheth & Tormen (1999) (dashed line), and the fit to numerical data published by Jenkins et al. (solid line). Note that we plot the mass function of Jenkins et al. only over the mass range where their fitting formula was checked. We have multiplied the mass function by M^2 before plotting in order to take out the dominant mass dependence and to make the differences between the various formulae more apparent. Fig. 2.1 clearly shows that, in the redshift and mass range studied, the FOF(0.2) halo mass function is well described by the formulae of Jenkins et al. and of Sheth & Tormen. While being not perfect, the fit is extremely good in comparison with the Press & Schechter mass function. This confirms the recent conclusion of Reed et al. (2003) and Yahagi et al. (2004), based on simulations of smaller volumes, that these formulae can be applied at earlier redshift and to lower masses than previously demonstrated.

2.4 Subhalo populations

Several methods have been proposed to identify subhaloes within larger systems. For a detailed review we refer to Springel et al. (2001; hereafter SWTK). In this paper, we use the algorithm SUBFIND, developed by SWTK, to isolate locally overdense and self-bound particle sets within dark matter haloes. All such subhaloes containing at least 10 particles are included in our subhalo catalogues.

2.4.1 A convergence study of subhalo populations

Independent of the particular method employed to identify subhaloes, most published studies agree that the differential subhalo mass function (MDF) of an individual halo is approximately a power-law, $dn/dm \sim m^{-\alpha}$, with $\alpha = 1.7 - 1.9$ independent of redshift and of the mass of the parent halo (Moore et al. 1999; Ghigna et al. 2000; De Lucia et al. 2004). No study so far has compared in detail the properties of the subhaloes identified by different methods. Different criteria for defining the boundaries and the membership of subhaloes

2 The subhalo populations of Λ CDM haloes

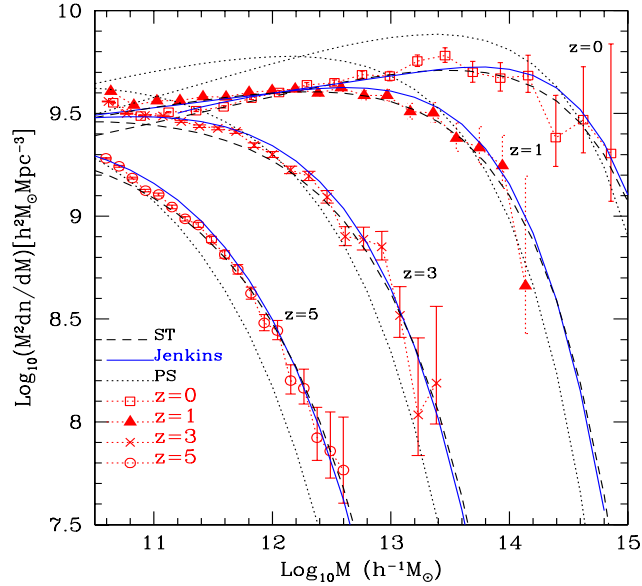


Figure 2.1: Comparison of the differential halo mass function in our GIF2 simulation with different analytic predictions. Halos were identified with a standard FOF algorithm with linking length $b = 0.2$, and we plot data for all haloes containing more than 20 particles. Note that we have multiplied the mass function by M^2 to take out the dominant mass dependence.

are bound to lead to systematic differences in subhalo populations, but the uniformity of the derived slopes suggests that such differences may be correctable through simple scaling factors.

Further study of the effects of numerical resolution on simulated subhalo populations is clearly important. Numerical convergence was claimed by Ghigna et al. (2000; hereafter G00), by SWTK and by Stoehr et al (2002, 2003) on the basis of multi-resolution simulations of individual objects. However, the data presented are not fully convincing. For example, Fig. 2.5 of SWTK shows the subhalo mass function for a rich cluster resimulated 4 times with increasing mass and force resolution. The subhalo abundance in the lowest resolution simulation S1 agrees well with that in the highest resolution simulation S4, while the intermediate resolution simulations S2 and S3 agree very well with each other but appear significantly offset from S4. The reasons for this are unclear. We show similar data in Fig. 2.2 for the subhalo abundance in the GA series resimulations of a ‘Milky Way’ halo. (A cumulative version of this plot is given by Stoehr et al. (2002) but without GA3n data). Here agreement is excellent for subhaloes that contain at least 30 particles, but there may be significant differences for smaller subhaloes. These could be due to resolution problems. As we show below (Section 4.6 and Fig. 2.10) it appears that subhaloes with small N dissolve overly fast, particularly in the inner regions of a halo.

In order to avoid effects due to our particular definition of the boundary of a subhalo (and

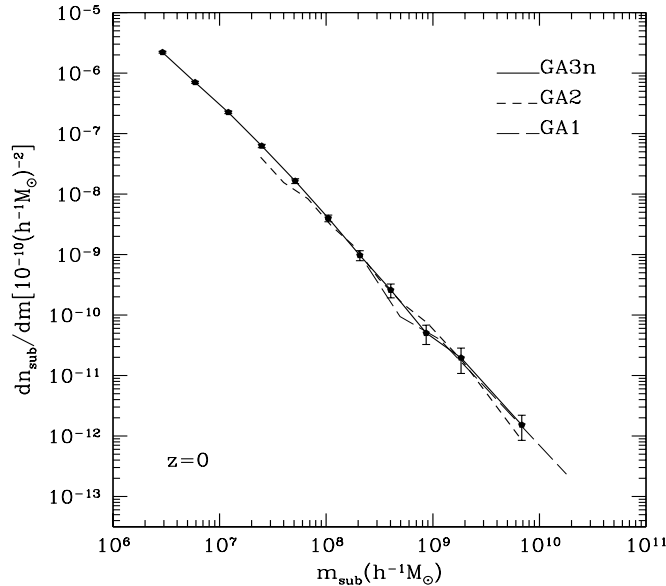


Figure 2.2: Differential subhalo abundance functions per unit host mass for the final haloes in our GA1, GA2 and GA3n simulations. Error bars assume Poisson uncertainties in the counts.

so of its mass) we check this convergence by examining the abundance of haloes in our GA series as a function of their maximum circular velocity V_{\max} . We define the square of this quantity to be the maximum value of $GM(r)/r$ for those particles identified as bound to the subhalo by SUBFIND. V_{\max} is a more stable quantity than the subhalo mass and depends little on how the subhalo is defined. Fig. 2.3 demonstrates that the cumulative abundance of subhaloes as a function of V_{\max} (the VDF) is very well reproduced between the different simulations in the GA series. Thus, we conclude that our simulation techniques correctly reproduce the subhalo abundance down to objects of relatively small particle count. In particular, GA3n reproduces the correct subhalo abundance down to values of V_{\max} below 10 km/s and so well below the values relevant to the observed satellites of the Milky Way.

Dark matter haloes are strongly nonlinear and chaotic N-body systems, so we cannot expect simulations of the ‘same’ object run with different resolution, with different codes, or with different integration parameters to be very similar at the final time. (See for example the various simulations from identical initial conditions in the Santa Barbara Cluster Comparison Project (Frenk et al. 1999) This is because in a chaotic N-body system any small perturbation to the trajectory is amplified exponentially by subsequent evolution. In the bottom panel of Fig. 2.4, we show density maps for all subhaloes belonging to the final FOF haloes of GA2 (left-hand panel) and GA3n (right-hand panel). Although these plots are qualitatively similar, there is no detailed correspondance between subhaloes. On the other hand, the upper panels show that the material which makes up these subhaloes is very similarly distributed in the two simulations at early epochs. The biggest differences

2 The subhalo populations of Λ CDM haloes

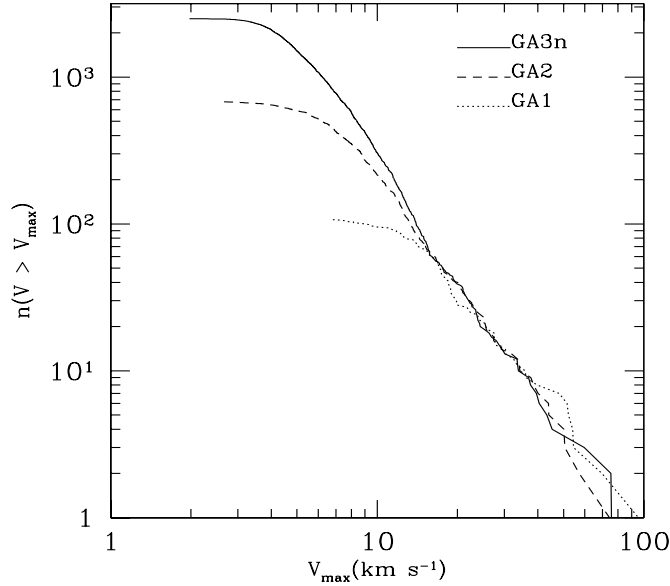


Figure 2.3: The cumulative abundance of subhaloes as a function of maximum circular velocity V_{\max} for the final haloes in the GA1, GA2 and GA3n simulations.

are due to subhaloes which are included in the final halo in one of the simulations but are just outside it in the other. Fortunately, we do not care much about the positions of individual subhaloes and are more interested in statistical results. A re-simulation of an object with higher resolution may not reproduce its structure in detail, but it can still be viewed as the result of evolution from a nearby set of initial conditions (e.g. Hayes 2003).

2.4.2 Is the population of subhaloes similar in all haloes?

A number of authors have argued that the statistical properties of subhaloes in a galaxy-sized halo are simply a scaled version of those in a rich cluster halo (Moore et al. 1999; Helmi & White 2001; De Lucia et al. 2004; Diemand et al. 2004). *Prima facie* this is surprising, since it is well known that the merging histories of haloes (and in particular their formation times) vary systematically with mass (Lacey & Cole 1993; Navarro, Frenk & White 1997). One might expect these differences to result in a systematic dependence of the subhalo population on mass.

We define a dimensionless subhalo mass, $m_n = m_{\text{sub}}/M_{\text{halo}}$, where M_{halo} is the virial mass of the parent halo defined as spherical region which has 200 times critical density of universe at that time. In the upper panels of Fig. 2.5, we plot subhalo abundance against this normalized mass for three ranges of halo mass in our GIF2 simulation, $[3 \times 10^{14} h^{-1} M_{\odot}, 10^{15} h^{-1} M_{\odot}]$, $[10^{14} h^{-1} M_{\odot}, 3 \times 10^{14} h^{-1} M_{\odot}]$ and $[3 \times 10^{13} h^{-1} M_{\odot}, 10^{14} h^{-1} M_{\odot}]$. These bins contain 7, 33 and 243 haloes, respectively. In this plot we also include subhalo abundance functions for GA3n and for our 8 cluster simulations. If halo populations of

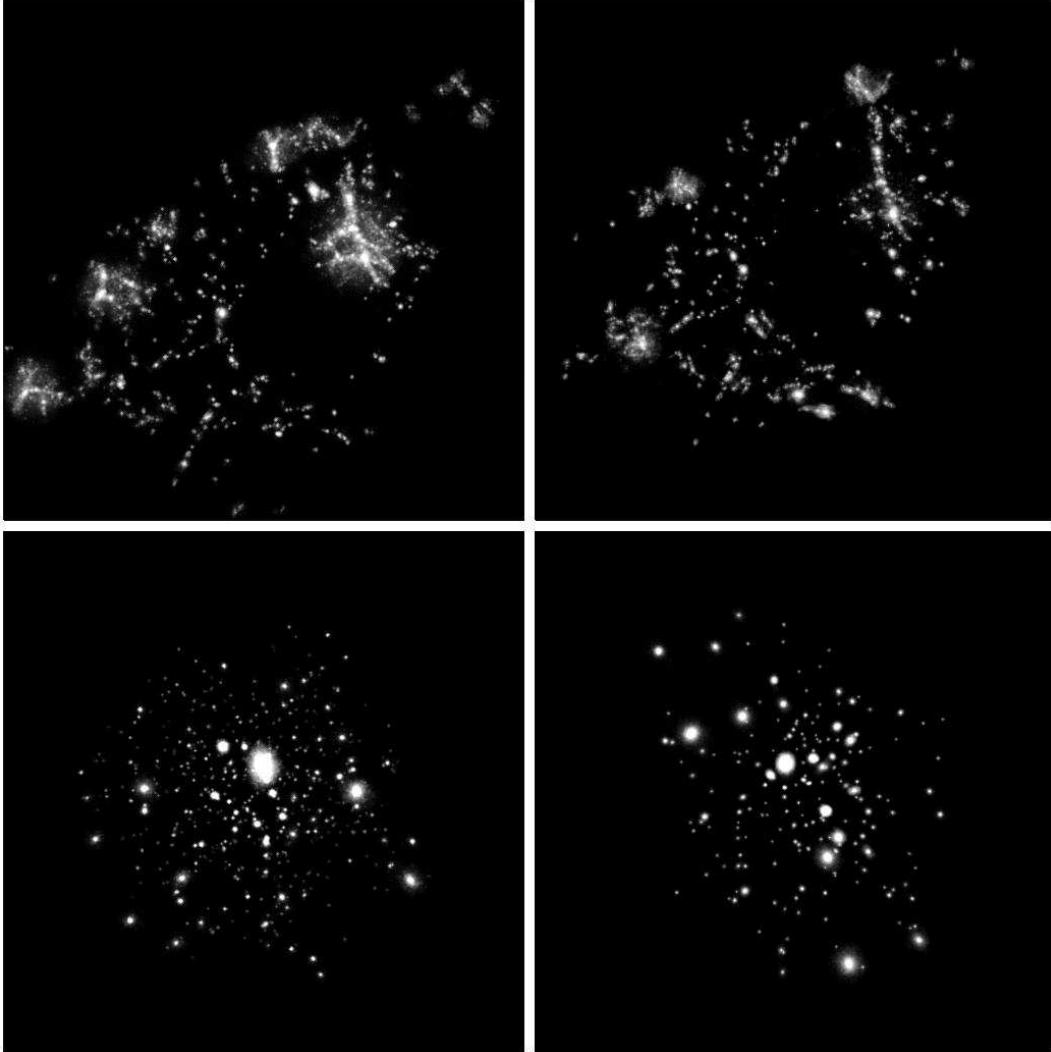


Figure 2.4: Images at $z = 0$ and $z = 5$ of the material contained in $z = 0$ subhaloes of the main halo with mass exceeding $5.8 \times 10^8 h^{-1} M_{\odot}$ in GA2 and GA3n. Upper plots are for $z = 5$, lower plots for $z = 0$. GA2 is shown on the left and GA3n on the right.

2 The subhalo populations of Λ CDM haloes

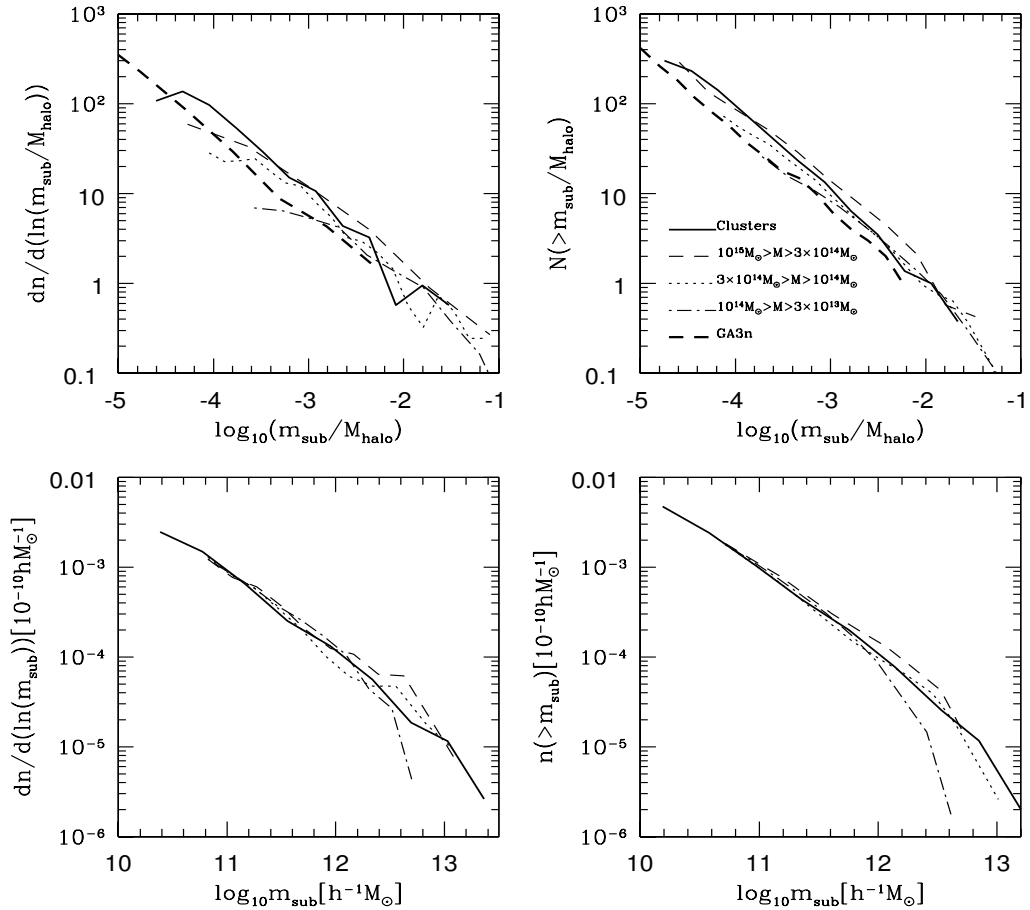


Figure 2.5: Mass functions at $z = 0$ for subhaloes within radius r_{200} of their parent haloes. In the top left-hand panel we plot differential subhalo abundance as a function of scaled subhalo mass, $m_n = m_{\text{sub}}/M_{\text{halo}}$, for three ranges of halo mass in our GIF2 simulation, for GA3n and for our 8 cluster resimulations. In the top right-hand panel, we plot the corresponding cumulative mass functions. In the bottom left-hand panel, we plot differential subhalo abundance normalized to the total mass of the parent haloes, $\langle M_{\text{halo}} dn/dm_{\text{sub}} \rangle$. The corresponding cumulative mass functions are shown in the bottom right-hand panel.

differing mass were just scaled copies of each other, these various abundance functions would all agree. In fact, however, the differential and cumulative normalized mass functions of Fig. 2.5 depend systematically on halo mass. The subhalo abundance in high-mass haloes is clearly higher (at given *scaled* subhalo mass) than in low-mass haloes. The difference between the rich cluster haloes and the galaxy halo GA3n is a factor of 2. The cluster haloes also clearly have more abundant subhaloes than the lowest mass haloes in our GIF2 simulation. A similar relation between subhalo abundance and mass of the host halo can be found in Fig. 2.7 of Diemand et al. (2004).

In the bottom panels of Fig. 2.5, we show differential and cumulative plots of subhalo mass abundance using a different normalization procedure. We divide the total number of subhaloes in each bin by the total mass of all the parent haloes to obtain the subhalo abundance per unit parent halo mass. We then plot this abundance as a function of the actual mass (rather than the scaled mass). With this normalization, the subhalo mass functions of different mass haloes agree very well. For relatively low-mass parent haloes the subhalo abundance drops below that seen in more massive parent haloes for subhalo masses exceeding about 1 per cent of the parent mass. Ignoring this high mass cut-off, the subhalo abundance per unit halo mass in Fig. 2.2 is reasonably well fit by:

$$dn/dm \simeq 10^{3.2} (m_{\text{sub}} h / M_{\odot})^{-1.9} h M_{\odot}^{-1} \quad (2.1)$$

An immediate consequence of the universality of this relation is a shift with parent halo mass in the abundance of subhaloes as a function of scaled mass m_n . For small subhalo masses this shift is

$$\Delta \log_{10} f(m_n; M_{\text{halo}}) = 0.1 \Delta \log_{10} M_{\text{halo}}, \quad (2.2)$$

where $f(m_n; M_{\text{halo}})$ is the mean abundance of subhaloes by normalized mass dn/dm_n in parent haloes of mass M_{halo} . Since the slope of the subhalo MDF is close to 2, this shift in the normalized function is quite small. As an example, the abundance shifts by about a factor of 2 at fixed m_n between a typical galaxy halo of mass $10^{12} h^{-1} M_{\odot}$ and a rich cluster halo of mass $10^{15} h^{-1} M_{\odot}$. This is indeed the shift seen between GA3n and the clusters in the upper panels of Fig. 2.5

In Fig. 2.6, we plot the abundance of subhaloes as a function of V_{max} for GIF2 haloes in our three mass bins and for our 8 clusters. We normalize the abundance as above by dividing the total subhalo count in each bin by the total mass of the contributing haloes. This figure confirms the result of Fig. 2.5. With this normalization the subhalo abundance as a function of V_{max} is ‘universal’, i.e. appears not to depend on parent halo mass. We also plot in Fig. 2.6 the differential abundance of *haloes* in our GIF2 simulation as a function of V_{max} . Here we normalize by the total mass in the simulation. This shows the interesting result that subhalo abundance and parent halo abundance follow similar curves, but with the subhaloes shifted to lower velocity by 20 or 30 per cent. We will come back to this in the next section. Note that the turn-over and drop at small V_{max} for all these curves are due to the resolution limit of the simulations.

2 The subhalo populations of Λ CDM haloes

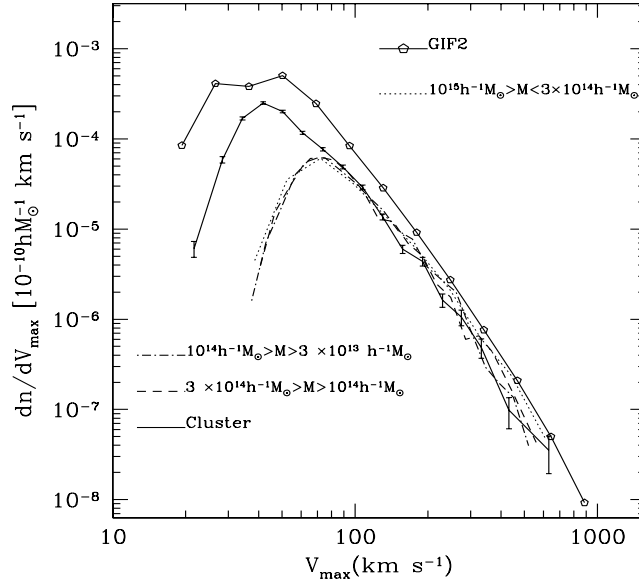


Figure 2.6: Differential abundance of subhaloes as a function of maximum circular velocity V_{\max} . Curves are shown for three halo mass ranges in the GIF2 simulation and for our 8 cluster simulations. All subhaloes within r_{200} of their hosts are counted, and the number of subhaloes in each bin is normalized by the total mass of the contributing haloes. The curve labelled GIF2 is the corresponding function for the main haloes themselves and is normalized by the total mass in the GIF2 simulation.

2.4.3 The mass fraction in subhaloes

The total fraction of a halo’s mass invested in subhaloes is an interesting quantity but one for which there is little agreement among the numbers reported in the literature (see, for example, Ghigna et al. 1998, 2000; Springel et al. 2001; Stoehr et al. 2003). Most authors estimate mass fractions between 5 per cent and 20 per cent, but Moore et al. (2001) argue that the true fraction might approach unity if subhaloes could be identified down to extremely small masses. Fig. 2.7 shows the average mass fraction (within r_{200}) in subhaloes more massive than given m_{sub} for GIF2 and cluster haloes in our three ranges of halo mass. These curves show clear trends which can already be inferred from Fig. 2.5. The subhalo mass fractions appear to converge to well-defined values as the lower limit on subhalo mass is reduced, and the asymptotic value is larger for high-mass than for low-mass haloes. Convergence is a result of the effective slope of the differential abundance function being larger than -2 , while the trend with halo mass results from the apparent universality of the abundance function at low masses (when normalized by halo mass) together with a dependence of the high-mass cut-off on halo mass.

The masses of individual subhaloes, and so the value of this asymptotic mass fraction, will depend systematically on the algorithm used to define the subhaloes. A variety of different subhalo identification schemes have been used in published studies and undoubtedly

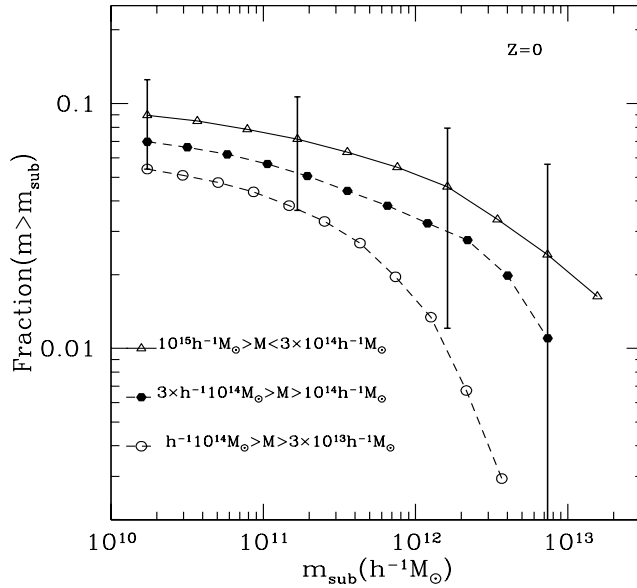


Figure 2.7: The fraction of halo mass in subhaloes. This plot shows the fraction of the mass within r_{200} of halo centre which is in subhaloes more massive than m_{sub} for GIF2 and cluster haloes in our three mass ranges. Error bars on selected points show the *rms* scatter of the individual bin values of the mean for the 15 haloes used to derive the curve for the most massive bin.

account in part for the wide range of subhalo mass fractions quoted. Notice also that since most of the subhalo mass is in the biggest objects, there is a large halo-to-halo variation (well over a factor of 2) in the overall subhalo mass fraction. We show this scatter through the error bars on selected points in the curve for the most massive haloes in Fig. 2.7. These give the *rms* scatter of the individual values for the 15 clusters averaged together to make this curve.

2.4.4 Dependence of subhalo populations on halo concentration and formation time

As demonstrated in Fig. 2.5, subhaloes tend to be more abundant in more massive haloes. In this section, we show that strong trends are also apparent with halo concentration and with halo formation time. Such systematics are not surprising since Navarro, Frenk & White (1996, 1997) showed that more massive haloes form later and have lower concentrations. They demonstrated that the density profiles of CDM haloes are well described by a simple fitting function with two parameters, ρ_s and r_s . Here r_s is a characteristic radius where the logarithmic density profile slope is -2 , and ρ_s is the mass density at r_s . They also showed that these two quantities are strongly correlated, implying a relation between concentration parameter $c = r_{200}/r_s$ and halo mass. More massive haloes are less concentrated. They argued that this is because more massive haloes typically form later. They also showed

2 The subhalo populations of Λ CDM haloes

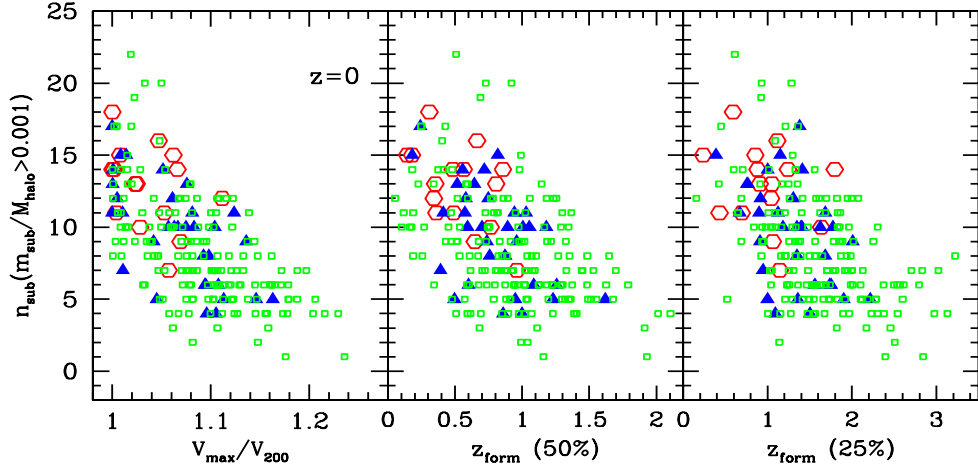


Figure 2.8: The relation between subhalo abundance and the concentration and the formation redshift of haloes. The left-hand panel shows the number of subhaloes as a function of halo concentration, as measured by V_{\max}/V_{200} , for our GIF2 and cluster simulations. Only subhaloes containing more than 0.1 per cent of the mass of their parent are considered in compiling these statistics. The middle and right-hand panels show the same measure of subhalo abundance as a function of halo formation times defined as the redshifts when the most massive progenitor has 50 per cent and 25 per cent of the final mass respectively. Open hexagons are for halos in the mass range $3 \times 10^{14} h^{-1} M_{\odot} < M_{\text{halo}} < 10^{15} h^{-1} M_{\odot}$; filled triangles are for halos with $10^{14} h^{-1} M_{\odot} < M_{\text{halo}} < 3 \times 10^{14} h^{-1} M_{\odot}$; and open squares are for haloes with $3 \times 10^{13} h^{-1} M_{\odot} < M_{\text{halo}} < 10^{14} h^{-1} M_{\odot}$.

that at given mass, haloes which form earlier have higher concentrations, a result which has been confirmed by subsequent studies (Wechsler et al. 2000; Bullock et al. 2001; Zhao et al. 2003a, 2003b). This suggests that haloes of similar concentration or formation time should have similar formation histories and so similar numbers of subhaloes.

In the left-hand panel of Fig. 2.8 we show the number of subhaloes as a function of the concentration of the host, as measured by V_{\max}/V_{200} . (Using this measure of halo concentration avoids fitting a model to our numerical data). For this comparison, we count only subhaloes with $m_{\text{sub}}/M_{\text{halo}} > 0.001$. This ensures that our results are free of resolution effects. We include data for our GIF2 haloes and for our 8 cluster simulations. Haloes of different mass are plotted using different symbols. Clearly, there is a trend for more concentrated clusters to contain fewer subhaloes and this trend is present and is similar in all three mass ranges.

The middle panel of Fig. 2.8 shows subhalo abundance as a function of halo formation redshift, defined here as the redshift at which the most massive progenitor of a $z = 0$ halo first exceeds half the mass of the final object. We obtain this value by linear interpolation between the redshifts at which we have stored values of the progenitor masses. In this plot

also there is a clear trend. Haloes which form late tend to have more subhaloes than haloes which form early, and the relation between substructure and formation time is similar for haloes of different mass. Notice that some haloes form at low redshift yet still contain few subhaloes. Examination of some specific cases suggests that these are products of recent mergers between isolated, similar mass haloes which had previously eliminated much of their substructure. In order to avoid such cases, the right-hand panel of Fig. 2.8 plots subhalo abundance against a formation time defined as the redshift when the most massive progenitor has 25 per cent of the final mass. The number of recently formed objects with little substructure is reduced and the relation between substructure and formation time appears cleaner.

A final point to note from Fig. 2.8 is the scatter in the number of subhaloes within objects of given concentration or formation time. The values span a range of up to a factor of four, and the scatter is at most weakly related to halo mass. Clearly the variety of possible formation paths for haloes of given global properties is large enough to produce widely different subhalo populations even among rather similar objects.

2.4.5 The evolution of the subhalo mass function

Our analysis so far has concentrated on the subhalo distribution within our simulated haloes at redshift $z = 0$. Although this is the time when our simulations have the best effective resolution and so can give information over the widest range of scales, it is nevertheless interesting to look at other redshifts in order to investigate the evolution of subhalo properties. Given the near universality we found above, it seems natural to concentrate on the variation with redshift of the abundance of subhaloes per unit parent halo mass, and to compare this with the abundance of haloes per unit mass in the Universe as a whole. This comparison is made in Fig. 2.9 using the abundance of subhaloes in the most massive progenitor of our ‘Milky Way’ halo in GA3n, and of the main cluster in each of our eight cluster simulations. For these plots we multiply the differential abundance distributions by the square of the (sub)halo mass in order to remove the dominant variation. We can then plot results corresponding to a range of fourteen orders of magnitude in abundance and seven orders of magnitude in (sub)halo mass. The simulation results are shown twice in these plots, for reasons discussed below. The halo abundance predicted for the Universe as a whole by the Sheth & Tormen (1999) mass function is shown by a dashed line in each panel.

Fig. 2.9 shows that subhalo abundance distributions vary rather little with redshift. At all redshifts we find the result already noted above for $z = 0$. Normalised to total available mass, the subhalo abundance within haloes is very similar to the halo abundance in the Universe as a whole. The offset between the two (the points without error bars and the dashed lines in Fig. 2.9) is almost independent of mass and epoch and is roughly a factor of four in abundance at fixed mass, corresponding to a factor of two in mass at fixed abundance. This offset can be ascribed to the different ways in which we define the limits of haloes and of subhaloes. Our haloes are bounded by a surface within which the mean interior density is 200 times the critical value, while our subhaloes are bounded by the surface where their density drops to the local value in their host. If the internal density profiles of subhaloes were exactly similar to those of their hosts, and their radial distribution

2 The subhalo populations of Λ CDM haloes

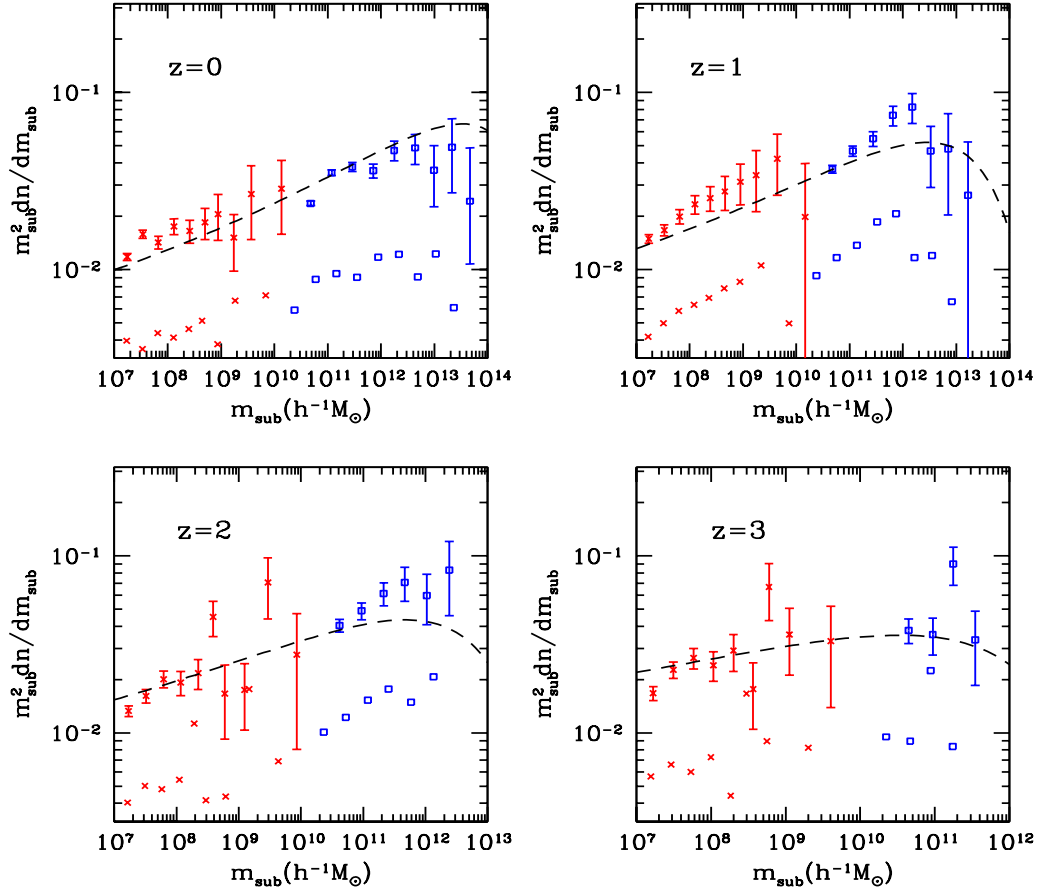


Figure 2.9: The differential abundance of subhaloes per unit parent halo mass in the GA3n simulation and in our eight cluster simulations is compared with the Sheth & Tormen (1999) formula for the abundance of haloes per unit mass in the Universe as a whole. The four panels refer to four different redshifts as shown. The simulation results are plotted twice in each panel. The symbols without error bars are for subhalo masses as returned by SUBFIND. The points with error bars are obtained when these masses are corrected upwards by a factor of two (see text). The crosses are for GA3n halo; and the squares are the averaged value of 8 clusters.

within their hosts exactly paralleled that of the dark matter, then it is easy to see that this difference in boundary definition would cause the masses of subhaloes to be about a factor of two smaller, on average than those of ‘field’ haloes of identical structure. The set of points with error bars in Fig. 2.9 shows our simulation results when the subhalo masses returned by SUBFIND are doubled to ‘correct’ for this effect. The agreement with the Sheth-Tormen curves is then remarkably good.

We note that the density profiles of the small haloes which give rise to subhaloes are more concentrated than those of the larger haloes they fall into. In addition, we show in the next section that the radial distribution of subhaloes is less concentrated than that of the mass. Both these effects should reduce the difference between the mass assigned to an isolated halo and that assigned to the subhalo it turns into. On the other hand, dynamical processes strip material from a halo once it is incorporated into a larger system, thereby reducing its mass. As we demonstrate in Section 5, most subhaloes fell into their host relatively recently and the amount of stripping is typically quite modest. The combined effect of all these factors is that once subhalo masses are doubled, as above, the number of subhaloes per unit mass within a halo is very similar to the number of small haloes per unit mass in the surrounding universe and thus in the material from which the main halo formed.

2.4.6 The spatial distribution of subhaloes

How are subhaloes distributed within their parent halo? Superficially, this appears closely related to the distribution of galaxies within clusters, but in fact this relation is complicated because subhalo masses are much more strongly affected by tidal stripping than are the luminosities of the galaxies they contain. As a result the effective total mass-to-light ratio of cluster galaxies is a strongly increasing function of clustercentric radius (see Fig. 2.12 of SWTK).

It is also interesting to ask whether the radial distribution of subhaloes depends on subhalo mass or on the mass of the parent halo. We address the latter dependence using haloes from our GIF2 and cluster simulations split into the three mass ranges already analysed in Section 4.2. For each mass range we compute the mean fraction by number of all subhaloes within r_{200} that lie within normalized radius r/r_{200} . These subhalo number density profiles are shown in the upper left-hand panel of Fig. 2.10 and are compared with a similarly defined profile for the total mass. All data are shown for $z = 0$ and for subhaloes with $m_{\text{sub}}/M_{\text{halo}} > 0.001$ only. We can then get comparable and reliable results for all three halo mass ranges. It is clear that the radial distribution of subhaloes is substantially less concentrated than that of the mass as a whole. There is no significant dependence detected on parent halo mass over the one order of magnitude range tested in this panel, but a weak dependence does appear when we compare with our ‘Milky Way’ simulation GA3n (see below).

We address the issue of possible dependences on subhalo mass using our cluster resimulations together with the haloes in the most massive bin of our GIF2 simulation (for a total of 15 systems). In the upper right-hand panel of Fig. 2.10 we show radial number fraction plots for subhalo populations limited above 10^{-3} and 10^{-4} of the parent halo mass. There appears to be a slight tendency for the more massive haloes to be more centrally

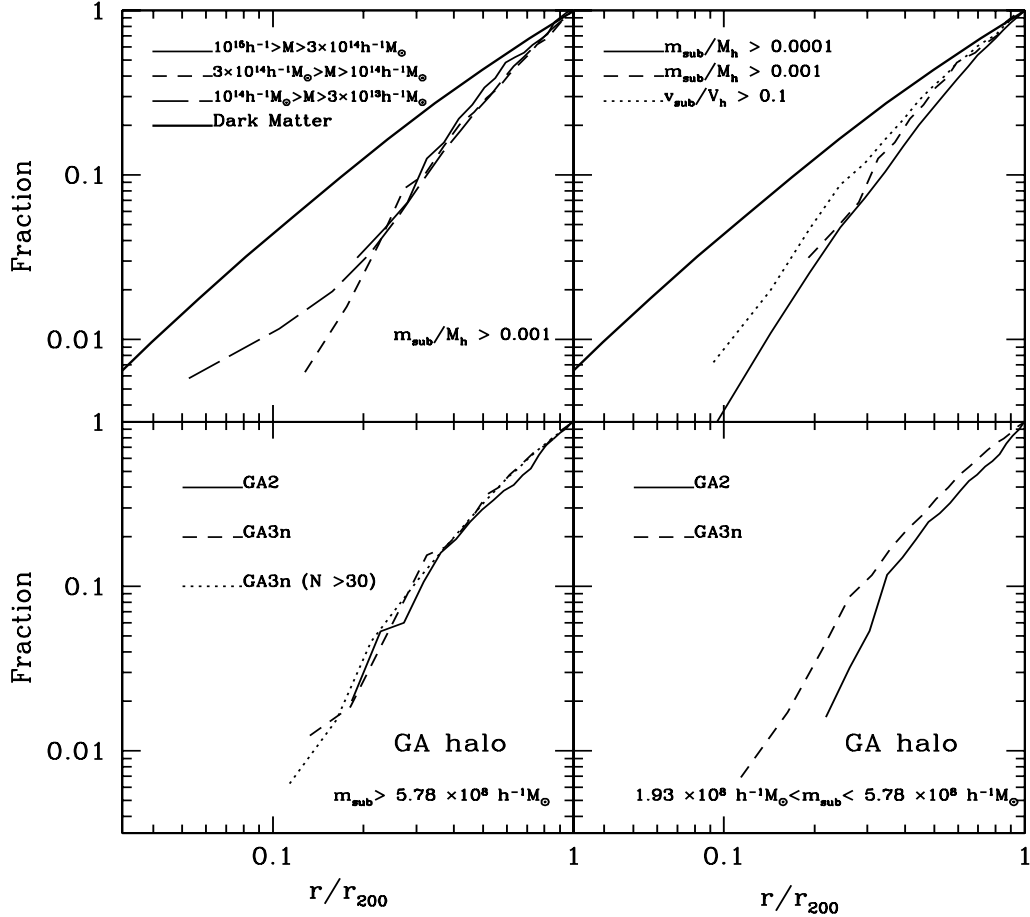


Figure 2.10: Cumulative radial distributions at $z = 0$ for subhaloes within r_{200} in various sets of haloes in our simulations. The top left-hand panel shows the fraction of all subhaloes with mass exceeding 0.1 per cent of their host halo mass and lying within r/r_{200} of halo centre. Results are plotted for haloes from our GIF2 and cluster simulations in each of the three mass ranges discussed above. The top right-hand panel shows similar profiles but for various subhalo samples of the 15 massive haloes ($M_{\text{halo}} > 3 \times 10^{14} h^{-1} M_{\odot}$) in our GIF2 and cluster simulations. For comparison, we plot cumulative profiles for the total halo mass in both panels. The bottom left-hand panel shows profiles for all subhaloes more massive than $5.78 \times 10^8 h^{-1} M_{\odot}$ for two resimulations of a ‘Milky Way’ halo with mass resolution differing by a factor of 10. This mass limit corresponds to 30 particles in the lower resolution simulation. The dotted line shows the profile for subhaloes containing at least 30 particles in the higher resolution simulation. The bottom right-hand panel gives subhalo profiles in these same two simulations but for the subhalo mass range corresponding to 10 to 30 particles in the lower resolution simulation.

concentrated, but the effect is small and it is unclear if it is significant given the relatively small number of parent haloes in our sample.

For these same 15 clusters, the upper right-hand panel of Fig. 2.10 also shows the cumulative radial profile of subhaloes for which V_{\max} is greater than 10 per cent of the parent halo's value of V_{200} . It is interesting that this population appears to be significantly more concentrated than populations defined in these same haloes above a mass threshold. This presumably results from a combination of two effects. A subhalo of given density structure is assigned smaller and smaller masses but unchanging V_{\max} values as it gets closer to the centre of its parent halo. In addition, subhaloes near the centre of their parent tend to be more heavily affected by tidal stripping than more distant objects as demonstrated in Section 5.4; such tidal stripping affects the masses of subhaloes more strongly than their maximum circular velocities (Ghigna et al. 2000; Hayashi et al. 2003).

The lower panels of Fig. 2.10 use our ‘Milky Way’ simulations to extend these results to parent haloes of lower mass and to test further for resolution effects. The dashed and solid curves compare the cumulative profiles for subhaloes with mass greater than $5.78 \times 10^7 h^{-1} M_{\odot}$ in GA2 and GA3n. This mass corresponds to 30 particles in GA2 and is $M_{\text{halo}}/40000$. The two profiles agree extremely well, suggesting that resolution is not seriously effecting our subhalo distributions. Reducing the lower limit on subhalo particle number still further does lead to noticeable effects, as we show in the lower right-hand panel of Fig. 2.10. Here the comparison is repeated for the subhalo mass range corresponding to 10 to 30 particles in GA2. The abundance of subhaloes is significantly depressed in the lower resolution simulation, particularly in the inner regions. Near the resolution limit of a simulation subhaloes begin to be lost and they disappear preferentially in the inner regions of haloes.

Note that the GA3n result in this panel agrees well with that in the left-hand panel, as does the additional GA3n profile plotted there for subhaloes with more than 30 particles (and so with $m_{\text{sub}} > 3 \times 10^{-6} M_{\text{halo}}$). Although all these profiles are close to those plotted in the upper panels for mass-limited subhalo populations within haloes of much higher mass, they are nevertheless noticeably more concentrated. This can be seen in Fig. 2.11, where we overplot the 30 particle limited subhalo number profile of GA3n and the mean profile for subhaloes with $m_{\text{sub}} > 10^{-4} M_{\text{halo}}$ in our 15 clusters; the subhalo profiles are plotted with symbols. This suggests that as the density profile of the parent halo becomes more concentrated, so too does that of the subhalo population. Note however, that the effect is much weaker for the subhaloes than for the mass as a whole. Our subhalo number density profiles are well fit by the following form:

$$n(< x)/N = (1 + ac)x^{\beta}/(1 + acx^{\alpha}) \quad (2.3)$$

where, x is the distance to the host centre in units of r_{200} , $n(x)$ is the number of subhaloes within x , N is the total number of subhaloes inside r_{200} , $a = 0.244$, $\alpha = 2$, $\beta = 2.75$, and $c = r_s/r_{200}$ is the concentration of the host halo. The lines in Fig. 2.11 show the predications of this formula for GA3n and for our 15 cluster haloes. Clearly, our fitting formula works quite well. We caution that the concentration dependence here is based on our GA-series simulations only and so should be confirmed with similar resolution simulations of other objects. We emphasize that this formula applies to subhalo populations defined above a

2 The subhalo populations of Λ CDM haloes

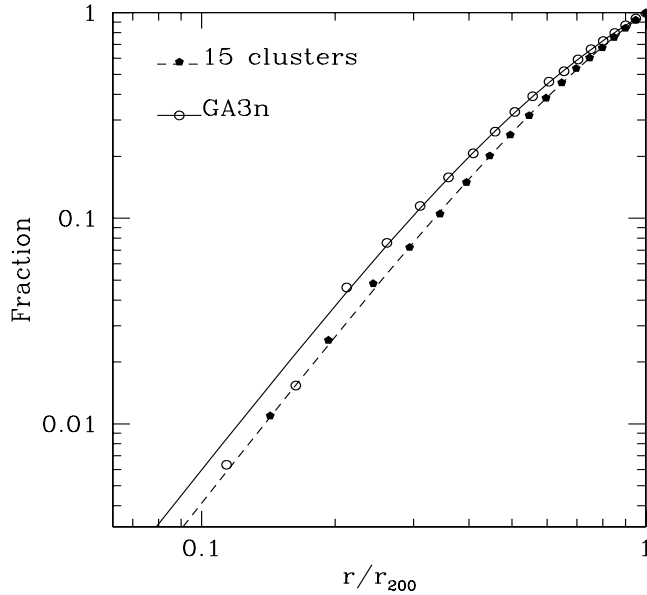


Figure 2.11: Cumulative radial distributions at $z = 0$ for subhaloes within r_{200} for the GA3n halo and out 15 clusters. The lines overlying the symbols are the corresponding fits given by Equation (3)

given lower mass limit, not to populations defined above circular velocity or luminosity limits.

Our subhalo number density profiles agree well with those presented by Diemand et al. (2003) who also found little dependence either on the mass of the parent or on the mass of the subhalo. They also agree with the subhalo profiles found by De Lucia et al. (2004) for their more massive haloes, but not with the more concentrated profiles found by these authors for their least massive haloes. The differences are relatively small but appear significant. In addition, De Lucia et al. (2004) found massive subhaloes in their simulations to be significantly less centrally concentrated than low-mass subhaloes. At present, we have no clear explanation for this difference with our results. We note that the discrepant results in De Lucia et al are based on a simulation (denoted M3 by them) which was carried out with an early version of GADGET and for which we have other indications that the chosen integration parameters produced overly condensed halo cores and thus, perhaps, overly robust subhaloes (Power et al. 2003). The profiles presented by Gill, Knebe & Gibson (2004) are also similar to ours but are somewhat steeper in the innermost regions. This is likely to reflect the rather different way in which they find subhaloes and define their masses.

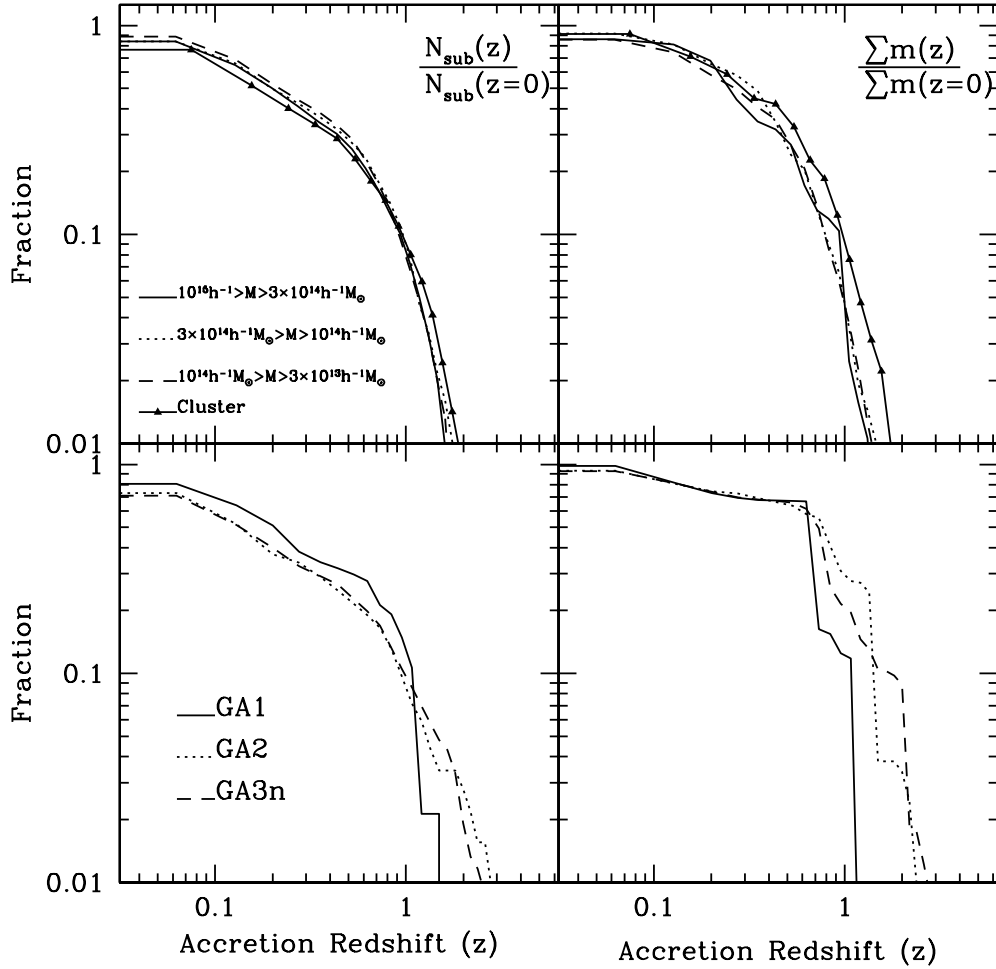


Figure 2.12: The distribution of subhalo accretion times in our simulations. The accretion time is defined as the redshift when the main progenitor first fell into a larger system and so first became a subhalo. The left-hand panels give the fraction by number of present-day subhaloes which were accreted before redshift z , while the right-hand panels give the corresponding fractions by mass. Our different mass halo samples are labelled. The upper panels refer to our samples of group and cluster haloes, while the lower panels refer to three simulations of a ‘Milky Way’ halo with differing mass resolution.

2.5 The evolution of subhaloes

In this section we analyse the evolution of subhaloes by following the history of individual objects. We construct these histories according to the definitions of SWTK. Any particular subhalo identified in one of our stored outputs can have progenitors in the immediately preceding output which are either subhaloes or independent FOF haloes. A subhalo at the earlier time is considered a progenitor if more than half its most-bound particles end up in the subhalo under consideration. A FOF halo is considered a progenitor if it contains more than half the subhalo's particles. The main progenitor of a subhalo is its largest mass progenitor. By tracing back its main progenitor, the history of any particular subhalo can be followed to the moment of 'accretion' when its principal halo ancestor fell onto a larger system and first became a subhalo.

2.5.1 The history of present subhaloes

It is interesting to know when current subhaloes were typically accreted onto the halo in which they are found. The various panels of Fig. 2.12 show, for our different parent halo samples, the fractions by number (left) and by mass (right) of present-day subhaloes which were accreted before redshift z , as given in the abscissa. In constructing these plots we have considered all subhaloes containing at least 10 particles at $z = 0$. The group and cluster mass haloes are shown in the upper panels, and the three simulations of a 'Milky Way' halo are shown in the lower panels. It is remarkable that very few of the subhaloes identified at $z = 0$ have survived as subhaloes since early times. Only about 10 per cent of them were accreted earlier than redshift 1 and 70 per cent were accreted at $z < 0.5$. These numbers are similar for haloes of all mass and do not depend significantly on the mass of the subhaloes considered. (The apparently discrepant behaviour of the mass fraction for the GA series is just a consequence of focussing on a single realisation in which a relatively massive object happened to accrete at $z \sim 0.7$.) It is clear that subhaloes are typically recent additions to the haloes in which they are seen, substantially *more* recent, in fact, than typical dark matter particles.

2.5.2 Mass loss from subhaloes as a function of time

When a virialised halo falls onto a bigger structure it loses mass continually through tidal stripping and its orbit slowly decays towards the centre of its new parent as a result of dynamical friction. It is reasonable to expect that subhaloes which fell in earlier should have lost a larger fraction of their original mass by the present day. To measure this mass loss, we calculate the ratio of the mass of each subhalo at $z = 0$ to the mass of its progenitor halo just before it was accreted. In Fig. 2.12 we plot the mean of this ratio for all present-day subhaloes more massive than $1.73 \times 10^{10} h^{-1} M_{\odot}$ as a function of their accretion redshift, showing results separately for parent haloes of different mass and including haloes from our GIF2 and cluster simulations. The noise at high redshifts in this plot is due to poor statistics. As we saw already in the last section, very few present-day subhaloes were accreted at such early times.

It is clear from Fig. 2.13 that there is little dependence of mass loss on parent halo

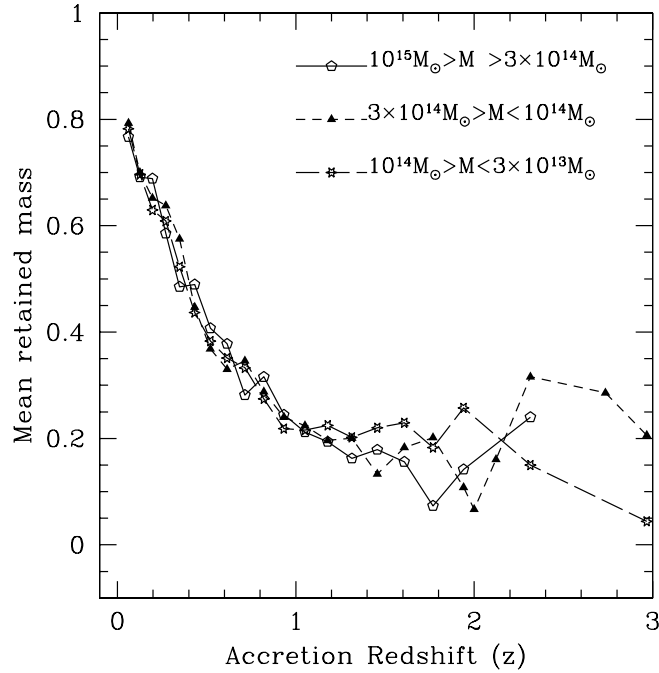


Figure 2.13: Mean retained mass fractions for subhaloes identified at $z = 0$ as a function of the redshift at which they were accreted. Different curves refer to parent haloes of different mass and all present-day subhaloes more massive than $1.73 \times 10^{10} h^{-1} M_{\odot}$ were included when taking the averages.

mass and that the mean retained mass fraction for *surviving* subhaloes is a strong function of accretion redshift. Notice that since we compile statistics for subhaloes identified at $z = 0$, we neglect objects which have been stripped to masses below our resolution limit or disrupted entirely. As we show in the next section, the retained mass fractions of Fig. 2.12 are thus substantially higher than those of typical haloes accreted at each redshift.

2.5.3 The fate of accreted haloes

In this section we follow all the haloes which are accreted onto the main progenitor of a final halo (and so first become subhaloes of it) at redshifts 2 and 1. We are interested to learn what fraction of these survive until $z = 0$, what are the final masses of the survivors, what happens to those that do not survive, and how these various fates depend on the mass of the halo which is accreted. Here we use our eight rich cluster simulations to investigate these issues. We begin by finding all progenitors of a final cluster which are independent FOF haloes in the stored output immediately beyond $z = 1$ (or 2) but are already listed as part of the main progenitor in the subsequent output. We then attempt to trace all these subhaloes forward until either we reach $z = 0$ or they are lost. Three different fates are possible for each accreted halo:

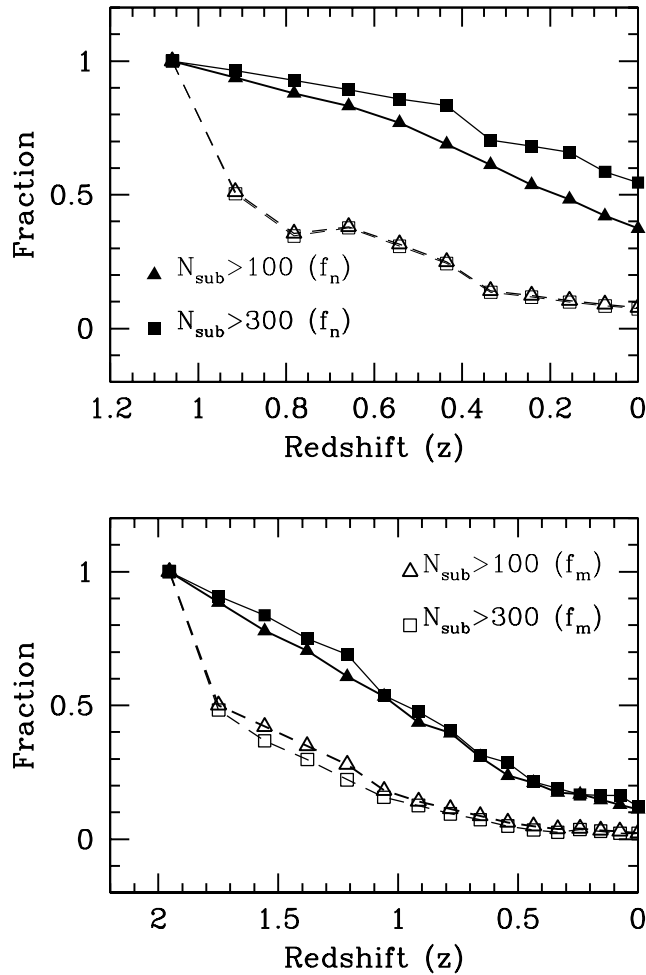


Figure 2.14: The fate of haloes which merge into the main cluster progenitor at redshifts of 2 & 1. Results are shown averaged over our eight cluster simulations in top and bottom panels, respectively. Filled symbols and solid lines show the fraction of haloes which survive as independent subhaloes at each later redshift z , while open symbols and dashed lines show the fraction of the total progenitor halo mass attached to these survivors. For each accretion redshift we show results for progenitor haloes containing at least 100 and at least 300 particles. A surviving subhalo is required to have at least 10 particles assigned to it by our subhalo-finder.

- (1) If it can be followed as a subhalo to $z = 0$, we say it survives;
- (2) If it dissolves and becomes part of the main body of its host, we say it disrupts;
- (3) If it merges with a larger subhalo and then loses its identity, we say it merges. We find that no more than a few percent of accreted haloes suffer this fate.

In Fig. 2.14 we show the fraction of accreted haloes which are identified as surviving at each later redshift, as well as the fraction of the total mass initially assigned to these haloes which remains attached to the surviving subhaloes. We see that while more than 90 per cent of accreted haloes are identified as subhaloes in the output immediately after their accretion, the total subhalo mass is, however, only about half of that assigned to the original haloes. This is a result of the effect already noted above. The algorithm which we use to identify subhaloes bounds them at a substantially higher density than that used to bound isolated haloes. Consequently, if a field halo falls onto a larger system its assigned mass decreases by a factor of two, on average, even if its structure is unchanged. As subhaloes orbit within their parent haloes, their masses are further reduced by tidal stripping. Thus the fraction of the initial mass attached to the survivors continually decreases, and more and more subhaloes drop below the mass limit for identifying them in our simulations.

Fig. 2.14 gives results for two sets of progenitor haloes at each accretion redshift. These are defined to contain at least 100 and at least 300 particles, corresponding to halo masses exceeding $5 \times 10^9 h^{-1} M_\odot$ and $1.5 \times 10^{10} h^{-1} M_\odot$, respectively. As can be seen, the mass fraction in the survivors is independent of this mass limit and is 8 per cent for haloes accreted at $z = 1$ and 2 per cent for haloes accreted at $z = 2$. The fraction of survivors by number does depend on the mass limit. Our samples only contain subhaloes identified with more than 10 particles, so descendants begin to be lost from the lower mass halo sample for mass reduction factors greater than 10 whereas factors exceeding 30 are needed to remove objects from the higher mass sample.

2.5.4 Radial dependence of accretion time and mass loss

Subhaloes which were accreted onto their parent halo's main progenitor at early times initially had relatively short orbital periods and so should be located, on average, in the inner regions of the final halo. In addition, a subhalo which has been orbiting within its parent for a long time will have suffered substantially from the effects of dynamical friction and tidal stripping, so its orbit will have decayed by a larger factor than that of a recently accreted subhalo of similar current mass. Both these effects are expected to lead to a correlation between the radial position of a subhalo and its accretion redshift.

In Fig. 2.15 we plot mean and median values of accretion redshift and of retained mass fraction against r/r_{200} for subhaloes of the 15 haloes in our GIF2 and cluster simulations with masses exceeding $3 \times 10^{14} h^{-1} M_\odot$. The upper and lower panel refer to subhaloes more massive than $2 \times 10^{10} h^{-1} M_\odot$ and more massive than $6 \times 10^{10} h^{-1} M_\odot$ respectively. Clearly there is indeed a strong age-radius relation which is similar for subhaloes of differing mass. Recently accreted subhaloes tend to occupy the outer regions of their host, while older subhaloes reside preferentially in the inner regions. In addition, haloes near the centre typically retain a much smaller fraction of their progenitor halo's mass than those in the

outer regions. The large difference between the median and the mean in the accretion redshift plot is a reflection of the substantial skewness of the distribution. As we already saw in Fig. 2.12 and 2.13, tidal stripping is clearly very effective and, as a consequence, the ancestors of inner subhaloes were more massive than those of outer subhaloes of the same mass. Thus in a galaxy cluster inner subhaloes are likely to host brighter galaxies than outer subhaloes of similar mass.

2.6 Summary and discussion

We have used a single, large-scale cosmological simulation together with two sets of resimulations of the formation of individual cluster and galaxy haloes to carry out a systematic study of the properties of dark halo substructure in the concordance Λ CDM universe. In agreement with the earlier work of Jenkins et al. (2001), Reed et al. (2003) and Yahagi et al. (2004) we find the abundance of haloes (defined using a friends-of-friends group finder with linking length $b = 0.2$) to be well described by the Sheth & Tormen (1999) mass function down to masses of a few times $10^{10}M_{\odot}$ and out to a redshift of 5. Our main results for the subhalo populations within these haloes can be summarized as follows:

- (1) The subhalo populations of different haloes are not simply scaled copies of each other, but vary systematically with global halo properties. On average, massive haloes contain more subhaloes above any given fraction of parent mass than do lower mass haloes, and these subhaloes contain a larger fraction of the parent's mass. At given halo mass, subhaloes are more abundant in haloes which are less concentrated, or formed more recently.
- (2) There is considerable scatter in the abundance of subhaloes between haloes of similar mass, concentration or formation time. This presumably reflects differences in the details of halo assembly.
- (3) For subhalo masses well below that of the parent halo the mean subhalo abundance *per unit parent mass* is independent of the actual mass of the parent. It is very similar to the abundance of haloes per unit mass in the universe as a whole, once a correction is made for the differing bounding density within which the masses of haloes and subhaloes are defined.
- (4) Normalised in this way to total parent halo mass, the mean abundance of subhaloes as a function of maximum circular velocity is also quite similar to the abundance per unit mass of haloes as a function of V_{\max} . For subhaloes the abundance per unit mass is about a factor of two lower at given V_{\max} than for haloes. Equivalently, the V_{\max} values of subhaloes at given abundance per unit mass are about 25 per cent lower than those for haloes.
- (5) In agreement with previous studies, we find the radial distribution of subhaloes within their parent haloes to be much less concentrated than that of the dark matter. We find no significant dependence of this radial profile on the mass of the subhaloes and only a very weak dependence on the mass (or concentration) of the parent halo.

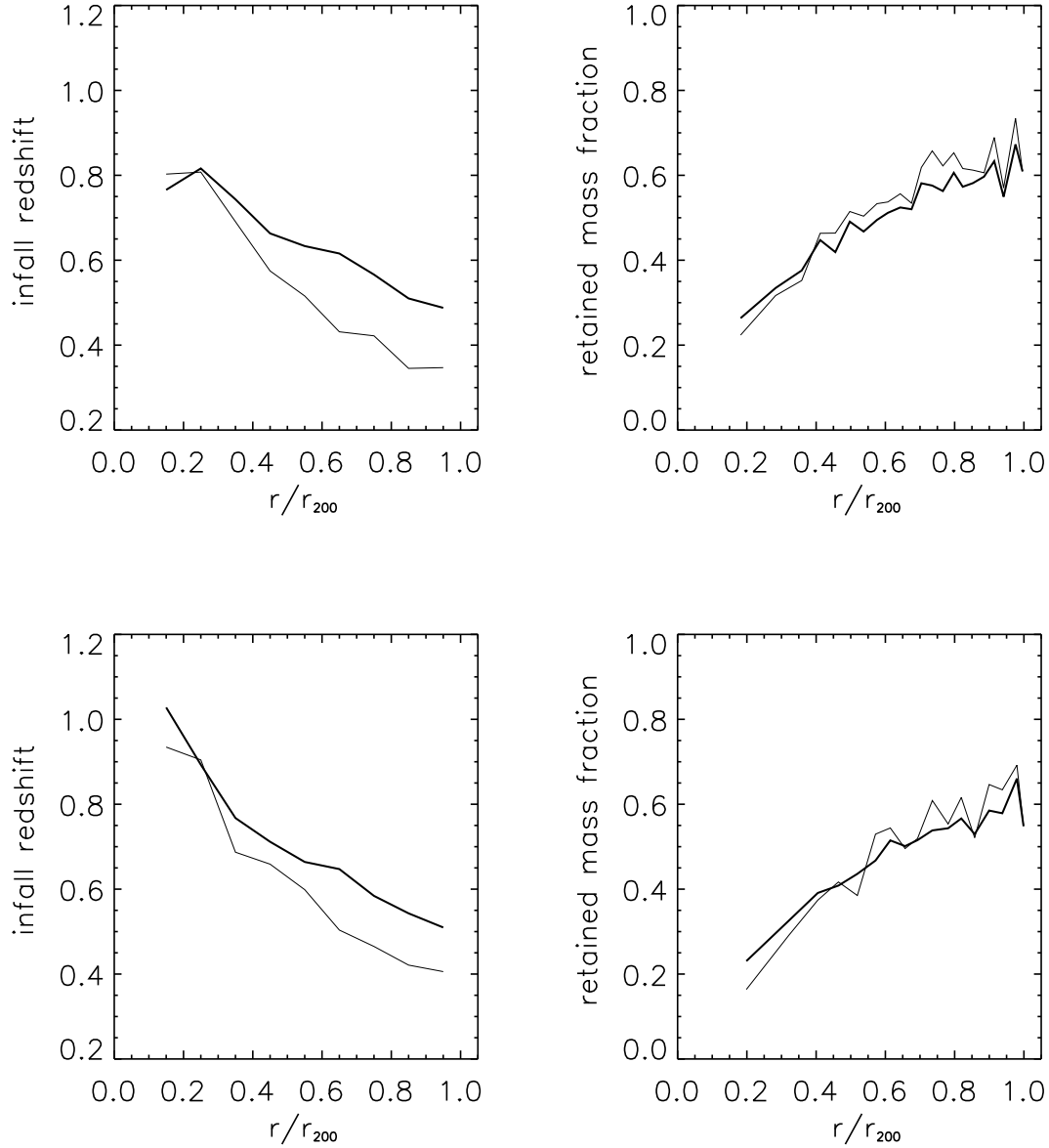


Figure 2.15: Radial dependence of the accretion redshift (left-hand panel) and retained mass fraction (right-hand panel) for subhaloes of the 15 haloes more massive than $3 \times 10^{14} h^{-1} M_{\odot}$ in our GIF2 and cluster simulations. In each panel thick solid lines give the mean at each value of r/r_{200} while thin solid lines give the median. The top panels are for subhaloes more massive than $2 \times 10^{10} h^{-1} M_{\odot}$ while bottom are for subhaloes more massive than $6 \times 10^{10} h^{-1} M_{\odot}$.

2 The subhalo populations of Λ CDM haloes

To a good approximation the radial distribution of subhaloes appears ‘universal’ and we give a fitting formula for it in equation 2.3.

- (6) The subhalo number density profile does depend on how the population is defined. Subhalo populations defined above a minimum circular velocity limit are significantly more concentrated than those defined above a minimum mass limit.
- (6) Most subhaloes in present-day haloes fell into their parent systems very recently. Only about 10 per cent of them were accreted earlier than $z = 1$ and 70 per cent were accreted at $z < 0.5$. These fractions depend very little on the mass of the subhaloes or on that of their parents
- (7) The rate at which tidal effects reduce the mass of subhaloes is not strongly dependent on the mass of the accreted object or on that of the halo it falls into. About 92 per cent of the total mass of haloes accreted at $z = 1$ is removed to become part of the ‘smooth’ halo component by $z = 0$. For haloes which fall in at $z = 2$ this fraction is about 98 per cent.
- (8) Subhaloes seen near the centre of their parent haloes typically fell in earlier and retain a smaller fraction of their original mass than subhaloes seen near the edge. Thus inner subhaloes may be expected to host brighter galaxies than outer subhaloes of similar mass (see Springel et al. 2001).

These properties suggest a relatively simple picture for the evolution of subhalo populations. A substantial fraction of the mass of most haloes has been added at relatively recent redshifts, and this mass is accreted in clumpy form with a halo mass distribution similar to that of the Universe as a whole. Since tidal stripping rapidly reduces the mass of subhaloes, the population at any given mass is dominated by objects which fell in recently and so had lower mass (and thus more abundant) progenitors. The orbits of recently accreted objects spend most of their time in the outer halo, so that subhaloes of given mass are substantially less centrally concentrated than the dark matter as a whole. Subhaloes which are seen near halo centre have shorter period orbits and so must have fallen in earlier. They thus retain a relatively small fraction of their initial mass.

Comparison of these subhalo properties with observation is far from simple. The recent accretion of most subhaloes means that the galaxies at their centres were almost fully formed by the time they became part of their current host. We might therefore expect their observable properties to be more closely related to the mass of their progenitor haloes and to their accretion redshifts than to the current masses of their subhaloes. Explicit tracking of galaxy formation during the assembly of cluster haloes shows that these differences can be large. For example, both Diaferio et al. (2001) and Springel et al. (2001) find radial number density profiles for magnitude limited samples of galaxies which are similar both to the underlying dark matter profiles and to the observed profiles of real clusters, but which are very different from the number density profiles for mass limited subhalo samples. Similar differences are to be expected between the velocity biases of galaxies and subhaloes. Models for the stellar content of subhaloes which are based purely on their current mass and internal structure are very unlikely to be successful. The past history of subhaloes must

be included to get realistic results, as must galaxies associated with apparently disrupted subhaloes. We investigate these issues further in a companion paper (Gao et al. 2004);

Acknowledgements

The simulations used in this paper were carried out on the Cray T3E and Regatta supercomputer of the computing centre of the Max-Planck-Society in Garching, and on the Cosma supercomputer of the Institute for Computational Cosmology at the University of Durham. GL thanks Yipeng Jing, Chris Power and Xi Kang for useful discussions. The numerical data for our GIF2 simulation will be publically available at <http://www.mpa-garching.mpg.de/Virgo>.

References

- Bullock J. S., Kolatt T. S., Sigard Y., Somerville R. S., Kravtsov A. V., Klypin A. A., Primack J. R., Dekel A., 2001, *ApJ*, 321, 559
- Couchman H. M. P., Pearce F. R., Thomas P. A., *ApJ*, 1995, 452, 797
- Davis M., Efstathiou G., Frenk C. S., White S. D. M., 1985, *MNRAS*, 292, 371
- De Lucia G., Kauffmann G., Springel V., White S. D. M., Lanzoni B., Stoehr F., Tormen G., Yoshida N., 2003, *MNRAS*, 348, 333
- Desai V., D'Alcanton J. J., Mayer L., Reed D., Quinn T., Governato F., 2004, preprint, astro-ph/0311511
- Diaferio A., Kauffmann G., Balogh M. L., White S. D. M.; Schade D., Ellingson E., 2001, *MNRAS*, 323, 999
- Diemand J., Moore B., Stadel J., 2004, submitted, astro-ph/0403160
- Efstathiou G., Davis M., White S. D. M., Frenk C. S., 1985, *APJS*, 57, 241
- Frenk C. S., et al, 1999, *ApJ*, 525, 554
- Gao L., Loeb A., Peebles P. J. E., White S. D. M., Jenkins A., 2003, *ApJ* submitted, preprint, astro-ph/0312499
- Gao L., De Lucia G., White S. D. M., Jenkins, A., 2004, *MNRAS* submitted, preprint, astro-ph/0405010
- Ghigna S., Moore B., Governato F., Stadel J., 1998, *MNRAS*, 300, 146
- Ghigna S., Moore B., Governato F., Lake G., Quinn T., Stadel J., 2000, *ApJ*, 544, 616
- Gill S. P. D.l, Knebe A., Gibson B. K, 2004, *MNRAS*, preprint, astro-ph/0404258
- Hayashi E., Navarro J. F., Taylor, J. E., Stadel J., Quinn, T., 2003, *ApJ*, 584, 541
- Hayes W. B, 2003, *ApJ*, 587, L59
- Helmi A., White S. D. M, *MNRAS*, 323, 529
- Jenkins A., Frenk C.S., Pearce F.R., Thomas P.A., Colberg J.M., White S. D. M., Couchman H. M. P., Yoshida N., 2001, *MNRAS*, 321, 372

References

- Klypin A., Kravtsov A., Valenzuela O., Prada F., 1999, *ApJ*, 522, 82
- Klypin A., Gottloeber, Kravsov A., Khokhlov M., 1999b, *ApJ*, 516, 530
- Lacey C., Cole S., 1993, *MNRAS*, 262, 627
- Lacey C., Cole S., 1994, *MNRAS*, 271, 676
- Macfarland T., Couchman H. M. P., Pearce F. R., Pichlmeier J., 1998, *New Astron.*, 3, 687
- Mo H. J., White S. D. M., 1996, *MNRAS*, 283, 347M
- Moore B., Katz N., Lake G., *ApJ*, 457, 455
- Moore B., Ghigna S., Governato F., Lake G., Quinn T., Stadel J., Tozzi P., 1999, *ApJ*, 524, 19
- Moore, B., Calcáneo-Roldán, C., Stadel, J., Quinn, T., Lake, G., Ghigna, S., & Governato, F. 2001, *Phys. Rev. D*, 64, 063508
- Navarro J. F., Frenk C. S., White S. D. M., 1997, *ApJ*, 490, 493
- Navarro J. F., Hayashi E., Power, C., Jenkins, A. R., Frenk, C. S., White, S. D. M., Springel V.; Stadel J., Quinn T. R., 2004, *MNRAS*, 349, 1039
- Power C., Navarro J. F., Jenkins, A., Frenk, C. S., White S. D. M., Springel V., Stadel J., Quinn T., 2003, *MNRAS*, 338, 14
- Press W.H., Schechter P., 1974, *ApJ*, 187, 452
- Reed D., Gardner J., Quinn T., Stadel J., Fardal M., Lake G., Governato F., 2003, *MNRAS*, 346, 565
- Seljak U., Zaldarriaga M., 1996, *ApJ*, 469, 437
- Sheth R., Tormen G., 1999, *MNRAS*, 308, 119
- Sheth R., Mo H. J., Tormen G., 2001, *MNRAS*, 323, 1
- Springel V., Yoshida N., White S. D. M., 2001a, *New Ast.* 6, 79
- Springel V., White S. D. M., Tormen G., Kauffmann G., 2001b, *MNRAS*, 328, 726(SWTK)
- Stoehr F., White S. D. M., Tormen G., Springel V., 2002, *MNRAS*, 335, 762
- Stoehr F., White S. D. M., Springel V., Tormen G., Yoshida N., 2003, *MNRAS*, 345, 1313
- Wechsler R. H., Bullock J. S., Primack J. R., Kravtsov A. V., Dekel A., 2002, *ApJ*, 586, 52
- White S. D. M., 1993, in schaeffer R., Silk J., Spiro M., Zinn-Justin J., eds, *Cosmology and large Scale Structure*, Les Houches Session LX. Elsevier, Amsterdam, P.77
- White S. D. M., Davis M., Efstathiou G., Frenk C. S., 1987, *Nature*, 330, 451

- Yoshida N., Sheth R. K., Diaferio A., 2001, MNRAS, 328, 669
- Yahagi H., Nagashima M., Yoshii Y., 2004, ApJ, 605, 709
- Zhao D. H., Mo H. J., Jing Y. P., Börner G., 2003a, MNRAS, 339, 127
- Zhao D. H., Jing Y. P., Mo H. J., Börner G., 2003b, ApJ, 597L, 9

References

3 Galaxies and subhaloes in Λ CDM galaxy clusters

Abstract

We combine 10 high resolution resimulations of cluster-sized dark haloes with semi-analytic galaxy formation modelling in order to compare the number density and velocity dispersion profiles of cluster galaxies with those of dark matter substructures (subhaloes). While the radial distribution of galaxies follows that of the dark matter closely, the distribution of dark matter subhaloes is much less centrally concentrated. The velocity dispersion profiles of galaxies are also very similar to those of the dark matter, while those for subhaloes are biased high, particularly in the inner regions of clusters. We explain how these differences, already clearly visible in earlier work, are a consequence of the formation of visible galaxies at the centres of dark matter haloes. Galaxies and subhaloes represent *different* populations and are not directly comparable. Evolution produces a complex and strongly position-dependent relation between galaxies and the subhaloes in which they reside. This relation can be properly modelled only by appropriate physical representation of the galaxy formation process.

3.1 Introduction

A variety of observational indicators have recently converged to establish the Λ CDM cosmogony as the *de facto* standard model for the formation of structure in our universe (e.g. Spergel et al 2003). For the general class of such hierarchical models, Navarro, Frenk & White (1996, 1997) showed that the radial density profiles of nonlinear structures such as galaxy or cluster dark haloes are well represented by a simple fitting formula of “universal shape”. As new galaxy surveys have amassed homogeneous data for large samples of clusters, the mean radial profiles of both number density and velocity dispersion have been found to conform quite closely to these NFW predictions for the dark matter (Carlberg et al. 1997; Biviano & Girardi 2003). Models which follow galaxy formation and cluster assembly explicitly do reproduce such parallel galaxy and dark matter profiles, even though the relation between the luminosity and dark matter mass of individual galaxies shows a lot of scatter and is predicted to depend strongly on clustercentric distance (Diaferio et al. 2001; Springel et al 2001).

The high resolution achieved by numerical simulations in recent years has allowed detailed study of the properties of dark matter substructure (subhaloes) within dark haloes (Tormen 1997; Ghigna et al. 2000; Klypin et al. 1999a, 1999b; Stoehr et al. 2002, 2003; De Lucia et al. 2004a; Diemand et al. 2004; Gill et al. 2004; Gao et al. 2004). These studies agree quite well on the structure, abundance and radial distribution predicted for subhaloes, once differences in numerical resolution are accounted for. On the other hand, a variety of

3 Galaxies and subhaloes in Λ CDM galaxy clusters

contradictory conclusions have been drawn from comparison with the observed properties of luminous objects in galaxy haloes and galaxy clusters (compare the discussions in Moore et al. (1998), Klypin et al. (1999), Stoehr et al. (2002,2003), Springel et al. (2001), D’Onghia & Lake (2003), Desai et al. (2003), Diemand, Moore & Stadel (2004) and Kravtsov et al. (2004)). We argue below that these disagreements can in most cases be traced to insufficiently careful modelling of the relation between the properties of subhaloes and those of the galaxies they contain.

In particular, a number of recent studies have noted that the radial distribution of subhaloes within dark haloes is very shallow compared both to that of the dark matter and to that of observed galaxies in real clusters (Ghigna et al. 2000; Diemand et al. 2004; De Lucia et al. 2004a; Gao et al 2004). Some of these authors concluded that this difference may indicate a fundamental problem for the Λ CDM model, failing to notice that the earlier simulations of Springel et al. (2001) had followed substructure with comparable numerical resolution and showed that modelling baryonic processes can produce a galaxy profile in good agreement with observation. This suggests there are serious inadequacies in a simple model where the luminosity (or kinematics) of a galaxy are simply related to the mass (or potential well depth) of the corresponding subhalo in a dark-matter-only simulation. With the assumptions of Springel et al. (2001) the relation between these properties shows very large scatter and depends systematically on radius within a cluster halo. This is because the stellar mass of galaxy is determined primarily by its halo mass at the time the stellar component was assembled rather than by its halo mass at the present day.

Semi-analytic models of the kind used by Springel et al. (2001) are an ideal tool to explore the relation between dark matter subhaloes and the galaxies they host. In this paper we use the improved semi-analytic model developed by De Lucia, Kauffmann & White (2004b) which is able to reproduce the observed luminosity functions, metallicities and colour-magnitude relations of cluster galaxies, as well as the metal content of the intracluster medium. We apply this model to a set of ten high resolution dark-matter-only resimulations of cluster formation in a Λ CDM universe, eight of which are also analysed in companion papers on the systematic properties of subhalo populations in Λ CDM dark haloes (Gao et al. 2004) and on the assembly of the central cusps of Λ CDM clusters (Gao et al. 2003)

This Letter is structured as follows. In Sec. 3.2, we briefly describe the simulations and the semi-analytic model used for this study. In Sec. 3.3, we study the spatial distributions and the velocity dispersion profiles of galaxies and dark matter substructures and we explain the differences between them. A discussion and a summary of our results are presented in Sec. 3.4.

3.2 The Simulations and the Semi-analytic Model

We use a set of ten N-body resimulations of the formation of a massive galaxy cluster in a Λ CDM Universe. The clusters range in mass M_{200} from $4.5 \times 10^{14} h^{-1} M_{\odot}$ to $8.5 \times 10^{14} h^{-1} M_{\odot}$, and were initially identified in a cosmological simulation of a region $0.5h^{-1}$ Gpc on a side (Yoshida et al. 2001). Many of them have been studied previously in Power et al. (2003), Gao et al. (2003, 2004) and Navarro et al. (2003). These resimulations

3.3 Number density and velocity dispersion profiles for galaxies and subhaloes

were carried out using the publicly available parallel N -body code GADGET (Springel, Yoshida & White 2001) with a particle mass of $5.12 \times 10^8 h^{-1} M_{\odot}$ and a force softening of $\epsilon = 5 h^{-1} \text{kpc}$. The cosmological parameters assumed were: $\Omega_0 = 0.3$, $\Omega_{\Lambda} = 0.7$, $h = 0.7$ (we adopt the standard convention $H_0 = 100 h \text{ km s}^{-1} \text{ Mpc}^{-1}$) and normalisation $\sigma_8 = 0.9$. Dark matter subhaloes are identified using the algorithm SUBFIND (Springel et al. 2001). All subhaloes containing at least 10 particles are tracked. The numerical data for each simulation are stored at 50 times logarithmically space between $1 + z = 40$ and $1 + z = 1$ and tree structures are built to follow the formation and merger history of each halo and its subhaloes.

We follow the baryonic evolution using the semi-analytic model by De Lucia et al. (2004b). As in Springel et al. (2001) the model explicitly follows the evolution of the dark matter halo within which a galaxy forms, even after this halo is accreted by a larger object and becomes one of its subhaloes. The model also follows the chemical and photometric evolution of cluster galaxies in a self-consistent way, together with the chemical enrichment of the intracluster medium. De Lucia et al. (2004b) have shown that their model agrees with a large body of observational results for galaxies in the local Universe, both in clusters and in the field. We refer to the original paper for a more detailed description. In this study, we use their ‘feedback’ model which they find to be the only one able to reproduce the observed decline in baryon fraction from rich clusters to galaxy groups.

3.3 Number density and velocity dispersion profiles for galaxies and subhaloes

A number of recent studies have focussed on the radial distribution of subhaloes within dark matter haloes (Ghigna et al. 2001; Stoehr et al. 2003; De Lucia et al. 2004a; Diemand et al. 2004; Gao et al. 2004; Gill et al. 2004). These papers all agree that the subhalo profile is shallower than that of the underlying dark matter, and indeed their subhalo profiles are all very similar. Our own results are shown in the top left panel of Fig. 3.1 in the form of average radial profiles for the dark matter and for different subhalo samples within our 10 cluster resimulations. Note that there are roughly 50 subhaloes per cluster with $M_{\text{sub}}/M_{\text{halo}} > 2 \times 10^{-4}$ or with $V_{\text{sub}}/V_{\text{halo}} > 0.09$. (The two velocities here are the maximum circular velocities of the subhalo and of the cluster respectively.) There are about 350 subhaloes per cluster with more than 30 particles, which is the limit to which Gao et al. (2004) considered the subhalo distributions to be insensitive to resolution effects. The shaded region shows the scatter of the dark matter density profiles in our simulation set. Note that all densities have been normalised to the mean density inside the virial radius. The weak concentration of the subhalo distribution relative to that of the dark matter is evident for all our samples, although, as noted by Gao et al. (2004), the profile depends on how the subhalo population is defined (limited in mass or in circular velocity). In this same panel we also plot mean profiles for our model galaxies to two different magnitude limits. In contrast to the subhalo profiles and in agreement with Diaferio et al. (2001) and Springel et al. (2001), these coincide very nicely with the mean dark matter density profile.

In the top right panel of Fig. 3.1 we plot the average projected dark matter distribution together with the surface density profile of model galaxies to two different magnitude limits.

3 Galaxies and subhaloes in Λ CDM galaxy clusters

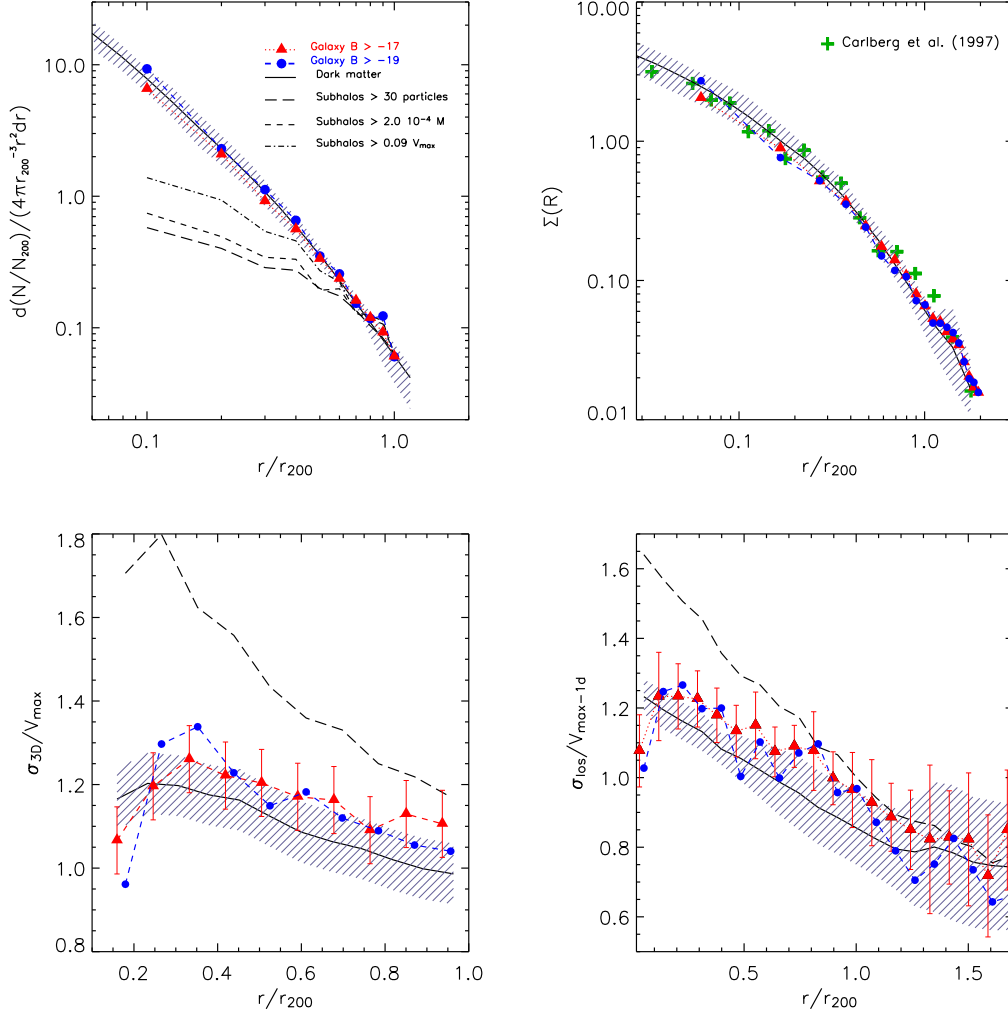


Figure 3.1: Top left: mean radial profiles for the dark matter (solid line), for model galaxies to two different magnitude limits (filled symbols), and for different subhalo samples, based on the ten clusters used in this study. Top right: mean projected surface density profiles for the dark matter (solid line) and for model galaxies to two different magnitude limits (dashed and dotted lines). The filled symbols represent the mean observed surface density profile of cluster galaxies in the CNOC survey (Carlberg et al. 1997). In these two panels, the hashed region represents the full scatter in dark matter profiles. Bottom panels: 3-D velocity dispersion profile (left) and line-of-sight velocity dispersion profile (right) for dark matter (solid line), for subhaloes containing at least 30 particles (dash line), and for model galaxies to two different limiting magnitudes. The dashed regions and error bars represent standard 1σ scatter in the dark matter and galaxy ($B < -17$) velocity dispersion profiles.

3.3 Number density and velocity dispersion profiles for galaxies and subhaloes

For comparison, we also plot the average observed surface density profile for cluster galaxies in the CNO survey (Carlberg et al. 1997). The surface density profiles for the simulations are obtained by projecting along the x , y and z axes in turn, keeping only dark matter particles and galaxies within $\pm 2R_{200}$ of cluster centre in depth, and binning up the projected density profiles out to a projected distance of $2R_{200}$. The plotted curves are then an average over three projections of each of ten simulations. The mean galaxy surface density profiles of our simulations agree extremely well both with the observational data and with the mean dark matter profile.

In the bottom panels of Fig. 3.1 we show the 3-D (left panel) and the line-of-sight (right panel) velocity dispersion profiles of dark matter particles, of galaxies and of subhaloes containing at least 30 particles. The hashed region and error bars represent the standard 1σ scatter of the dark matter and galaxy ($B < -17$) profiles among our ten resimulations. In agreement with Diemand et al. (2004) and Gill et al. (2004), we find that the velocity dispersion of the subhalo population substantially exceeds that of the dark matter, particularly in the inner regions. On the other hand, any bias in the velocity dispersions of the model galaxies are quite weak.

Fig. 3.1 clearly shows that subhaloes and galaxies have very different number density and velocity dispersion profiles in our simulations, despite the fact that we assume that a galaxy forms at the centre of each dark halo and is carried along with it when it falls into a larger system and so becomes a subhalo. What is the origin of these differences? If one wants to relate the properties of subhaloes to those of the galaxies residing within them, the evolution of the baryonic component has to be tracked appropriately. This necessarily involves consideration of the full collapse, assembly, merging and tidal stripping history of each subhalo, rather than just its properties at the final time. Such tracking can be carried out conveniently and moderately realistically using semi-analytic techniques, as is done in this work.

Note that many of the model galaxies used to construct Fig. 3.1 are not associated with any resolved dark matter subhalo. In pure dark matter simulations subhaloes can disappear once their mass falls below the resolution limit of the simulation. It may be that their dark matter content should indeed be reduced to such small values by tidal stripping, or it may be that proper inclusion of the effects of the baryonic component would make them more resistant to stripping and disruption, as originally envisaged by White & Rees (1978). Our semi-analytic model assumes that the visible galaxy survives even if the mass of the corresponding subhalo drops below the limit of our N-body simulation. We associate the galaxy with the most bound particle of its subhalo at the last time this could be identified, and we use this particle at later times to track the galaxy's position and velocity. Such 'orphan' galaxies behave as individual N-body particles although we assume them to merge with the central galaxy of the cluster on a dynamical friction time-scale. They are responsible partly for the large differences between the 'galaxy' and 'subhalo' profiles in the inner regions of our clusters.

As discussed in Gao et al. (2004), the infall time and the retained mass of a subhalo are both strongly increasing functions of clustercentric radius. This implies that subhaloes in the inner regions of cluster haloes today were generally more massive in the past than similar mass but more recently accreted subhaloes in the outer regions. As first shown by Springel et al. (2001), this produces an increasing mass-to-light ratio as a function

3 Galaxies and subhaloes in Λ CDM galaxy clusters

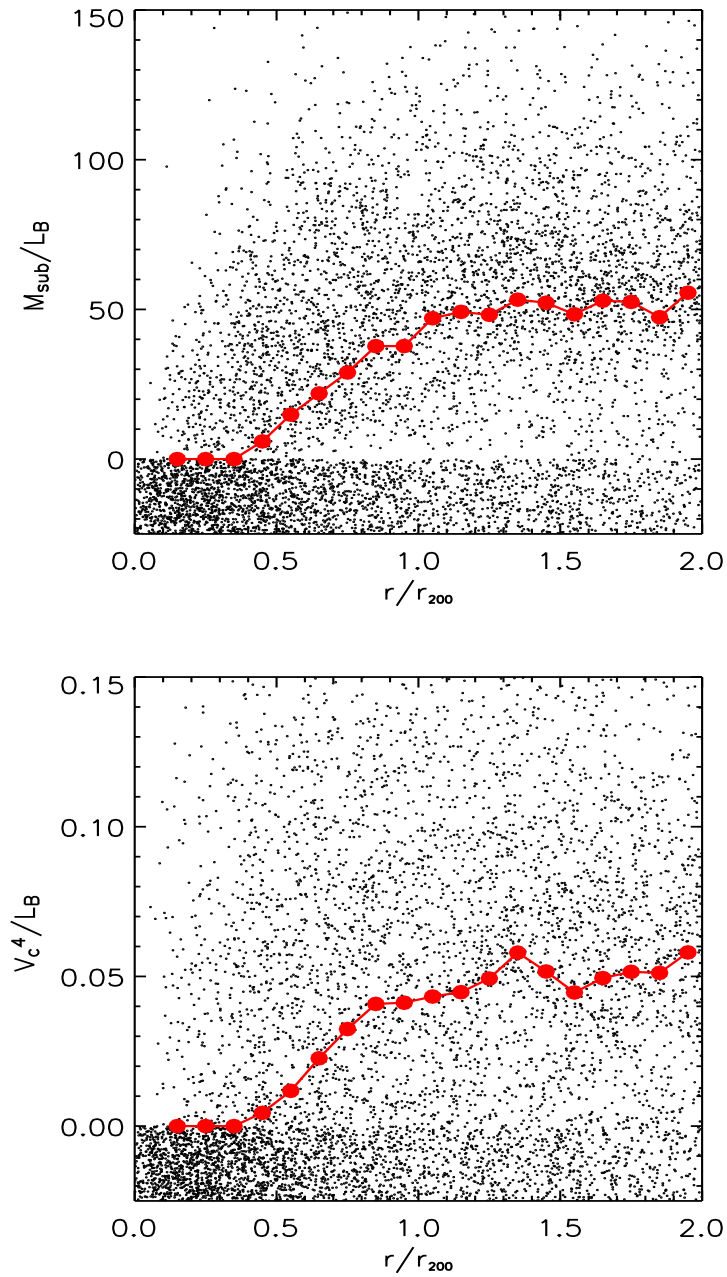


Figure 3.2: Mass-to-light ratio (left) and (circular velocity)⁴-to-light ratio (right) for model galaxies brighter than $B = -17$ as a function of distance from cluster centre. Thick lines show median values as a function of radius. Galaxies that are not associated with any dark matter subhalo are assigned zero mass and circular velocity, but are displayed with a randomly generated small negative value of the ordinate so that they are visible in the plots.

of the clustercentric distance. We show this for our present models in Fig. 3.2 where we plot mass-to-light ratio (M/L_B) and (circular velocity)⁴-to-light ratio (V^4/L_B) for our model galaxies as a function of distance from cluster centre. Galaxies brighter than $M_B = -17$ from all ten resimulations are shown here. The velocity used in the right panel is defined as the maximum circular velocity of the associated subhalo. Outside the virial radius, these ratios are almost flat, reflecting the proportionality between the halo mass (or circular velocity to the fourth power) and the galaxy luminosity for isolated haloes (the Tully-Fisher relation). About 60 per cent of the galaxies brighter than $M_B = -17$ are not associated to any resolved subhalo, and so are assigned zero mass and circular velocity. Note, in this plot, in order to show the density distribution of those ‘orphan’ galaxy, we plot mass-to-light ratio for them vary randomly from -25 to 0 , and (velocity-to-light)⁴ from -0.025 to 0 , respectively. Springel et al. (2001) show that this trend is present at a similar level in a simulation with almost ten times better resolution than those we use here. In addition, numerical convergence studies by Diemand et al. (2004) and by Gao et al. (2004) indicate that resolution effects on subhalo mass are relatively small for subhaloes with more than 30 particles and so cannot be responsible for the trends in Figure 2.

The radial variation of the mass-to-light ratio of cluster galaxies reflects the fact that tidal stripping is very efficient in reducing the masses of subhaloes within larger systems but is assumed to have much less effect on the luminosity and structure of the galaxies which reside at their centres. In such a situation, selecting subhaloes above a certain mass (or circular velocity) results in a population with very different properties from a galaxy population selected above a certain limiting magnitude.

3.4 Summary and discussion

In this Letter, we have implemented a semi-analytic treatment of galaxy formation on ten high resolution resimulations of galaxy cluster evolution in order to study the number density and velocity dispersion profiles predicted for galaxies and for dark matter subhaloes in Λ CDM galaxy clusters. In agreement with previous work, we find galaxy profiles that agree well both with simulated dark matter profiles and with observed galaxy profiles, but subhalo profiles with much weaker central concentration and with substantially higher velocity dispersion.

We show that these differences are due to a strong increase in the mass-to-light (or (circular velocity)⁴-to-light) ratio of galaxies as a function of the distance from cluster centre. This trend is caused by tidal stripping which rapidly reduces the mass of dark matter subhaloes once they are accreted onto a larger structure, while only weakly affecting the galaxies at their centres. In related work, De Lucia et al. (2004a) and Gao et al. (2004) examine in considerably more detail the efficiency of tidal stripping, showing that the longer a substructure spends in a massive halo, the larger is the destructive effect. As they demonstrate explicitly, subhaloes are constantly being erased and being replaced by newly infalling haloes. Our semi-analytic models assume that this process does not, however, destroy the galaxy at the centre of each subhalo, which has typically accumulated a substantial and strongly bound stellar component during early evolutionary stages.

Much of the work on substructure within dark matter haloes has attempted to link

3 Galaxies and subhaloes in Λ CDM galaxy clusters

simulated substructure to observed galaxies by assuming a constant mass-to-light ratio for subhaloes or by relating their maximum circular velocity to galaxy luminosity through the observed Tully–Fisher and Fundamental Plane relations. Our results show clearly, as did the earlier results of Springel et al. (2001) that such assumptions are very unlikely to give realistic results. Galaxies and subhaloes are not simply related. The luminosity of a galaxy cannot be inferred from the $z = 0$ properties of the subhalo which corresponds to it in a dark-matter-only N-body simulation. Indeed, many cluster galaxies have *no* corresponding subhalo in such a simulation, even though the haloes in which they originally formed were easily resolved by the simulation. The galaxy formation process must be treated appropriately to get results which are even qualitatively correct.

We note that these issues will not be addressed by carrying out dark matter simulations of higher resolution. The tests of Diemand et al. (2004) and Gao et al. (2004) show that subhaloes can be followed and their masses tracked at least roughly down to a limit of 20 particles or so, corresponding to subhalo masses around $10^{10}M_{\odot}$ for the simulations in this paper. This is below the observed *stellar* mass of the galaxies in the real samples with which we are comparing our models. Thus dynamical evolution becomes dominated by the visible components of galaxies before our simulations run into resolution problems. Any improvement over our current simple semi-analytic assumptions will require explicit modelling of structure in the stellar component of cluster galaxies.

Finally we note that although this paper has dealt with cluster-sized haloes only, the same caveats apply also to galaxy- and group-sized haloes. Only through a full treatment of the baryonic physics, is it possible to carry out a detailed comparison between theoretical results and observational data. A complex network of actions and back-reactions regulates the evolution of the galaxy components we see, and any comparison of simulated subhaloes to observed galaxies must consider the time-integrated effect of these processes or risk serious error.

Acknowledgements

The simulations used in this paper were carried out on the Cosma supercomputer of the Institute for Computational Cosmology at the University of Durham. GL thanks Yipeng Jing and Xi Kang for useful discussion. G. D. L. thanks the Alexander von Humboldt Foundation, the Federal Ministry of Education and Research, and the Programme for Investment in the Future (ZIP) of the German Government for financial support.

References

- Biviano A., Girardi M., 2003, ApJ, 585, 205
- Carlberg R. G., Yee H. K. C., Ellingson E., 1997, ApJ, 478, 462
- Desai V., Dalcanton J. J., Mayer L., Reed D., Quinn T., Governato F., 2004, preprint, astro-ph/0311511
- D’Onghia, E. & Lake, G., 2003, ApJL submitted, preprint, astro-ph/0309735
- De Lucia G., Kauffmann G., Springel V., White S. D. M., Lanzoni, B., Stoehr, F., Tormen, G., Yoshida, N., 2004a, MNRAS, 348, 333
- De Lucia G., Kauffmann G., White S. D. M., 2004b, MNRAS, 349, 1101
- Diaferio A., Kauffmann G., Michael B., White S. D. M., Schade D., Ellingson E., 2001, MNRAS, 323, 999
- Diemand, J., Moore, B., Stadel, J., 2004, preprint, astro-ph/0403160
- Gao, L., Loeb, A., Peebles, P. J. E., White, S. D. M., Jenkins, A., 2003, preprint, astro-ph/0312499
- Gao, L., White, S. D. M., Jenkins, A., Stoehr, F., Springel, V., 2004, preprint, astro-ph/0404589
- Ghigna S., Moore B., Governato F., Lake G., Quinn T., Stadel J., 2000, MNRAS, 544, 616
- Gill S. P. D.I, Knebe A., Gibson B. K, Dopita M. A., 2004a, MNRAS in press, preprint, astro-ph/0404255
- Gill S. P. D.I, Knebe A., Gibson B. K., 2004b, MNRAS in press, preprint, astro-ph/0404258
- Kauffmann G., Colberg J. M., Diaferio A., White S. D. M., 1999, MNRAS, 303, 188
- Klypin A., Gottloeber S., Kravtsov A. V., Khokhlov A., M., 1999, ApJ, 1999, 516, 530
- Klypin A., Kravtsov, A. V., Valenzuela, O., Prada F., 1999a, ApJ, 522, 82
- Kravtsov A. V., Gnedin O. Y., Klypin A. A., 2004, ApJ submitted, preprint, astro-ph/0401088
- Moore B., Ghigna S., Governato F., Lake G., Quinn T., Stadel J., Tozzi P., 1999 ApJ, 524, 19

References

- Navarro J. F., Hayashi E., Power C., Jenkins A., Frenk C. S., White S. D. M., Springel V., Stadel J., Quinn T. R., 2004, MNRAS, astro-ph/0311231
- Power C., Navarro J. F., Jenkins A., Frenk C. S., White S. D. M., Springel V., Stadel J., Quinn T., 2003, MNRAS, 338, 14
- Spergel D.N. et al., 2003, ApJS, 148, 175
- Springel V., Yoshida N., White S. D. M., 2001a, New Ast. 6, 79
- Springel V., White S. D. M., Tormen G., Kauffmann G., 2001b, MNRAS, 328, 726
- Stoehr F., White S. D. M., Tormen G., Springel V., 2002, MNRAS, 335, L84
- Stoehr F., White S. D. M., Springel V., Tormen G., Yoshida N., 2003, MNRAS, 345, 1313
- Tormen G., 1997, MNRAS, 290, 411
- White S. D. M., Rees M. J., 1978, MNRAS, 183, 341
- Yoshida N., Sheth R. K., Diaferio A., 2001, MNRAS, 328, 669

4 Earlier formation and later merging of the Giant Galaxies

Abstract

The most luminous galaxies in the present Universe are found at the centers of the most massive dark matter haloes, rich galaxy clusters. In the Λ CDM cosmology, such massive halo cores are present at redshift $z = 6$ with a comoving number density (as a function of mass interior to ~ 10 kpc) that is comparable to today's value. The identity of the matter in these central regions is, however, predicted to change as major mergers bring together stars and dark matter from initially well separated sub-units. We use N-body simulations to show that these mergers push pre-existing matter outwards in the dominant galaxy, preserving the inner density profile of collisionless matter. It appears that the central regions of large galaxies end up dominated by stars formed in a number of dense cores, well before the last major mergers. The density profile of collisionless matter (stars and dark matter combined) in these central regions appears to be stable and to have attractor-like behavior under merging. This suggests that the baryon loading associated with dissipative contraction and star formation may be erased as subsequent mergers drive the mass distribution back to a universal profile. Such suppression of the effects of baryon loading, along with the early assembly of mass concentrations, may help resolve some apparent challenges to the CDM model for structure formation.

4.1 Introduction

Recent merger-driven evolution of the most massive galaxies was under discussion well before the introduction of the Cold Dark Matter (CDM) model for structure formation (see for example Toomre & Toomre 1972, §VII.b; Ostriker & Tremaine 1975), and has long been recognized as an important process within the CDM model (Frenk et al. 1985). A less widely discussed aspect of this model is that dark matter halos with characteristic velocities and comoving number densities characteristic of the luminous parts of large galaxies form at redshifts well above unity (Loeb & Peebles 2003). The dichotomy – very significant events in the history of the massive galaxies at low and high redshift – may be mirrored in the observational data: there is clear evidence for merging and evolution beyond aging of the star populations at redshift $z < 1$, and clear evidence also for the presence of giant galaxies with old star populations at redshifts well above unity (Conselice et al., 2003).

We discuss the relation between these two aspects of galaxy formation in the CDM model by combining arguments based on analytic fitting functions and on direct numerical N-body simulations. The early formation of mass concentrations similar to those in the luminous parts of the most massive present-day galaxies is reviewed in §2. In §3 we present Λ CDM

4 Earlier formation and later merging of the Giant Galaxies

simulations which have sufficient resolution to follow the assembly of the regions which house the central dominant galaxy in observed rich clusters. The details of this assembly are analyzed in §4. Mergers among massive halos at redshifts between 0.5 and 4 bring more matter into the innermost 10 kpc than remains from the dominant progenitor at higher redshift. Logical and observational consistency with the early formation of massive systems leads to three conditions. First, most of the matter present in the centers of the dominant halos at $z = 6$ has to be displaced outwards during mergers. We show this effect in the simulations. Second, the hierarchy of mergers has to preserve the stellar concentration within radii ~ 10 kpc. This may reflect the fact that in merger simulations the dense regions (where stars seem most likely to form) tend to end up in the dense regions of the merger remnant. We present in §4 a statistical measure that illustrates this preservation effect. Third, the characteristic density profile of a virialized halo of collisionless matter has to be stable under a sequence of disturbances from major mergers. As discussed in §4.3, this attractor effect is supported by the simulations. An important observational consequence may be the suppression of the adiabatic baryon loading associated with gas cooling and star formation.

Our central conclusion is that in the Λ CDM cosmology giant galaxies exist at redshift $z = 3$ with close to the present comoving number density, in terms of the total mass measured within physical radius $r \sim 10$ kpc. At this time they may have up to half the present star mass in this region. This would be quite different from the indications from at least some semi-analytic models for galaxy formation (e.g. Baugh et al. 1998, figure 13), but in line with a considerable variety of – though not all – observational indications (as reviewed in Peebles 2002). Further considerations on whether our interpretation of the Λ CDM model agrees with the observations are presented in §5.

Throughout this paper, we assume the standard Λ CDM cosmological parameters $\Omega_m = 0.3$, $\Omega_\Lambda = 0.7$, $\Omega_b = 0.04$, $\sigma_8 = 0.9$, $n = 1$, and Hubble constant $H_0 = 100h$ km s⁻¹ Mpc⁻¹ with $h = 0.7$.

4.2 Formation of Mass Concentrations Characteristic of the Most Massive Galaxies

Analytic fitting functions can be combined with analytic formulae for halo abundance to make Λ CDM predictions for the characteristic mass density run in rare, very massive halos. In Figure 4.1 we show results for halos assumed to have a fixed comoving number density, corresponding to physical density $n = 10^{-7}a(t)^{-3}$ Mpc⁻³; the profiles are plotted at redshifts corresponding to factor of two steps in the cosmological expansion factor $a = (1+z)^{-1}$. The most striking impression from this plot is how little the mass distribution changes in the inner regions after $1+z = 8$. Fukushige & Makino (2001) were led by their numerical simulations to propose that that the run of density in physical units in the inner power law part is approximately independent of time, a behavior suggested previously by the simple theoretical model of Syer & White (1998) for the assembly of halos through merging. Loeb & Peebles (2003) were independently led to the same proposal from the fitting function analysis in Figure 4.1.

This figure, computed as described in Loeb & Peebles (2003), is based on the Press-

4.2 Formation of Mass Concentrations Characteristic of the Most Massive Galaxies

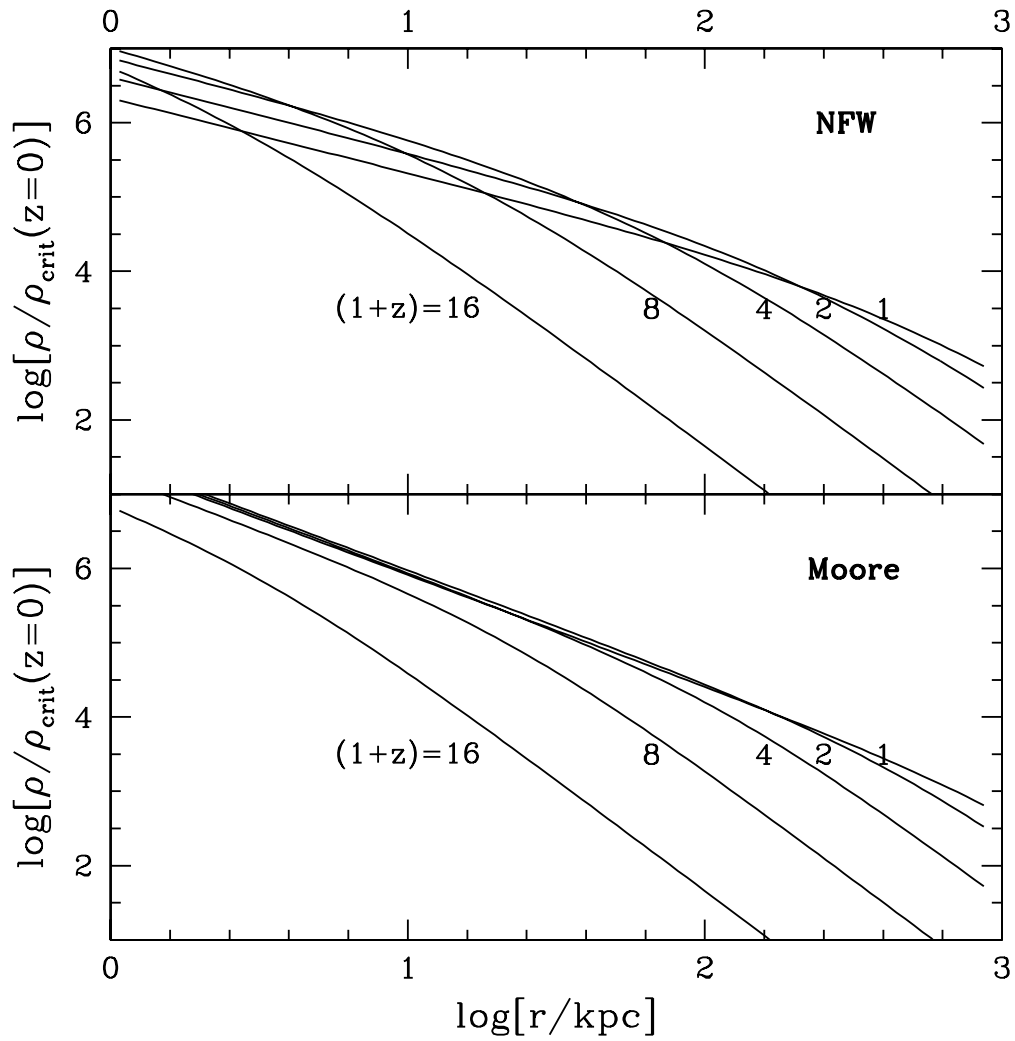


Figure 4.1: Density runs at various redshifts for halos with comoving density $n(> M) = 10^{-7} \text{ Mpc}^{-3}$. Physical rather than comoving units are used both for the radius and for the density.

4 Earlier formation and later merging of the Giant Galaxies

Schechter mass function (including the modification by Sheth & Tormen 1999; see also Sheth, Mo & Tormen 2001) and analytic density profiles. The Navarro, Frenk, & White (1997, hereafter NFW) shape with concentration parameter $c = 4$ is used in the top panel, while the Moore (Moore et al. 1999; Ghigna et al. 2000) profile with concentration $c = 4/1.72$ is used in the bottom panel. (See Klypin et al. 2001 for the conversion factor, 1.72, between the two profiles.) Clearly, the mass in the inner $10h^{-1}$ kpc of these rare halos is predicted to evolve very little for $z \lesssim 6$. That is, according to the Λ CDM model, massive cores similar to those which house the largest present-day galaxies already existed just one billion years after the Big Bang. We will see in the next section that our simulations of Λ CDM bear out this result from the fitting functions.

4.3 High Resolution Simulations of Massive Halo Assembly

The numerical results in this paper are based on a set of 8 simulations of the formation of a massive galaxy cluster halo in our standard Λ CDM model. These 8 halos, which are part of the suite of simulations analysed in Navarro et al (2003), range in virial mass between $4.5 \times 10^{14}h^{-1}M_{\odot}$ and $8.5 \times 10^{14}h^{-1}M_{\odot}$. They are chosen from a simulation of a representative cubic region of side $479h^{-1}\text{Mpc}$ (the VLS simulation of the Virgo Consortium, see Jenkins et al. 2001 and Yoshida Sheth & Diaferio 2001), which contains 41 halos with mass exceeding $4.5 \times 10^{14}h^{-1}M_{\odot}$. Our objects thus have an effective abundance of $3.7 \times 10^{-7}h^3\text{Mpc}^{-3}$. This is the observed present-day abundance of galaxies with luminosity greater than $8L_*$. Almost all such systems are indeed the central dominant galaxies within rich clusters.

We resimulated each of our 8 halos, as in Navarro, Frenk & White (1997), with greatly improved resolution in the cluster and its immediate environment and with degraded resolution outside this region. The mass of an individual dark matter particle in the high resolution region is $5.12 \times 10^8h^{-1}M_{\odot}$ and the gravitational softening parameter is $5.0h^{-1}$ kpc in comoving units. The simulations were carried out with the publicly available parallel N-body code GADGET (Springel, Yoshida & White 2001).

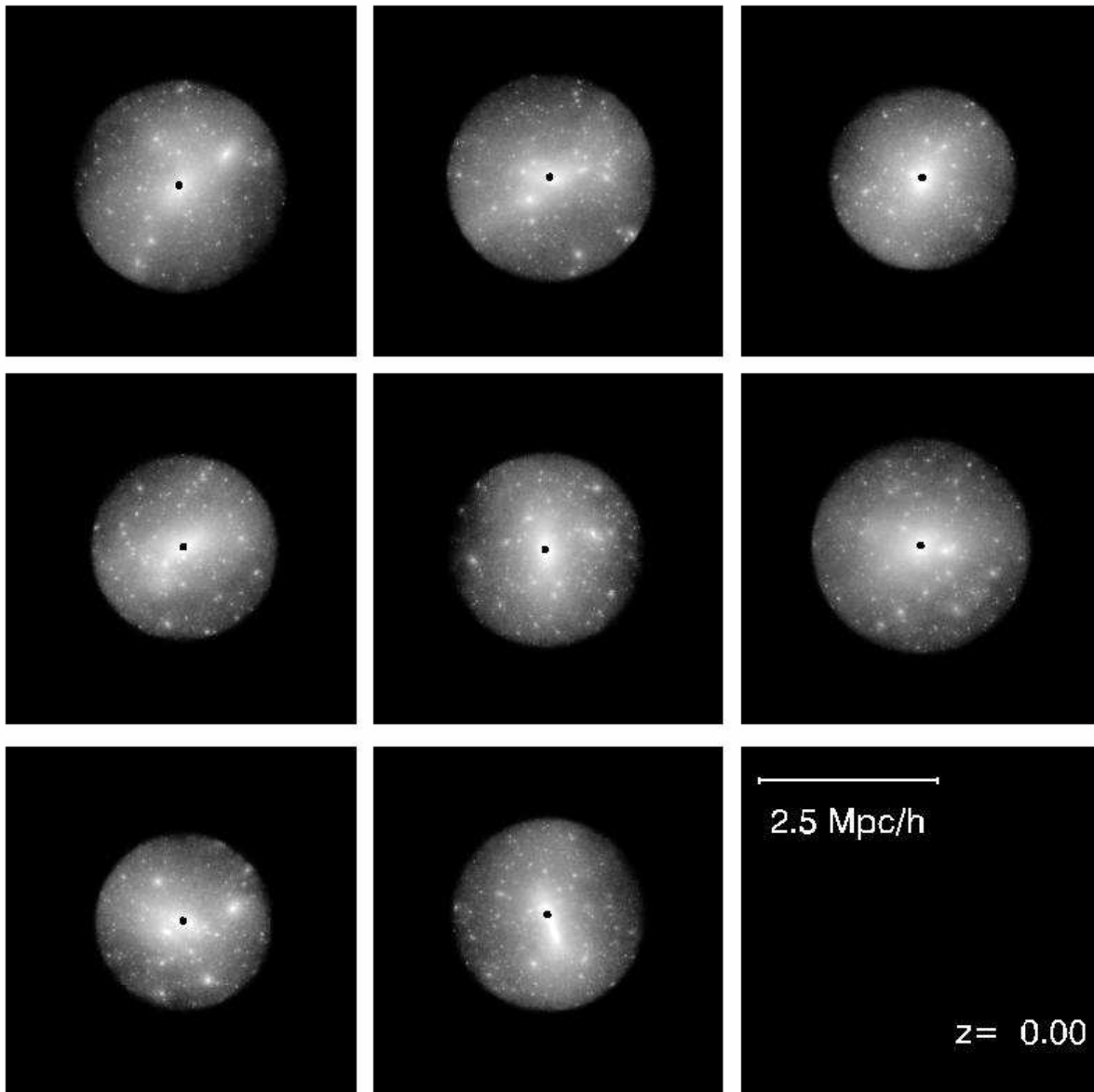
We show images of the evolution of the mass distribution in these 8 halos in Figure 4.2. The three sets of panels show the halo material at three different redshifts, $z = 0, 1$ and 3 . Each panel is $5h^{-1}\text{Mpc}$ across in physical (not comoving) units. Each shows only the matter which is within r_{200} of the cluster center at $z = 0$, so that the same particles are used to make corresponding images in each of the three sets. As usual, we define r_{200} to be the radius within which the mean enclosed density is 200 times the critical value. It is striking that although all the halos are centrally concentrated and relatively regular at $z = 0$, the material which makes them up was in all cases in several disjoint and well separated pieces at $z = 1$ and was in many pieces at $z = 3$.

In the images in Figure 4.2 the particles which lie within $10h^{-1}$ kpc of halo center at $z = 0$ are shown in black in all three sets. It is remarkable that in all cases these particles also come from several different objects at $z = 3$. The same is true even at $z = 1$ in many cases. We analyse the details of core assembly in more detail in the next section.

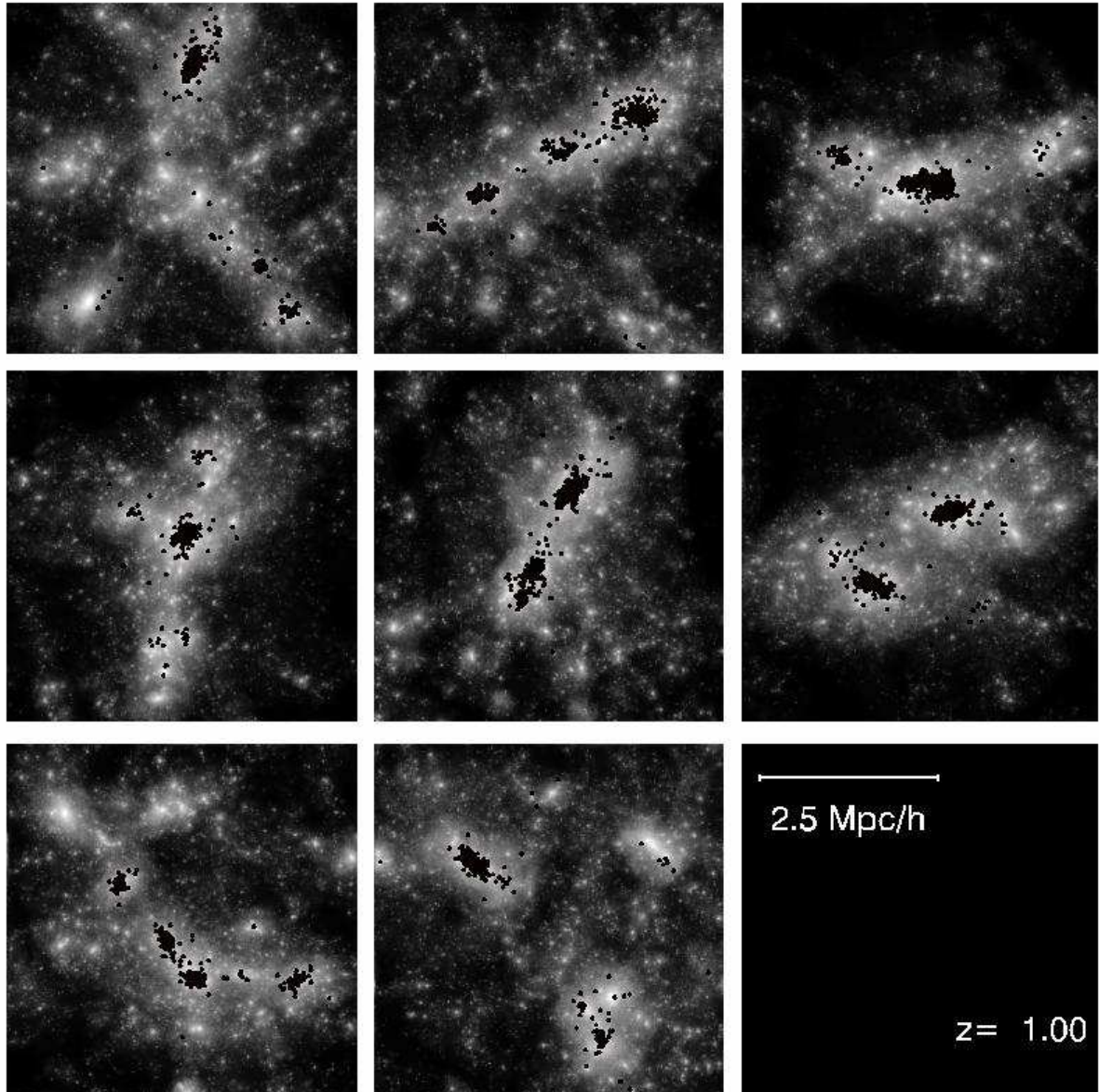
The stability of the central mass concentrations predicted in §2 can be seen directly in these simulations. Figure 4.3 shows the mass within physical radius $r = 10h^{-1}$ kpc around the center of the most massive progenitor of the final halo at discrete time steps and in each

4.3 High Resolution Simulations of Massive Halo Assembly

of the 8 simulations. Notice that the vertical axis is linear in these plots. The variations in mass are relatively small and show no consistent trend for $a > 0.15$, corresponding to $z < 6$. This is in good agreement with Figure 4.1. That is, the CDM model predicts that at $z < 6$ there is little evolution of the mass within a radius characteristic of the luminous parts of the largest galaxies. Note, however, that the object plotted in each panel is *not* the same at each time: the most massive progenitor of a cluster at $z = 6$ does not necessarily evolve into its most massive progenitor at $z = 4$ which may not evolve into its most massive progenitor at $z = 2$. We indicate this effect in the plots; working back from $z = 0$, we toggle the plotting symbol between filled and open each time the most massive progenitor changes identity.



4 Earlier formation and later merging of the Giant Galaxies



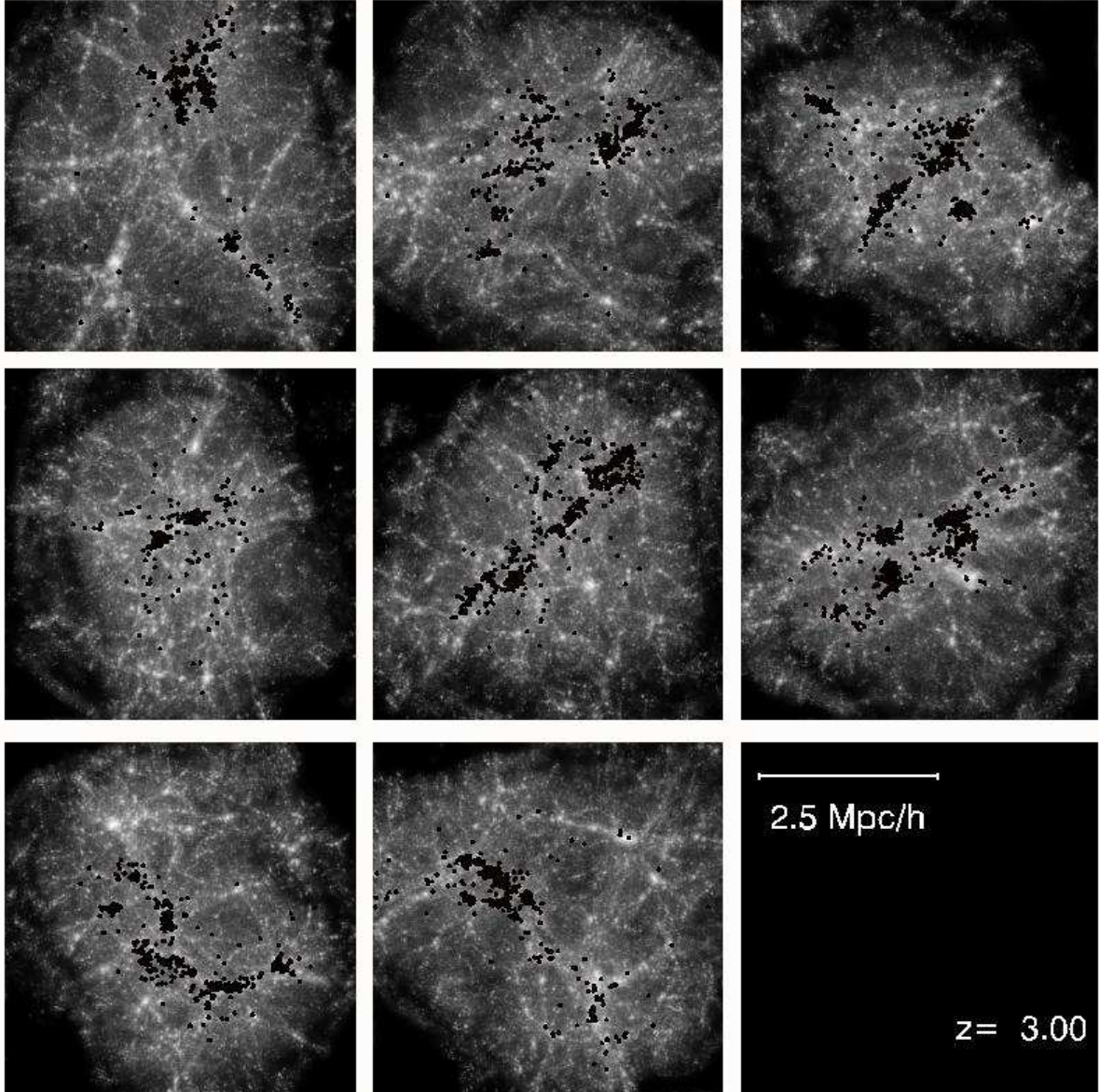


Figure 4.2: Images of the mass distribution at $z = 0, 1$ and 3 in our 8 simulations of the assembly of cluster mass halos. Each plot shows only those particles which lie within r_{200} of halo center at $z = 0$. Particles which lie within $10h^{-1}$ kpc of halo center at this time are shown in black. Each image is $5h^{-1}\text{Mpc}$ on a side in physical (not comoving) units.

4 Earlier formation and later merging of the Giant Galaxies

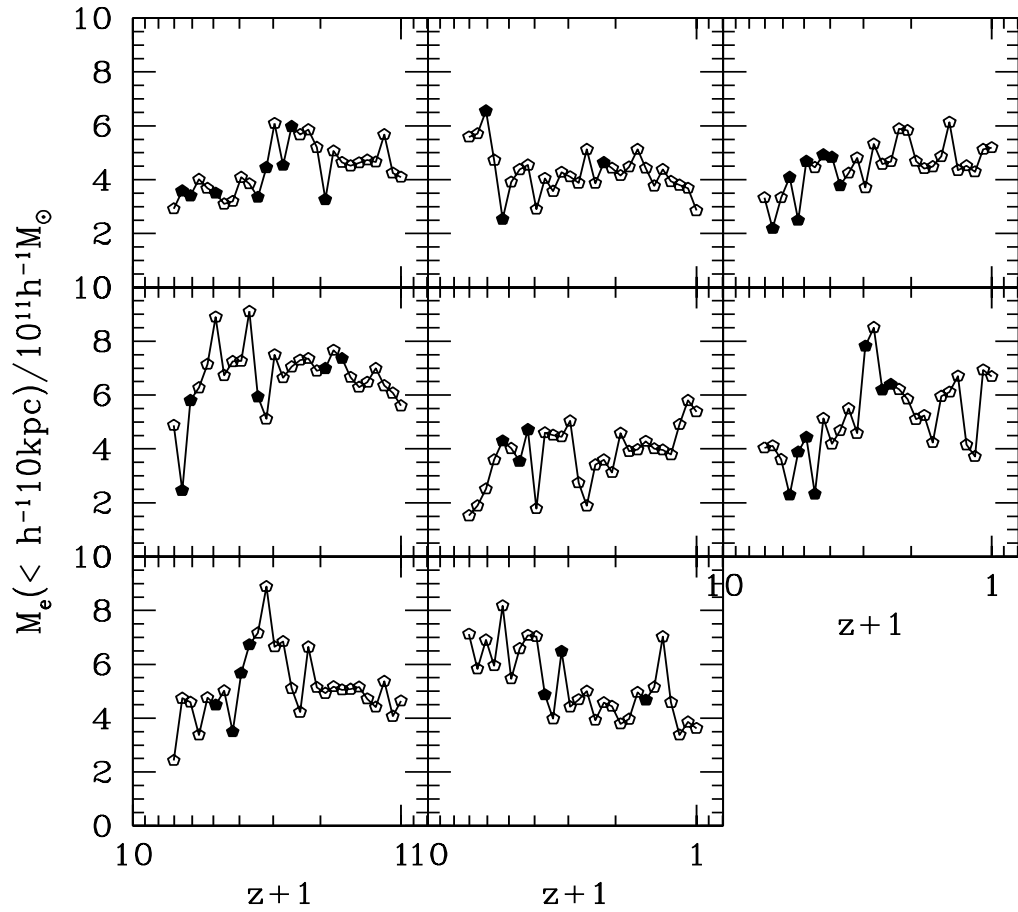


Figure 4.3: The total mass within physical distance $10h^{-1}$ kpc of the center of the most massive progenitor of the final halo at each time plotted and for each of our 8 simulations. Symbols switch between filled and open each time the identity of the most massive progenitor changes.

4.4 Mergers and Relaxation at Low Redshifts

In this section, we consider the predicted rearrangement of matter in the cores of pure CDM halos at low redshift, and then discuss why the stars in giant galaxies might be expected to remain concentrated in the centers of the halos as observations require. Finally, we consider the idea that the net mass distribution in stars plus dark matter, both considered as collisionless particles, tends to relax toward the NFW form.

4.4.1 Rearrangements of the Dark Matter

Loeb & Peebles (2003) discuss the evolution of the halo structure shown in Figure 4.1 in terms of an “inside-out” growth process, whereby mass is added to galaxies in “onion shells” with declining density as a function of cosmic time. This can indeed reproduce the behavior in Figure 4.1, but cannot be the entire story because, as Figure 4.2 shows, late mergers add material even to the very center of the main halo and so must affect the distribution of the other matter there.

Figure 4.4 makes this point more quantitatively. We identify the particles which are within $10h^{-1}$ kpc of the center of each cluster halo at $z = 0$, and we then follow them back in time. The circles in each panel show the fraction of these particles which are already within $100h^{-1}$ kpc (physical) of the center of their dominant concentration at each earlier redshift. (We identify the center of this dominant concentration by calculating the gravitational potential of each particle in the set due to all the others, and then choosing the most bound particle.) Note that the dominant concentrations used to make this plot are often not the most massive progenitors which were used to make Figure 4.3. Both figures illustrate the point that, in the Λ CDM model, mergers at low redshifts have a substantial effect on the innermost regions of large halos. Only 20–50% of the mass that now lies within $10h^{-1}$ kpc of the center of a massive halo was closer than $100h^{-1}$ kpc to their dominant concentration at $z = 6$, and typically no more than 50% was closer than $100h^{-1}$ kpc at $z = 2$. The rest of the mass was added to the cores by late mergers. These major mergers are visible in Figure 4.4 as abrupt changes in $F(z)$ which are often accompanied by large fluctuations in the mass within $10h^{-1}$ kpc.

The matter present in the central $10h^{-1}$ kpc of each massive concentration at high redshift must have been displaced to make room for the matter subsequently added by mergers. We illustrate this process in Figure 4.5. We start by selecting all particles within $10h^{-1}$ kpc (physical) of the center of the most massive progenitor of each halo at $z = 6$. Since many of these particles have apogalactica well outside $10h^{-1}$ kpc, we plot their cumulative radial distributions at $z = 5.5$ after they have had time to phase-mix around their orbits. We then identify this same set of particles at a series of later times and plot the cumulative radial distribution about the center of their dominant concentration. (This center is defined as the most bound particle of the set, as above.) One sees a systematic trend for these distributions to broaden with time, the median distance typically increasing by a factor of about two from $z = 4$ to the present. Notice, however, that in two of the eight cases the dominant concentration of these particles at $z = 0$ is *not* at the center of the main halo, but at the center of one of its more massive subhalos.

The late assembly of the matter which does finally end up at halo center is illustrated

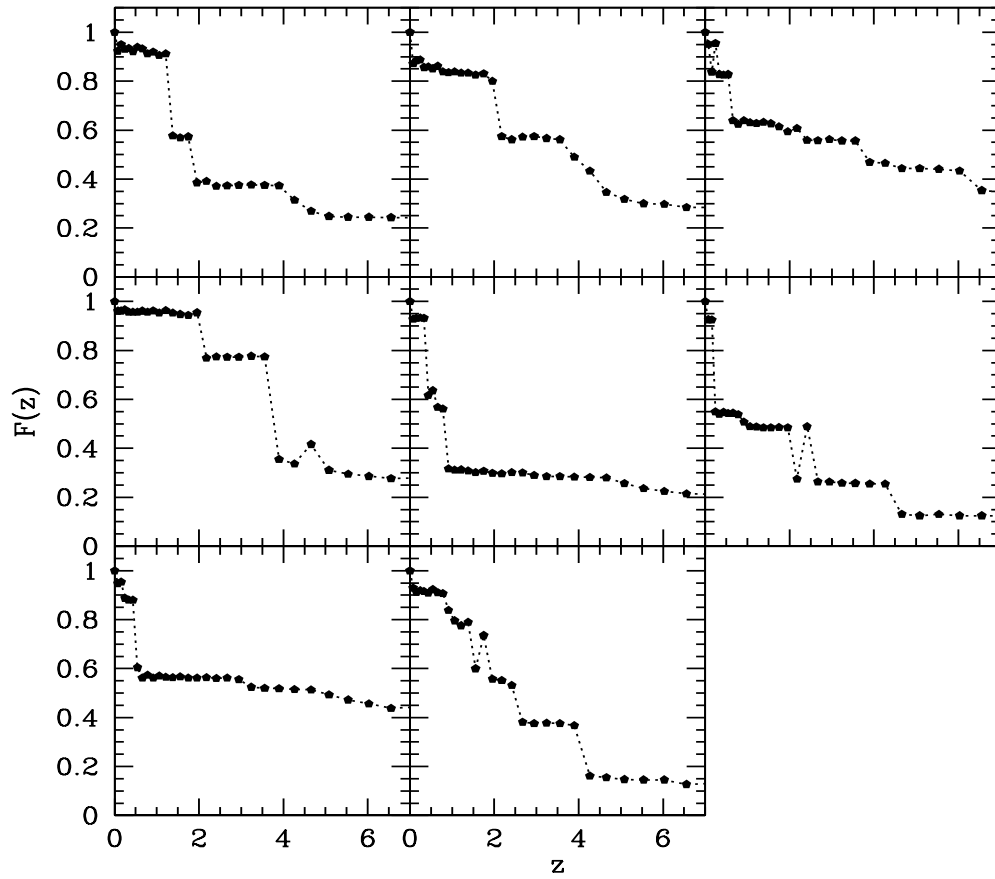


Figure 4.4: History of addition of the matter now in the central parts of massive halos. The black curves show the fraction of the particles at $r < 10h^{-1}$ kpc at $z = 0$ which lie within $100h^{-1}$ kpc (physical) distance from the center of their main concentration at each earlier redshift z .

by the complementary plot in Figure 4.6. Here we again select all particles which are within $10h^{-1}$ kpc of halo center at $z = 0$ and then plot cumulative radial distributions about the center of their dominant concentration at a series of earlier times. (These are the same particle sets and center definitions used to make Figure 4.4.) We plot the lowest redshift curves for $z = 0.07$ rather than for $z = 0$ in order to show a properly phase-mixed, quasi-equilibrium distribution. There is little evolution subsequent to $z = 0.33$ in 7 cases, subsequent to $z = 1$ in 3 cases, and subsequent to $z = 2$ in one case. At higher redshifts, however, substantial fractions of the particles are further than $100h^{-1}$ kpc from center of the dominant concentration in all cases. This behavior reflects the late addition of matter to the cores of the galaxies, as already illustrated in Figure 4.4.

4.4.2 The Distributions of Stars

The star populations in giant ellipticals are typically old (a familiar and well established observation, as evidenced by the discussions by Oke 1971, 1984 and Hamilton 1985; for recent data see Bernardi et al. 2003). Once formed, stars behave dynamically as collisionless matter. Since stars make substantial contributions to the mass within the half-light radii $r_e \lesssim 10h^{-1}$ kpc of massive galaxies (Romanowsky et al. 2003, and references therein) merger-driven rearrangements of matter must not have substantially diluted the central concentrations of stars by the addition of nonbaryonic dark matter. A full analysis of the predicted effect of dilution is beyond the scope of this paper – and perhaps beyond what is now computationally feasible – but we can offer two simple relevant considerations. First, the condition that dilution is modest is in line with the familiar tendency in numerical simulations for the dense parts of merging halos to end up in the dense parts of the merger remnant (White 1980; Barnes 1992; Dubinski 1998).

The second consideration is based on the same sets of particles already used in Figures 4.4 and 4.6, namely those particles that are within $r < 10h^{-1}$ kpc of the center of each dominant halo at $z = 0$. Figure 4.7 shows the evolution with redshift of the cumulative distribution of ambient physical density around each of these particles, estimated by means of a standard SPH spline kernel which averages over the positions of the 25 nearest neighbors. Note that the final time shown is $z = 0.07$ rather than $z = 0$ so that the particle distribution is properly phase-mixed. The median ambient density around this particle set increases by a factor of about six from $z = 6$. This is a result of our selection procedure, which preferentially picks out those particles which have been scattered into the most strongly bound orbits by 2-body effects and by the violent relaxation which accompanies merging. The median ambient density for these particles at $z = 6$ is typically about $5 \times 10^6 M_\odot \text{kpc}^{-3}$, which is 500 times the mean density at that epoch. The matter now in the central regions of a giant galaxy was thus already in the inner regions of virialised objects at $z = 6$, and hence could have experienced substantial star formation at that time.

This mixing process is explored in a different way in Figure 4.8. Among all the particles that lie within r_{200} in each final cluster we identify the 1000 which have the largest ambient density at $z = 6$. We then plot cumulative ambient density distributions for these particle sets at lower redshifts beginning with $z = 5.53$. These distributions broaden with time as relaxation scatters particles into lower density regions. At $z = 0$ their median ambient density is typically $3 \times 10^6 M_\odot \text{kpc}^{-3}$, which is a factor 9 smaller than at $z = 5.5$ but still 10^5

4 Earlier formation and later merging of the Giant Galaxies

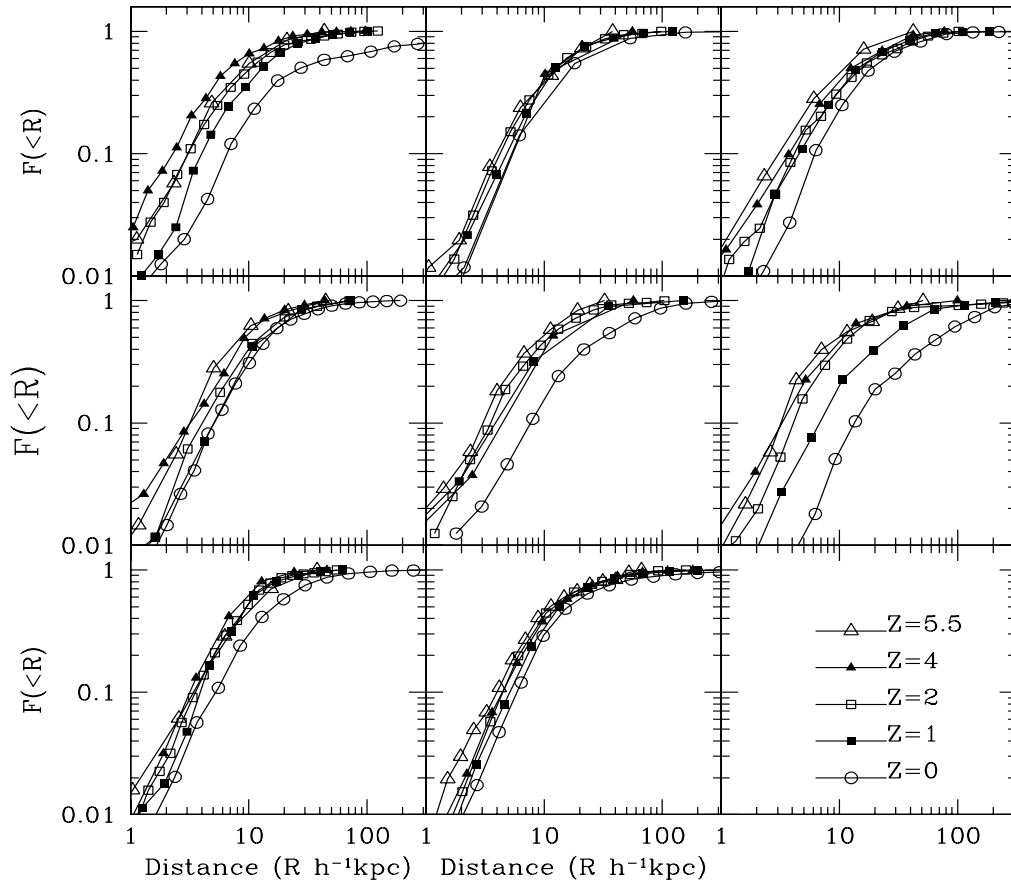


Figure 4.5: Cumulative radial distributions at a series of later redshifts for the particles that were within $10h^{-1}$ kpc of the center of the most massive $z = 6$ progenitor of each cluster halo. Distances are all in physical units and are measured from the center of the dominant concentration of each particle set at each redshift. Note that for the middle clusters in the top and bottom rows (numbers C2 and C8) this dominant concentration does not coincide with the cluster center at $z = 0$ but with one of the more massive substructures.

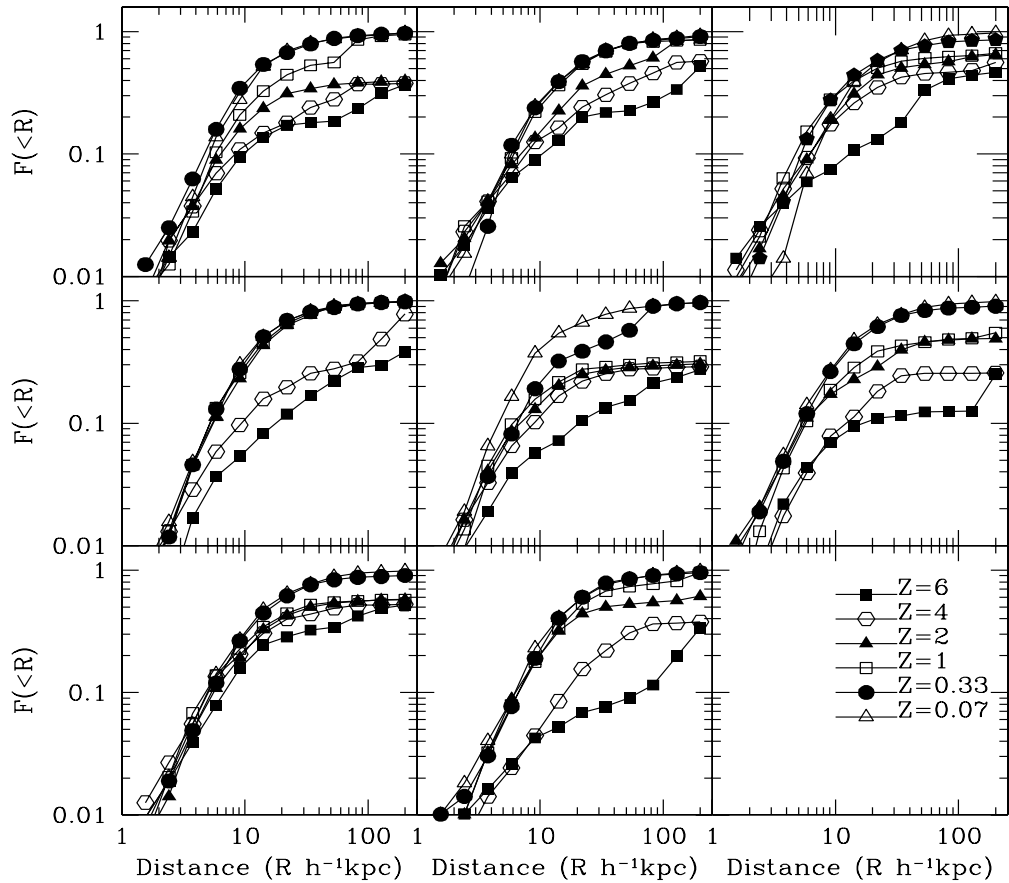


Figure 4.6: Evolution of cumulative radial distributions, as in Figure 4.5, but now for particles which are within $10h^{-1}$ kpc of halo center at the final time, $z = 0$. These are same particle sets (with the same definition of density center) already used to make Figure 4.4.

4 Earlier formation and later merging of the Giant Galaxies

times the present cosmic mean density. Note that much of this broadening occurs between $z = 1$ and $z = 0$, and is actually a consequence of 2-body scattering. In simulations of even better mass resolution, we would expect the reduction in density at late times to be significantly lower. It is important to realise, however, that not all these “dense” particles from high redshift end up in the central “galaxy”. Typically about 40% of them lie within $100h^{-1}$ kpc of the center of the final halo; most of the others lie near the center of one of its substructures. If we consider these particles to represent the matter which was already illuminated by star formation at $z = 6$, then the corresponding light is today associated both with the dominant central galaxy in each halo and with other cluster galaxies.

A comparison of the distribution of matter that is illuminated now in the giant galaxy with that which was plausibly already illuminated at $z = 6$ is presented in Figure 4.9. This shows, for the particles used in Figure 4.8, the present cumulative radial distribution about the center of the final halo. In 6 of our 8 halos the largest single concentration of these “early dense” particles is in the central object, with 20% to 50% within $100h^{-1}$ kpc of halo center. In the remaining two objects, however, the dominant concentrations are in subhalos offset by 150 to $500h^{-1}$ kpc from the center of the main halo, so that the bulk of the earliest stars are predicted to be in non-central galaxies.

In these rare massive halos at $z = 6$ the virial radius (at density contrast ~ 200) is comparable to the half-light radius $r_e \sim 10h^{-1}$ kpc of the bright galaxy at the center of the present day descendant. If most of the baryons then within this region had promptly collapsed to stars, the stellar mass fraction within $r = 10h^{-1}$ kpc at $z \sim 6$ would have been about equal to the primeval mass fraction, that is, about one fifth of the total mass within the present half-light radius. The remaining ~ 80 percent of the stars would have been added later, by merging with other concentrations of generally old stars. Roughly in line with this, the indication from Figure 4.3 is that ~ 20 –50% of the mass now interior to $r = 10h^{-1}$ kpc was added at $3 \lesssim z \lesssim 6$, and about half of the mass was added at $z < 3$. We must assume that most of the added mass was stellar, so that the core can be star-dominated today. If the mass displaced out of this radius were primarily CDM, the stellar mass interior to $r_e \sim 10h^{-1}$ kpc would have roughly doubled since $z \sim 3$. Since $M(< r) \propto r^\beta$ with $\beta \sim 1$ in the core, the effective radius r_e of starlight would have about doubled since $z \sim 3$.

4.4.3 The Attractor Hypothesis

Our analysis depends on the hypothesis of a dynamical attractor effect, that *the inner cores of galaxies tend to approach through multiple mergers a universal density profile for their collisionless mixture of stars and dark matter*. The stability of the NFW mass distribution under violent disruptions by mergers argues for this effect, as do observational constraints, as follows.

In the absence of the attractor effect the dissipative settling needed to increase the baryon to dark matter ratio in the luminous parts of a galaxy would tend to make the central mass density run steeper than the NFW/Moore model, leading to two problems. First, it would seem to produce an unacceptably steep central mass density run (Barnes & White 1984; Jesseit, Naab & Burkert 2002; Sand, Treu & Ellis, 2002; Sand et al. 2003, and references therein). Second, it would likely produce too many galaxies with large velocity dispersions.

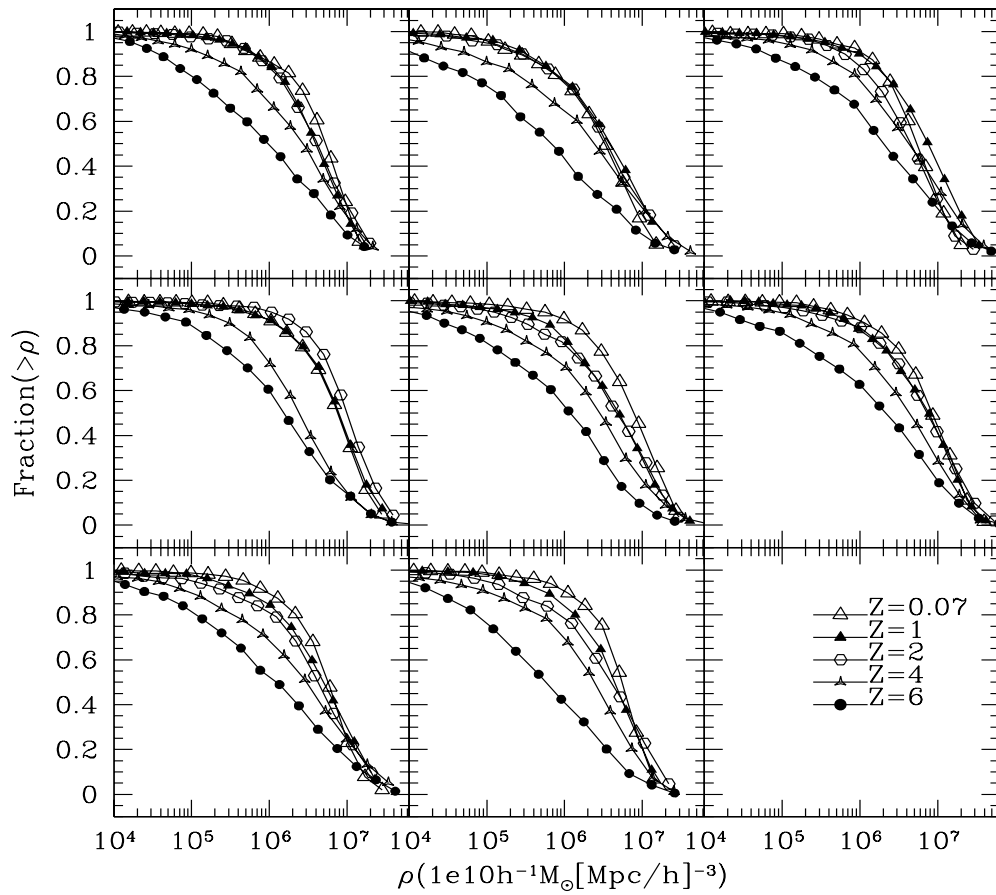


Figure 4.7: Evolution of the cumulative distribution of ambient physical density for particles which lie within $10h^{-1}$ kpc of halo center at $z = 0$. These are the same particle sets used to make Figures 4.4 and 4.6.

4 Earlier formation and later merging of the Giant Galaxies

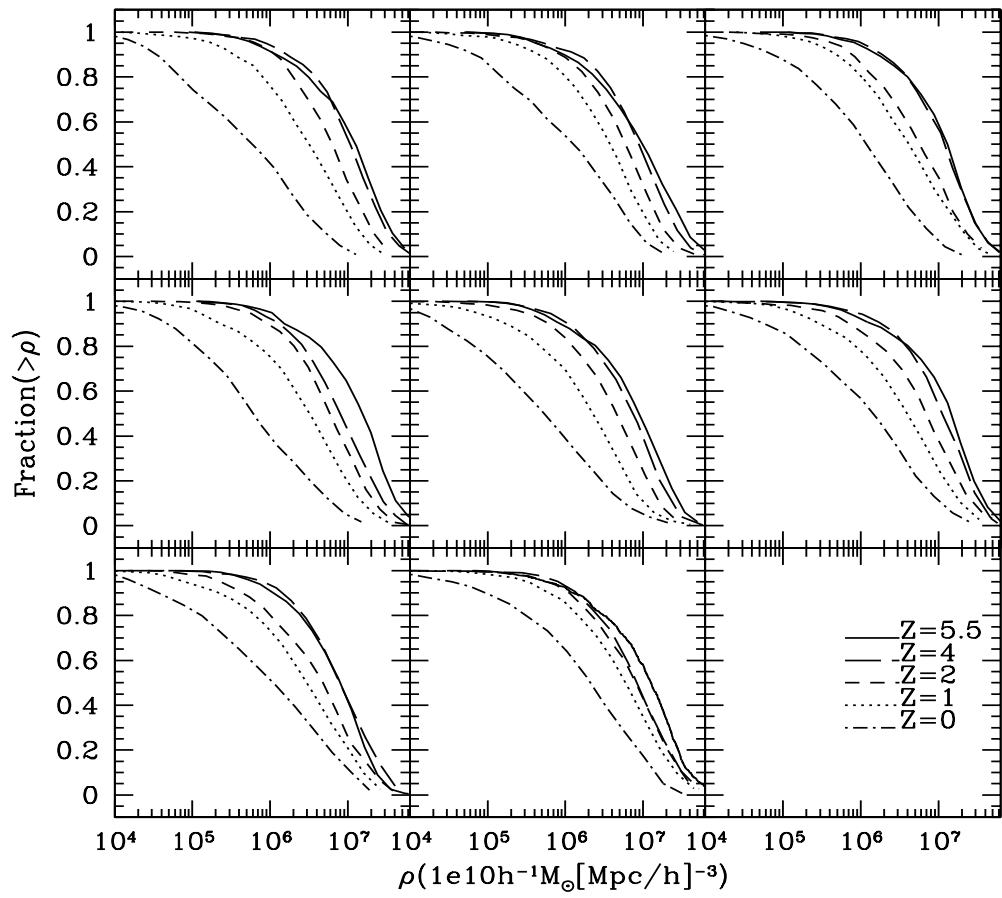


Figure 4.8: Evolution of the cumulative distribution of ambient physical density for those 1000 particles within r_{200} at $z = 0$ which had the highest ambient densities at $z = 6$.

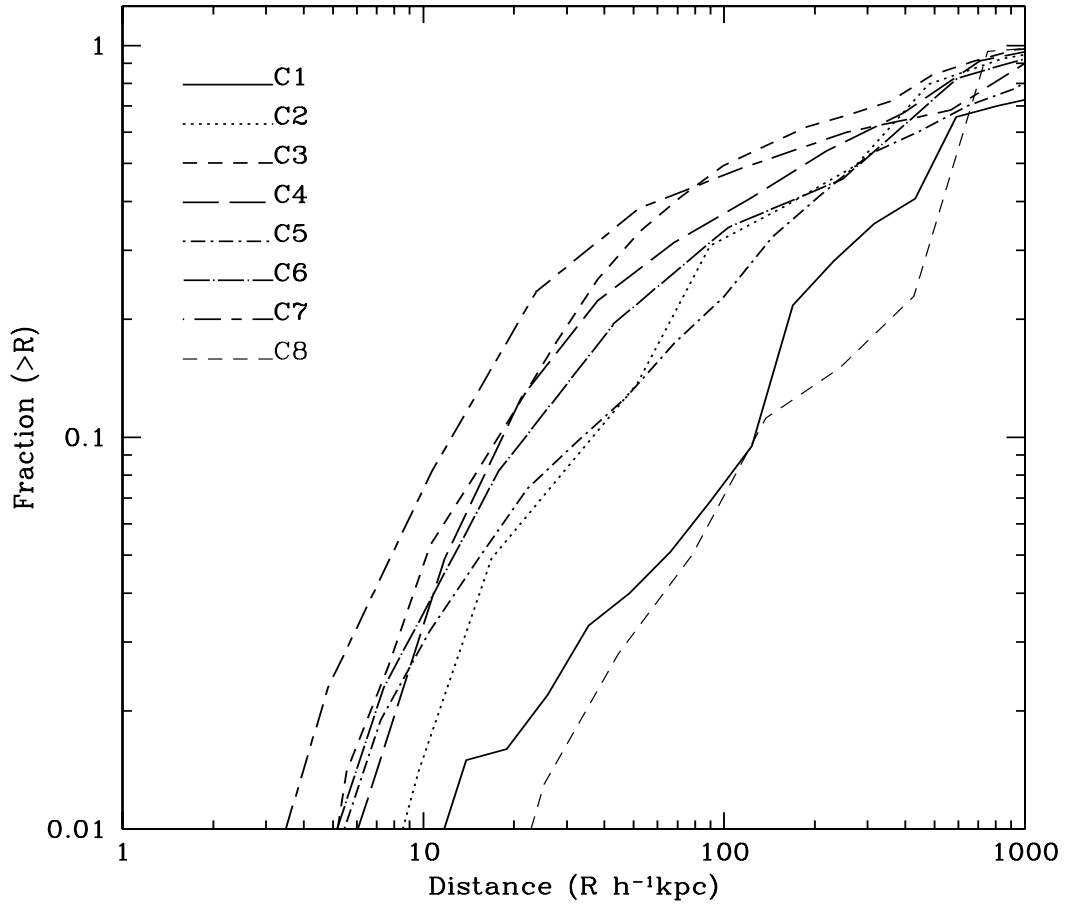


Figure 4.9: The cumulative radial distribution at $z = 0$ of the particle sets tracked in Figure 4.8. The center used here is the density center of the main halo. Note that in several cases a large fraction of the particles are concentrated to one of the halo substructures rather than to this main center.

4 Earlier formation and later merging of the Giant Galaxies

If in the typical giant galaxy all collisionless matter, dark plus stellar, relaxed to a good approximation to NFW, it would certainly help relieve the challenge of the central mass density run. Also, it would allow consistency of the comoving number density of massive halos as a function of the velocity dispersion (at a characteristic present-day half-light radius, $r_e \sim 10h^{-1}$ kpc) with the SDSS observations of the counts of galaxies as a function of the stellar velocity dispersion (as illustrated in Figure 4.2 of Loeb & Peebles 2003, with the data from Sheth et al. 2003). The attractor hypothesis was invoked by Loeb & Peebles (2003) to help resolve these two observational issues.

A similar argument is given in a recent preprint by El-Zant et al (2003). These authors performed simulations of idealised NFW clusters, in which the galaxies are represented by a population of “massive solid clumps”. As the clumps spiral to cluster center, their energy losses causes the central NFW cusp to flatten. This effect also occurs in our own simulations as massive substructure clumps merge into the central region, but in our case the clumps are not solid and are progressively disrupted as they move in. Stellar galaxies can clearly be disrupted in a like manner so it is unclear that the El-Zant et al. representation more realistic than our own. The main point in the current context is that numerical work since the original NFW papers suggests that an NFW-like inner structure is an attractor for evolution from a wide range of initial conditions and thus should apply to stars and dark matter together in rich cluster cores.

In the attractor hypothesis the usual correction for compression by stellar mass added through dissipative settling would apply only to stars formed out of baryons added after the last major merger. Figure 4.3 indicates that the central mass distributions in massive galaxies typically have been rearranged by at least one major merger at $z < 2$. Our hypothesis requires that most of the stars formed earlier than that.

Elliptical galaxies at $z < 1$ do show evidence for recent star formation (Jørgensen 1999; Trager et al. 2000; Menanteau, Abraham, & Ellis 2001; Fukugita 2003), which might be the result of accretion or of recycling of matter shed by stars within the galaxy. The amount of mass added or rearranged by recent star formation is generally thought to be only ~ 10 – 20% , however, and so not likely to greatly disturb the attractor solution.

4.5 Open Issues

The idea that some large elliptical galaxies formed by merging of late-type galaxies has been under discussion for many years (e.g. Toomre & Toomre 1972; Ostriker 1980; Negroponte & White 1983; Schweizer 2000). Under the attractor hypothesis, an elliptical that formed by the merger of gas-rich galaxies with a subsequent starburst, perhaps the typical path in galaxy groups, might be expected to show significant baryon loading effects on its total density run; an elliptical that formed by mergers of less gas-rich early-type galaxies, perhaps the more common pattern for cluster ellipticals, would show fewer effects from baryon loading. We are not aware of observational tests of this possible systematic difference between $\rho(r)$ in field and cluster galaxies, although possibly related differences are seen between the central density runs of bright and faint ellipticals (Faber et al 1997) and between the core colors of cluster and field ellipticals (Menanteau, Abraham & Ellis 2001).

A related issue is the meaning of the strikingly small differences between the spectra and

mass-to-light ratios of cluster and group ellipticals, as illustrated by Hogg et al. (2003) and van Dokkum & Ellis (2003). A detailed analysis of this effect within the Λ CDM model would be challenging, and certainly desirable. A first analysis by Kauffmann & Charlot (1998a) shows qualitative agreement with the data but a quantitative difference between cluster and field which may be larger than observed.

There is a long history of debate over the observational constraints on the time scale for the formation of the mass concentrations characteristic of the luminous parts of present-day giant galaxies (e.g. Peebles 1989; White 1989; and references therein). Radio galaxy surveys provide convincing evidence for the presence of old massive galaxies at redshifts $1 < z < 3$ (Lilly & Longair 1984; Nolan et al. 2003; Willott et al. 2003). Massive high redshift protogalaxies are likely hosts for the $\sim 10^9 M_\odot$ black holes that power the SDSS quasar population at $z \sim 6$ (Fan et al. 2003; Wyithe & Loeb 2003). On the other hand, a number of recent attempts to measure the evolution of the mean stellar density contributed by massive galaxies have concluded that only half the current stars are present at $z \sim 1$ to 1.5 and only a tenth at $z \sim 3$ to 4 (Drory et al. 2003; Bell et al. 2003; Dickinson et al. 2003; Stanford et al. 2003). Estimating the number density and stellar mass of giant galaxies at high redshift poses a severe observational challenge, however, and the current situation is confused. Thus Bell et al. (2003) find that the stellar mass in their red sequence of galaxies has increased by a factor of two since redshift $z = 1$, but Pozzetti et al. (2003) see no significant evolution of the star mass function of massive galaxies over the same redshift interval.

There also is continuing debate over the relation of the observations to the theoretical situation. Kauffmann & Charlot (1998b) find a considerable difference between the redshift distributions predicted for K-selected samples by the assumption of pure luminosity evolution out to high redshift and by a semianalytic Λ CDM model for galaxy formation. They conclude that the observations favor the latter. Somerville et al. (2003) find much smaller differences between their own versions of these two models. The predicted redshift distributions differing insignificantly at $z < 1.4$. At higher redshift their hierarchical model predicts fewer galaxies than their pure luminosity evolution model, with the observations lying between the two. Our own analysis indicates that in the Λ CDM model the stellar mass in a giant galaxy at $z = 3$ could be as much as half the present value. This is considerably less rapid evolution than is claimed by many authors, but is significantly later assembly than pure luminosity evolution assumes. It is perhaps in line with Somerville et al. (2003). We emphasise that the Λ CDM model does produce enough massive objects at early times to account for the highest redshift galaxy clusters, massive galaxies and luminous quasars (Efstathiou & Rees 1992, Mo & White 2002). The debate is whether current treatments of star and black hole formation adequately represent the predictions of the Λ CDM cosmology, and, of course, whether these predictions are compatible with the observed numbers of massive objects at high redshift.

The examples in the numerical simulations used in this paper suggest the typical giant galaxy has suffered significant merging events at redshifts less than unity. The cluster Abell 2199 (Minkowski 1961) has long been considered a likely example of galaxies observed in the act of merging, and the cluster C0337 at $z = 0.59$ may be another case (Nipoti et al. 2003). The number of candidate merging systems of this type is not large, however. It would be of considerable interest to use numerical simulations to develop diagnostics of the

4 Earlier formation and later merging of the Giant Galaxies

appearance of recently merged, massive, early-type galaxies. These could then be used to check the high merger rate of the Λ CDM cosmology.

Our discussion highlights two systematic effects of purely gravitational halo formation. First, the form for the halo density run behaves as a dynamical attractor (Navarro, Frenk & White 1997; Jain & Steinmetz 1999). Second, the mass within a fixed physical radius around the most massive halos evolves little with time after reaching a density contrast on the order of 100 (Fukushige & Makino 2001; Loeb & Peebles 2003). Both effects are supported by numerical simulations, but have not been fully checked in the specific context of baryon settling. Existing simulations of mergers of spirals embedded within NFW-like halos do produce remnants whose inner regions are closer to NFW than those of their progenitors, despite remaining dominated by stars (Barnes 1992; Dubinski 1998). Further simulations would be helpful, however, to check our attractor hypothesis, in particular whether a halo which is compressed relative to NFW by baryon loading relaxes back to NFW after a few major mergers.

Finally, we note that since the physics of pure gravitating systems is simple, even if their behavior is complex, there may be an analytic explanation of the systematics of halo formation discussed in this paper. Possible approaches are discussed by Syer & White (1998) and Dekel, Devor & Hetzroni (2003) among others, but a convincing explanation remains elusive.

Acknowledgements

We have benefitted from discussions with Masataka Fukugita and Jeremy Heyl. This work was supported in part by NASA grant NAG 5-13292, and by NSF grants AST-0071019, AST-0204514 (for A. L.).

References

- Barnes, J. E., 1992, ApJ, 393, 484
- Barnes, J. & White, S. D. M. 1984, MNRAS, 211, 753
- Baugh, C. M., Cole, S., Frenk, C. S., & Lacey, C. G. 1998, ApJ, 498, 504
- Bell, E. F., Wolf, C., Meisenheimer, K., Rix, H., Borch, A., Dye, S., Kleinheinrich, M., & McIntosh, D. H. 2003, ApJ, submitted; astro-ph/0303394
- Bernardi, M., et al. 2003, AJ, 125, 1866B
- Dekel, A., Devor, J. & Hetzroni, G. 2003 MNRAS, 341, 326.
- Conselice, C. J., Bershady, M. A., Dickinson, M. & Papovich, C., AJ, 2003, 126, 1183C
- Dickinson, M., Papovich, C., Ferguson, H. C., & Budavari, T., 2003, ApJ, 587, 25
- Drory, N, Bender, R., Feulner, G., Hopp, U., Maraston, C., Snigula, J., & Hill, G. J., 2003, ApJ, 595, 698
- Dubinski, J. 1998, ApJ, 502, 141
- El-Zant, A. A, Hoffman, Y., Primack, J., Combes, F., Shlosman, I., 2003, astro-ph/0309412
- Efstathiou, G. P. & Rees, M. J. 1988, MNRAS, 230, 5p
- Faber, S. M., Tremaine, S. D., Ajhar, E. A., Byun, Y.-I., Dressler, A., Gebhardt, K., Grillmair, C., Kormendy, J., Lauer, T. R., & Richstone, D. 1997, AJ, 114, 177
- Fan, X. et al. 2003, AJ, 125, 1649
- Frenk, C. S., White, S. D. M, Efstathiou, G. P. , & Davis, M, 1985, Nature, 317, 595
- Fukugita, M. 2003, submitted to ApJ
- Fukushige, T., & Makino, J. 2001, ApJ, 557, 533
- Ghigna, S., Moore, B., Governato, F., Lake, G., Quinn, T., & Stadel, J. 2000, ApJ, 544, 616
- Hamilton, D. 1985, ApJ, 297, 371
- Hogg, D. et al. 2003, ApJL submitted, astro-ph/0307336.

References

- Huss, A. B., Jain, B., & Steinmetz, M., 1999, *ApJ*, 517, 64
- Jenkins, A., Frenk, C. S., White, S. D. M., Colberg, J. M., Cole, S., Evrard, A. E., Couchman, H. M. P., & Yoshida, N. 2001, *MNRAS*, 321, 372
- Jesseit, R., Naab, T., & Burkert, A. 2002, *ApJL*, 571, L89
- Jørgensen, I. 1999, *MNRAS*, 306, 607
- Kauffman, G. & Charlot, S. 1998a, *MNRAS*, 294, 705
- Kauffman, G. & Charlot, S. 1998b, *MNRAS*, 297, L23
- Klypin, A., Kravtsov, A. V., Bullock, J. S., & Primack, J. R. 2001, *ApJ*, 554, 903
- Lilly, S. J. & Longair, M. S. 1984, *MNRAS*, 211, 833
- Loeb, A. & Peebles, P. J. E. 2003, *ApJ*, 589, 29
- Menanteau, F., Abraham, R. G., & Ellis, R. S. 2001, *MNRAS*, 322, 1
- Minkowski, R. 1961, *AJ*, 66, 558
- Moore, B., Ghigna, S., Governato, F., Lake, G., Quinn, T., Stadel, J., & Tozzi, P. 1999, *ApJL*, 524, L19
- Mo, H. J. & White, S. D. M. 2002, *MNRAS*, 336, 112
- Navarro, J. F., Frenk, C. S., & White, S. D. M. 1997, *ApJ*, 490, 493
- Navarro, J. F., Hayashi, E., Power, C., Jenkins, A. R., Frenk, C. S., White, S. D. M., Springel, V., Stadel, J. & Quinn, T. R. 2003, *MNRAS*, submitted (astro-ph/0311231)
- Negroponte, J. & White, S. D. M. 1983, *MNRAS*, 201, 401
- Nipoti, C., Stiavelli, M., Ciotti, L., Treu, T., & Rosati, P. 2003, *MNRAS*, 344, 748
- Nolan, L. A., Dunlop, J. S., Jimenez, R., & Heavens, A. F. 2003, *MNRAS*, 341, 464
- Oke, J. B. 1971, *ApJ*, 170, 193
- Oke, J. B. 1984, *ASSL Vol. 111: Clusters and Groups of Galaxies*, 99
- Ostriker, J. P. 1980, *Comments on Astrophysics*, 8, 177
- Ostriker, J. P. & Tremaine, S. D. 1975, *ApJ*, 202, L113
- Peebles, P. J. E. 1989, in *The Epoch of Galaxy Formation*, eds. C. S. Frenk et al. NATO ASI series, vol 264, p. 1
- Peebles, P. J. E. 2002, *ASP Conf. Ser. 283: A New Era in Cosmology*, 351
- Pozzetti, L. et al. 2003, *A&A*, 402, 837

-
- Romanowsky, A. J., Douglas, N. G., Arnaboldi, M., Kuijken, K., Merrifield, M. R., Napolitano, N. R., Capaccioli, M., & Freeman, K. C. 2003, *Science*, 301, 1696
- Sand, D. J., Treu, T., & Ellis, R. S. 2002, *ApJL*, 574, L129
- Sand, D. J., Treu, T., Smith, G., & Ellis, R. S. 2003, *ApJ*, submitted; astro-ph/0309465
- Schweizer, F. 2000, *Phil Trans R Soc London, A* 358, 2063
- Sheth, R. K., Mo, H. J., & Tormen, G. 2001, *MNRAS*, 323, 1, 119
- Sheth, R. K. & Tormen, G. 1999, *MNRAS*, 308
- Sheth, R. K. et al. 2003, *ApJ*, in press; astro-ph/0303092
- Somerville, R. S. et al., 2003, *ApJL*, in press; astro-ph/0309067
- Springel, V., Yoshida, N., & White S. D. M., 2001, *New Ast.* 6, 79
- Stanford, S. A., Dickinson, M., Postman, M., Ferguson, H., Lucas, R., Conselice, C., Budavari, T., & Somerville R., 2003, *ApJ*, in press; astro-ph/0310231
- Syer, D. & White, S. D. M. 1998, *MNRAS*, 293, 337
- Toomre, A. & Toomre, J. 1972, *ApJ*, 178, 623
- Trager, S. C., Faber, S. M., Worthey, G., & González, J. J. 2000, *AJ*, 119, 1645
- van Dokkum, P. G. & Ellis, R. S. 2003, *ApJL*, 592, L53
- White, S. D. M., 1980, *MNRAS*, 191, 1
- White, S. D. M. 1989, in *The Epoch of Galaxy Formation*, eds. C. S. Frenk et al. NATO ASI series, vol 264, p. 15
- Willott, C. J., Rawlings, S., Jarvis, M. J., & Blundell, K. M. 2003, *MNRAS*, 339, 173
- Wyithe, J. S. B. & Loeb, A. 2003, *ApJ*, 595, 614
- Yoshida N., Sheth R. K. & Diaferio A., 2001, *MNRAS*, 328, 669

References

5 The first structures in a CDM Universe

Abstract

We have carried out a sequence of N -body resimulations of individual haloes at various redshifts within a *cosmological volume* $(0.68\text{Gpc})^3$ with the aim of resolving the first bound objects which could potentially host the first stars in a cold dark matter dominated universe. Our simulations succeed in resolving rare but relatively massive haloes spanning a very broad redshift range [$z = 80, z = 0$] with ultra-high resolution. The highest resolution achieved in our final level simulation has a particle mass of $0.8M_\odot$ and a force softening of $\epsilon = 7.8\text{pc}$ in comoving units. Our results indicate that initial structure formation was extremely strongly biased to overdense regions, and that this can be well understood within the framework of extended Press-Schechter(EPS) theory. The internal structure of these early haloes are quite similar to their low redshift counterparts, although the NFW profile does not fit as well. The halo mass function is examined at redshift $z = 50$ and $z = 30$. We find an excellent agreement between the predictions and the simulations. Because our simulation volume is not a small periodic box we are able to simulate rarer and more massive halos at any given redshift than previous work. We find that bound-free cooling from atomic hydrogen can take place in haloes as early as $z = 32$ and that the comoving abundance of these halos is predicted to be the same as for $10^{14}h^{-1}M_\odot$ halos today. If the first stars did form in haloes with mass $\sim 10^6M_\odot$, a large number would be born already at $z \sim 42$ with a comoving abundance matching that of haloes with mass M_* today.

5.1 Introduction

Soon after their birth the first stars will light up the universe and begin to influence the thermal and chemical state of the ambient gas. The precise details of what happens when these stars turn on has yet to be understood. Recent simulation work following the evolution of dark matter and primordial gas (see Bromm & Larson, 2003 and reference therein) has claimed that the first stars are born in haloes with virial temperatures $T_{\text{vir}} \sim 2000\text{K}$ and masses $M \sim 10^6M_\odot$ at redshifts $20 < z < 30$ (Abel et al. 1999; Fuller & Couchman, Bromm et al. 2001; Yoshida et al. 2003).

Because of constraints from currently available computer resources, previous hydrodynamical simulation work on the first stars has been carried out by following gas and dark matter in small comoving periodic cubes (Abel et al. 1999; Yoshida et al. 2003). According to the CDM scenario, at high redshift, the most massive haloes, which may house the first generation of stars, are extremely rare objects and are expected to originate from extreme rare high density peaks. Small periodic boxes tend to suppress the height of the peaks (Bond et al. 1991; Barkana & Loeb 2003) as well as to limit the volume surveyed, and therefore will artificially underestimate the formation redshift of the first stars. Thus the first stars resolved in these previous simulations form later than the *real* first stars

which would appear in a CDM universe. An alternative approach, is to simulate a high σ region with constrained initial conditions (Fuller & Couchman 2000; Bromm et al. 2001). However, there is no clear relation between the statistical properties of the final objects starting from such constrained initial conditions and those objects forming from realistic initial conditions (White 1993). Thus the question of when and how the first stars appear in our universe should be revisited.

Starting with the framework of the extended Press-Schechter theory (Bond et al. 1991; Lacey & Cole 1993, 1994; Mo & White 1996, 2002; Sheth & Tormen 2002), it is possible together with semi-analytical modeling to constrain the formation of the first stars. In recent years, EPS and improved EPS (e.g. Sheth & Tormen (1991), Jenkins et al. (2001)) theory have been compared against N-body simulations over a very broad parameter range (Jenkins et al. 2001; Reed et al. 2003; Gao et al. 2004a). These comparisons show excellent agreement between the halo abundance in N -body simulations and the analytical formulae by Jenkins et al (2001) and by Sheth & Tormen (1999). However these comparisons are still limited by the finite dynamical range of current simulations. The validity of EPS theory has only been checked over a limited mass and redshift range. Previous results already show that EPS or Sheth & Tormen mass function do not correctly predict halo abundance at the high mass end (Jenkins et al. 2001). In the CDM model, the earliest structures we are interested in are all extremely rare objects so one needs to be particularly cautious when using EPS theory in this regime before it is confirmed.

In this paper, we carry out a sequence of ultra-high resimulations of individual objects at a variety of redshifts with the aim of simulating convincingly the formation of the earliest structure in a CDM universe. To start with, to familiarise the reader with the properties of the dark matter distribution at high redshift we present a series of images of the halos and their surroundings. We then examine whether or not the analytical theory which works well at low redshift can be applied at high redshift. We defer the inclusion of hydrodynamical modeling of the condensation of primordial gas to future papers. The paper is structured as follows. In Section 2, we describe our simulation method in detail. In Section 3, we investigate biased clustering of massive haloes at high redshift, and examine the performance of EPS theory against our simulations. In Section 4, we study the internal structure of massive dark objects as a function of redshift. We discuss the implications of our simulation in Section 5. Finally, we set out our conclusions in Section 6.

5.2 Simulations details

We used the following cosmological parameters for our simulations: $\Omega = 0.3$, $\Lambda = 0.7$, $\sigma_8 = 0.9$, $\Omega_b h^2 = 0.0196$ and $h = 0.7$. The initial linear power spectrum is computed down to scale $2000h/\text{Mpc}$ with CMBFAST (Seljak & Zaldarriaga, 1996). It was necessary to extrapolate a further order of magnitude in wavenumber to reach the Nyquist frequency defined by our highest resolution resimulation. The extrapolation used was a power-law matched to the slope at the join. Strictly speaking one would expect there to be some curvature but in fact at these wavenumbers the slope is very close to -3.

5.2.1 The simulations

It is a challenge to simulate the formation of the first structures, because in a CDM universe, structure formation is hierarchical and the first collapsed objects are very small. More seriously the slope of the matter power spectrum on small scales approaches the critical value of -3 where the contribution to the variance of the density field per log interval in wavenumber is independent of wavenumber. Thus a wide-range of scales make important contributions to the density field fluctuations (Efstathiou et al. 1988; Smith et al. 2003). A very large simulation box is required to provide the correct long wave fluctuations and with current computer resources it is not possible to simulate a sufficiently large region while at the same time following the non-linear dynamics of the first collapsing structures.

We have devised a procedure to circumvent this dilemma as follows.

- (1) We identified a rich cluster in a very large volume cosmological simulation.
- (2) we then resimulated this rich cluster and its immediate surroundings with higher mass and force resolution. The final cluster had around 2 million particles.
- (3) We identified the most massive object in the high resolution region at a higher redshift when it contained only around 10000 particles within the virial radius.
- (4) We then resimulated this object and its immediate surroundings with higher mass and force resolution (again with several million particles inside virial radius).
- (5) repeat 3 and 4 again and again until the desired redshift or particle mass is achieved.

In practice, we selected a rich cluster of virial mass $8 \times 10^{14} h^{-1} M_{\odot}$ from a large scale cosmological simulation (The VLG simulation of The Virgo consortium, Jenkins et al. 2001) with side-length $479 h^{-1} \text{Mpc}$. The first resimulation of the cluster (named cl01) has been analyzed in Navarro et al.(2003) and Gao et al. (2003, 2004a, 2004b). Then we used the ‘‘Zoom-in’’ resimulation technology similar to Power et al. (2003) to simulate the desired object step by step following the recipes described above with much higher mass and force resolution. At the end of each new simulation, we checked the virial mass and the surrounding structure between the lower and the higher resolution simulations to ensure they are consistent. For the first three resimulations, R1 ($z = 0$), R2 ($z = 5$) and R3($z = 12$) the simulation was run with the original periodic boundaries of the parent simulation. We used isolated boundary conditions with a spherical cut-off at comoving radius $5 h^{-1} \text{Mpc}$ and $1.25 h^{-1} \text{Mpc}$ for R4 and R5 respectively. Since the universe is quite homogenous at high redshifts on these scales, our desired objects were largely unaffected by the omission of more distant structures. Note that this cut-off, unlike the imposition of periodic boundary conditions, does not cut-off the contribution to the density field due to long wavelength modes, although it does significantly affect the bulk motion of the region, which we are not interested in here. The high resolution regions for R1, R2 and R3 simulation are about 4 times the virial radius of the final object, while for R4 and R5 we employed a more extensive volume to allow us to investigate the large scale structure around the largest halos. Further details of our series of resimulations are listed in Table 1. Here N_p is the total number of particles in the high resolution region of each simulation,

Table 5.1: Numerical parameters of R series simulation

	<i>R1</i>	<i>R2</i>	<i>R3</i>	<i>R4</i>	<i>R5</i>
N_p	8457516	5804755	8658025	41226712	73744737
$m_p[h^{-1}M_\odot]$	5.12×10^8	2.2×10^6	1.24×10^4	29.5	0.545
$\epsilon[h^{-1}\text{kpc}]$	5.0	0.8	0.15	0.017	0.0048
$M_{200}[h^{-1}M_\odot]$	0.8×10^{15}	3.4×10^{12}	2.0×10^{10} ,	5.2×10^7	1.2×10^5
z_{start}	39	149	249	399	599
z_{final}	0.0	5.0	12.04	29.04	48.84

M_p is the mass of each of these particles, ϵ is the softening parameter (in comoving units), M_{200} is the mass of the final object within a sphere of mean overdensity 200 relative to critical, and z_{start} and z_{final} are the initial and final redshift of the simulation.

Typically in our resimulations the highest mass halo is resolved with 2 million particles inside r_{200} . Only for the highest redshift $z = 48.84$, was the particle number significantly lower at 0.2 million particles. For R5, the highest resolution resimulation, the particle mass was $0.8M_\odot$ and the force softening of 7.8pc in comoving units.

For a given halo mass at a particular redshift one can associate a characteristic abundance, defined as the number of halos of equal or greater mass per unit volume. While the iterative procedure outlined above is guaranteed to find a rare massive halo at high redshift it is not obvious what the global mean abundance of the halos generated by this procedure actually is. The abundance cannot be on average any lower than the abundance of galaxy clusters similar to that selected initially. In fact, it turn out to be significantly higher.

The R1 simulation was run with the publically available tree code GADGET-1.1(Springel, Yoshida & White, 2000). The other simulations were run with an improved TREE-PM GADGET-2.0 (Springel 2004, in preparation).

5.2.2 Halo finders

In N -body simulations two of the most common methods to identify halos are: the friends-of-friends algorithm of Davis et al. (1985), and the spherical overdensity(SO) finder described by Lacey & Cole (1994). An advantage of the FOF method is that it does not impose any fixed shape on the halos, and it is very economical computationally. However, it occasionally links two separate haloes through a chance bridge of particles. In the limit of very large numbers of particles per object, FOF approximately selects the matter enclosed by a fixed isodensity contour.

In the SO algorithm, the mass of a halos is evaluated in a spherical region. There is only one free parameter, the mean overdensity, k , of the halos, although there are many possible ways of centering the spherical region. In our implementation, the centre is determined iteratively, after making an initial guess based an estimate of the local density for each particle with the standard SPH method, re-centering on the center-of-mass, growing a sphere outwards about the new centre until it reaches the desired mean overdensity, and recomputing the center-of-mass. After several iterations, the motion of the centre becomes

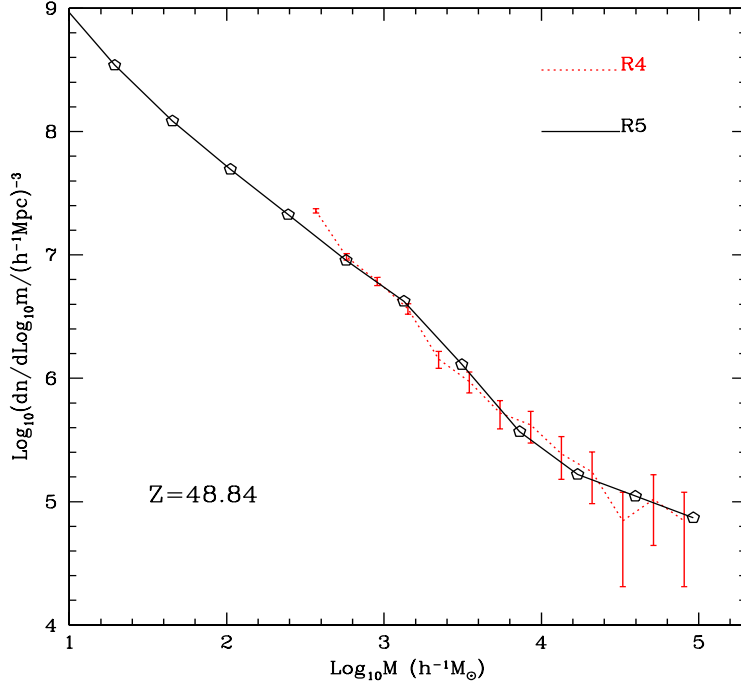


Figure 5.1: Halo mass function for the same region of R4 and R5 simulation. The haloes are identified with SO(180) algorithm; The error bars assume Poisson uncertainties in the counts for the R4 haloes.

small. The advantage of the SO algorithm is that it avoids the problem of occasionally linking two disjoint halos. It does, however, impose a fixed spherical shape on the haloes.

For the first structures, as we will see in later sections, massive objects are very strongly clustered, and their separations are usually small. More over, these objects are almost always connected together by long filaments made of smaller haloes. We find that the FOF halo selection is then quite dependant on the mass resolution of the simulations. For example, with the FOF(0.2) algorithm, the halo mass function in the corresponding region of R4 and R5 simulations are very different, 15 per cent of all high resolution particles are identified as a single halo for the R5 simulation, which it doesn't occur for the lower resolution simulation R4. The abundance of haloes selected by SO($k = 180$) is the same for lower and higher resolution as can be clearly seen in Fig. 5.1, where we plot it for the R4 and the R5 simulations; clearly, they match up to the resolution limit of the lower resolution simulation. In what follows, we use the SO(180) algorithm to identify all halos, unless otherwise stated.

5.3 Large scale structure at high redshift

5.3.1 Morphology

According to the CDM paradigm, growing density fluctuations imprinted in the very early universe begin to evolve into the nonlinear regime on small scales first with larger and larger scales participating as time progresses. At high redshift the matter power spectrum has a slope close to -3 and this means that structure grows in scale more rapidly (measured in terms of the Hubble time) than in the present day universe. Because of this difference it is interesting to compare “large scale” structure at high redshift to that today. For this comparison, we scale length units to r_{200} of the most massive halo in our R4 simulation at $z = 48.84$ and to the R1 halo at $z = 0$ in the VLG simulation. Here r_{200} is defined to be the radius within which the mean enclosed density is 200 times the critical value. In comoving units, it is 1.5Mpc for the R1 halo, and 1.2kpc for the R5 halo which is the most massive halo in high resolution region of R4 simulation at redshift $z = 48.84$.

In Fig. 5.2, the mass surface density of “large scale” structure for our R4 simulation at $z = 48.84$ is shown in the bottom panel, and for the parent VLG simulation at $z = 0$ is shown in the upper panel. In this plot, a slice of geometry $190 \times 190 \times 10$ in units of r_{200} is projected into a plane. We normalize the projected density fields using the projected cosmic mean surface density at the corresponding redshifts. The color table in each panel represents the real dimensionless surface density $1 + \delta$, and is shown with a logarithmic scale. The mass distribution of the VLG simulation on large scales is relatively homogenous while the structures at early times are very strongly biased around the most massive halo of our simulation. This is consistent with the statistics of *gaussian random* fields (Kaiser et al. 1984): high density peaks tend to be more strongly clustered. This indeed indicates that the most massive halos at high redshift reside in very large overdense regions imprinted on the initial density field.

5.3.2 Biased structure formation at high redshift

We quantify this biased spatial clustering of structure at high redshift visible in Fig. 5.2 by comparing the mass function measured directly from our simulations with that predicted as the cosmic mean. Note that no studies have established whether the current analytical formulae works well at such high redshift and on such small mass scales. In the bottom panel of Fig. 5.3, we plot the SO(180) halo mass function for spherical regions centered the most massive halo in the high resolution region of the R4 simulation at redshift $z = 48.84$. We give results for radii 80, 40 and 20 times r_{200} of this halo. For comparison, we plot the halo abundance for spherical regions centred on our $z = 0$ cluster with radii 80, 40 and 20 times its r_{200} . In each panel of Fig. 5.3, we also plot the standard Press-Schechter (PS) (Press & Schechter 1973) and Sheth & Tormen (Hereafter ST) (Sheth & Tormen 1999) mass function as short-dashed and long-dashed lines. It is noticeable that the difference between the PS and the ST mass function at $z = 48.84$ is a factor of 8, much larger than at $z = 0$. Clearly, the halo abundance in the VLG simulation agrees with ST at $z = 0$ over the entire mass range both for $r < 80r_{200}$ and for $r < 40r_{200}$, whereas it is slightly higher at the large mass end for $r < 20r_{200}$. There is no significant bias in abundance in large volumes around a massive halo at $z = 0$ and the mean overdensity for these selected

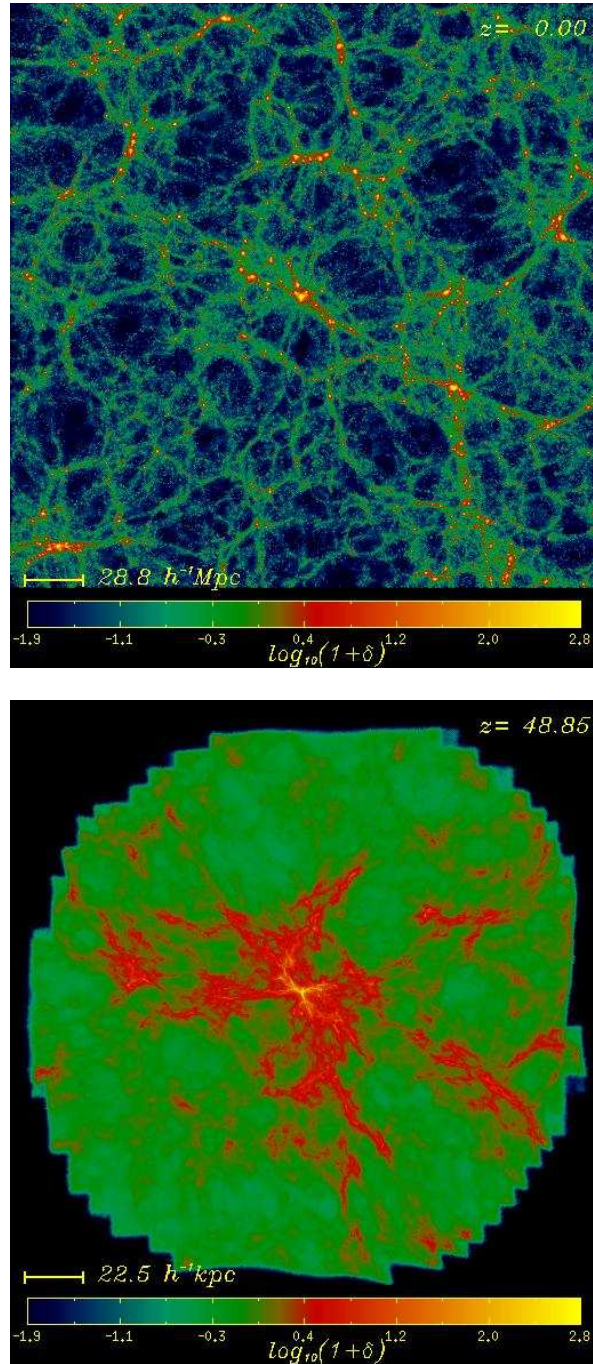


Figure 5.2: Projected dark matter density fields of a slice of geometry $190 \times 190 \times 10$ in units of r_{200} of the halo on which each slice is centred. This is the R5 halo (the most massive halo in high resolution region of the R4 simulation at $z = 48.84$) and the R1 halo at $z = 0$. The VLG simulation is plotted in the upper panel and the R4 simulation in the lower panel. The density fields are normalized to the cosmic mean density field and shown in a logarithmic scale.

5 The first structures in a CDM Universe

regions is almost 0. On the other hand, the halo abundance at redshift $z = 48.45$ in our largest examined volume ($r < 80r_{200}$) is about 1200 and 150 times more abundant than the predicted by the EPS and the ST respectively over the whole mass range we resolve. This is in large part due to the fact that this whole region is overdense, as seen in Fig. 5.2.

It is important to know whether the analytical formulae can correctly reproduce the halo abundance found in numerical simulations at such a high redshift. There is no straightforward approach to test this with our data, since our simulated regions are special ones with high overdensity. However, we can compare our results with conditional EPS theory.

Extending PS theory, Bond et al. (1991) argued that the fraction of the mass in a initial region of radius R_0 and linear overdensity δ_0 which at redshift z_1 is contained in dark haloes of mass M_1 is given by,

$$f(S_1, \delta_1 | S_0, \delta_0) \frac{dS_1^2}{dM_1} dM_1 = \left(\frac{1}{2\pi}\right)^{1/2} \frac{\delta_1 - \delta_0}{(S_1^2 - S_0^2)^{3/2}} \exp\left[-\frac{\delta_1 - \delta_0}{2(S_1^2 - S_0^2)}\right] \frac{dS_1^2}{dM_1} dM_1 \quad (5.1)$$

where, S denote the top-hat variance of linear density fluctuation, S_1 is for redshift z_1 and S_0 is for initial redshift z_0 ; δ_1 is the linear overdensity. Now we need to connect the nonlinear overdensity in *Eulerian space* to the original linear overdensity in *Lagrangian space*. Based upon the spherical collapse model, Mo & White(1996) first derived an analytical formula linking the nonlinear overdensity to the linear overdensity in *Lagrangian space* for an *Einstein-de sitter* universe, and afterwards Sheth & Tormen confirmed that it is reasonably accurate for all cosmologies (Sheth & Tormen, 2002).

$$\delta_0(\delta, z_0) = \frac{\delta_{sc}(z_0)}{1.68647} \times \left[1.68647 - \frac{1.35}{(1 + \delta)^{2/3}} - \frac{1.12431}{(1 + \delta)^{1/2}} + \frac{0.78785}{(1 + \delta)^{0.58661}} \right] \quad (5.2)$$

It is simple to measure the nonlinear overdensity in each spherical region of the R4 simulation, we derive a the nonlinear overdensity $\delta = 1.7$ for the spherical region with radius $80r_{200}$, $\delta = 2.8$ for $40r_{200}$ and $\delta = 4.3$ for $20r_{200}$, respectively. Then we use Equation 5.2 to compute the corresponding linear overdensity which is needed in Equation. 5.1 to derive the predicted halo abundance in these regions. In the same plot, the thick solid lines are the halo abundance functions predicted by conditional EPS theory corresponding the halo abundance in the three different region. Clearly, the agreement is very good in all cases. This indicates that the EPS mass function is surprisingly accurate for estimation of halo abundance in high density regions at high redshifts.

5.4 Evolution of massive halo structure and environment

We now turn to on investigation of the internal structure and immediate surroundings of massive haloes as a function of redshift.

5.4 Evolution of massive halo structure and environment

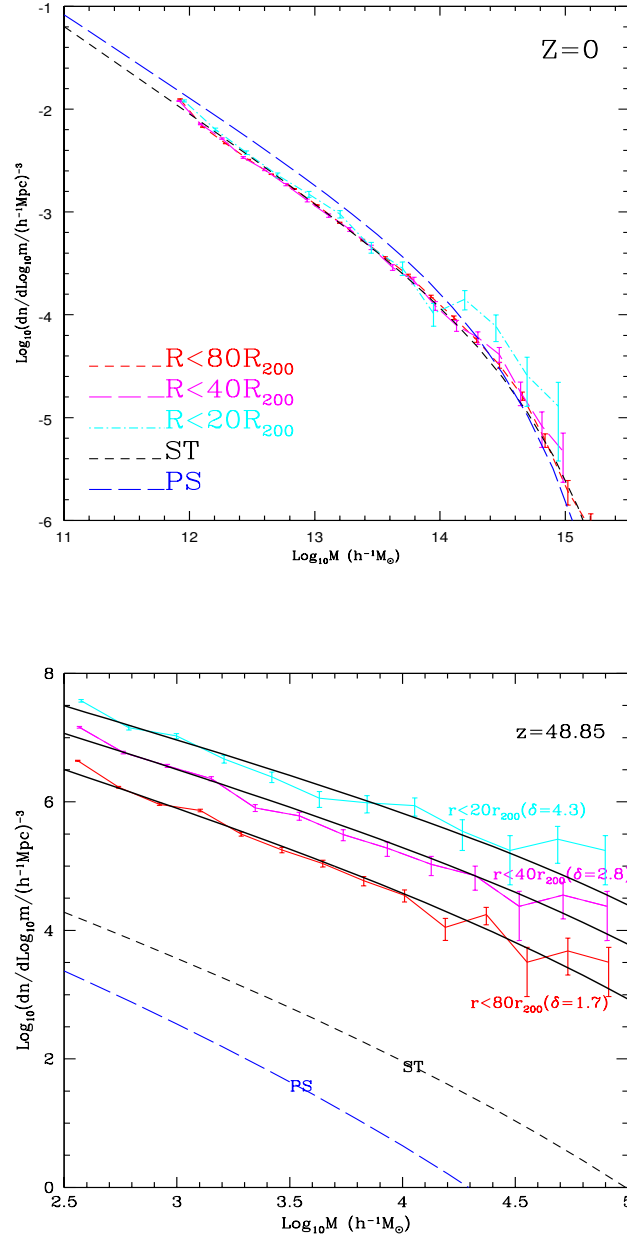


Figure 5.3: Halo abundance function in the VLG (top panel) and the R4 simulation (bottom panel) for different spherical regions $80R_{200}$, $40R_{200}$ and $20R_{200}$ centred on the R1 halo at $z = 0$ and on the most massive halo in the high resolution region of the R4 simulation at $z = 48.85$, respectively. Halos were identified by the standard SO(180) method. The error bars assume Poisson uncertainties in the counts. In the bottom panel, the solid lines in the upper curve are the predicted halo abundance in regions with different nonlinear overdensity according to constrained Press–Schechter theory.

5.4.1 Visualization

In the left column of Fig. 5.4, we show images of our massive haloes as a function of redshift. In each plots, the density field in a cube with length 4 in units of r_{200} centered on the final halo in one of our resimulations is projected into a plane. Again, the surface density is normalized to the cosmic mean. Clearly, these haloes look rather similar in that they are all quite centrally concentrated. However there is a strong trend for the strength of the surrounding filaments to increase with redshift.

In the right column of Fig. 5.4, we show the same haloes on a larger scale. In the plots, we project a slice of thickness of $2r_{200}$ and side $10r_{200}$ for the same haloes. As can be seen, the density contrast in the images is higher for haloes at $z = 0$ and $z = 5$, this suggests that the matter in the region we show is very concentrated to the central dark haloes; while the background is brighter for haloes at $z = 12$, $z = 29$ and $z = 48$ where very strong filaments are visible.

5.4.2 Density profile of dark haloes as a function a redshift

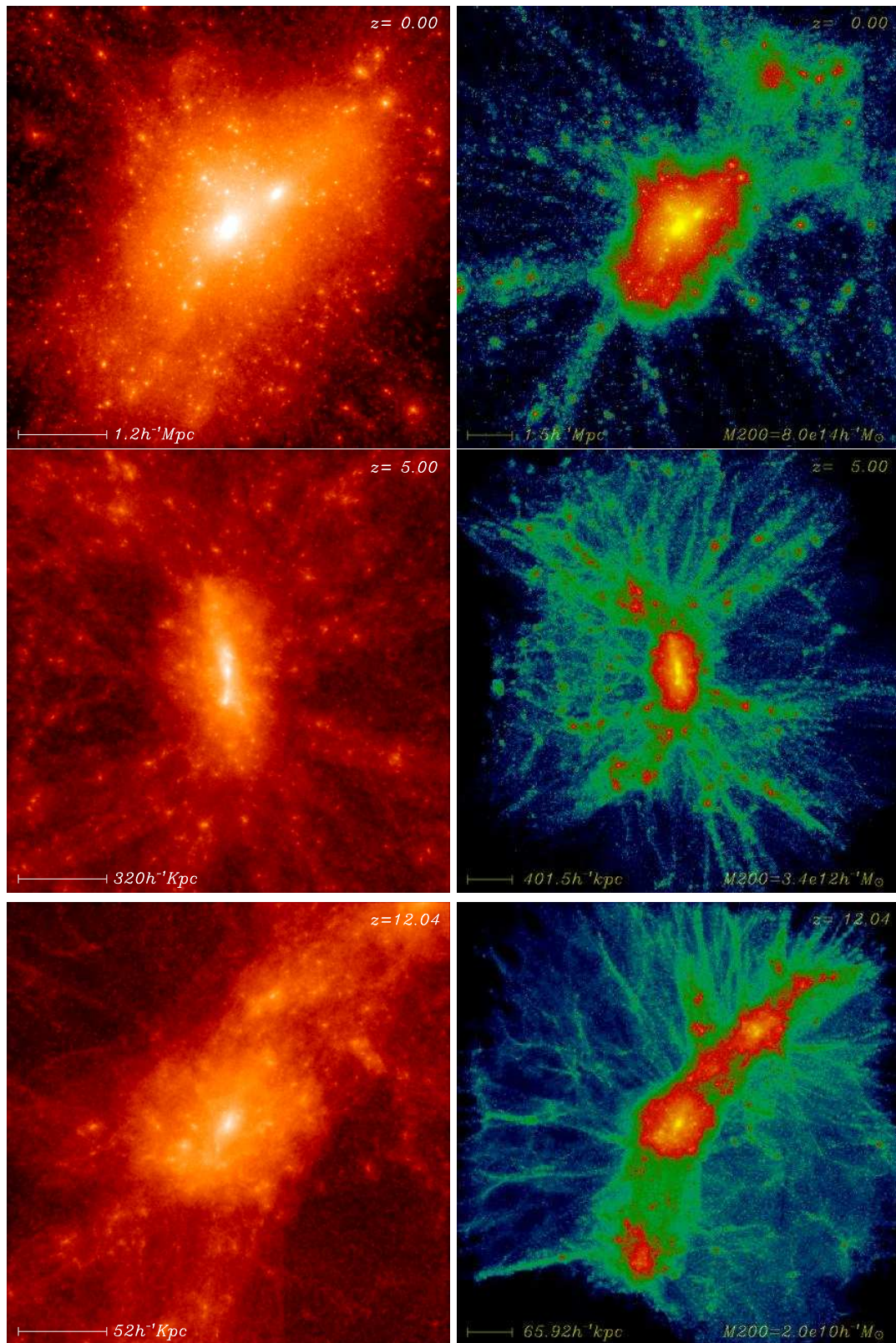
In collisionless dark matter only simulations, the density profiles of low redshift CDM haloes are well described by a simple fitting function with two parameters, ρ_s and r_s (Navarro, Frenk & White, 1997). Here r_s is a characteristic radius where the logarithmic density profile slope is -2, and ρ_s is the mass density at r_s . Recent high resolution simulations confirm that the NFW profile actually is a good fit to 1% of the virial radius, although there is still debate about the asymptotic slope at smaller radii (Navarro et al. 2003; Reed et al. 2003; Diemand et al. 2004). Roughly two million particles lie within virial radius of the final halo in all our simulations except R5 so we can look at the internal structure of massive haloes as a function of redshift. In Fig. 5.5 we show the density profiles of these final massive haloes as open symbols. The best NFW fit for these haloes are shown as the solid lines, and the concentration parameter $c = r_{200}/r_s$ is given in each panel. As can be seen, the NFW profile is a good description of these objects up to redshift $z = 12$, but it does not work so well for earlier times.

In the lower left panel, we overplot all these density profiles for a convenient comparison. This shows that, when scaled with r_{200} , the density profile for the final massive haloes in our sequence are systematically dependent on redshift: the inner slope and the concentration parameter c decrease with increasing redshift. It is noticeable that the density profiles for the R4 and the R5 haloes are almost the same, and their surrounding structures are quite similar (see in Fig. 5.4). This suggests the possibility of a self-similar formation of very massive dark haloes at high redshift.

5.4.3 Properties of Substructure

The high resolution achieved by numerical simulations in recent years has allowed detailed study of the properties of dark matter substructure (subhaloes) within dark haloes (Ghigna et al. 1998; De Lucia et al. 2004; Diemand et al. 2004; Gao et al. 2004a, 2004b). The properties of substructure are important to characterize the internal structure of dark matter haloes and to compare to observed substructure such as satellite galaxies. Unfortunately,

5.4 Evolution of massive halo structure and environment



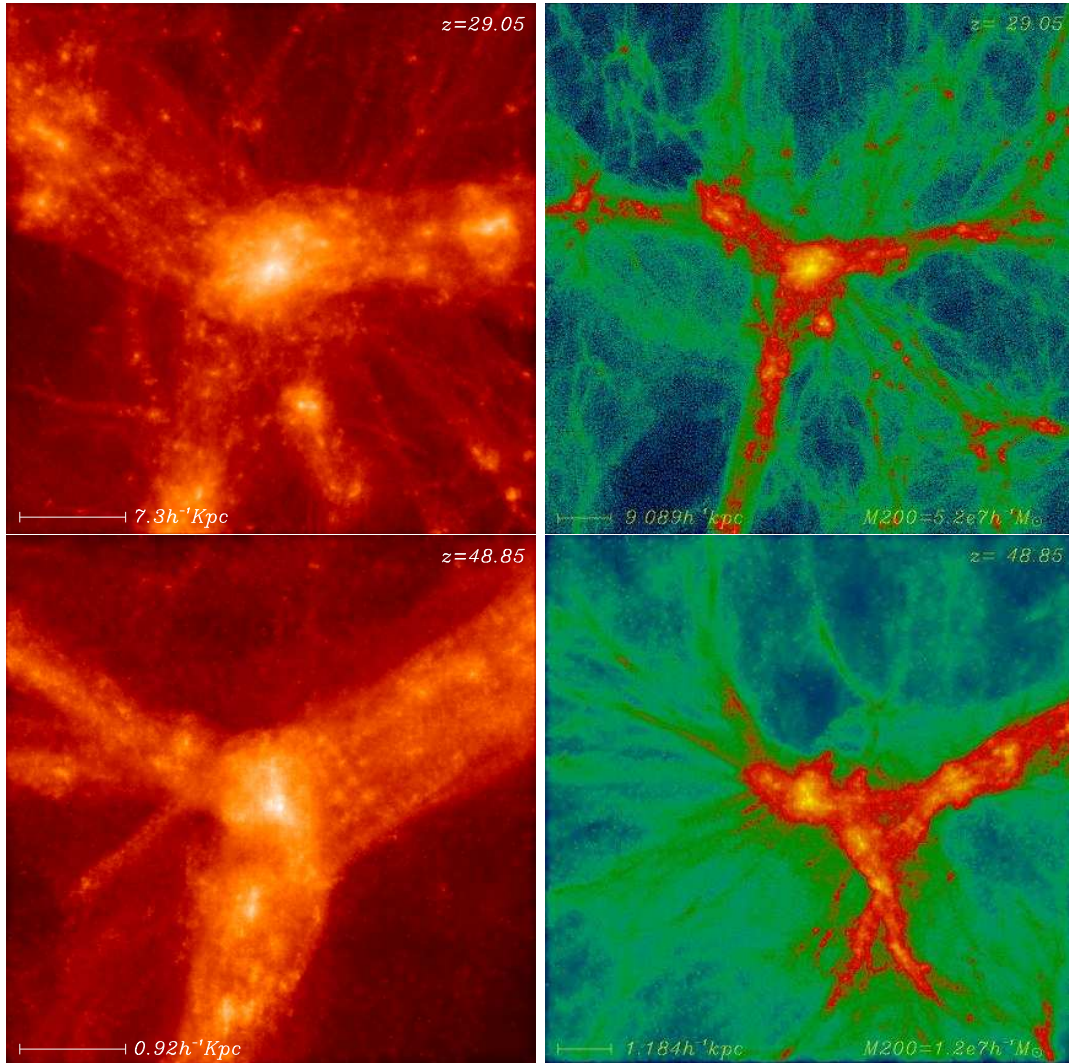


Figure 5.4: Projected dark matter density fields of massive halo in inverse chronological order. In left-hand panel we plot mass projections of dark matter particles within a cube with $4r_{200}$ on a side. In right panel we show a slice centra to our final haloes in our sequence simulations with geometry $10 \times 10 \times 2$ in unit of r_{200} of the corresponding haloes. The density fields are normalized with mean cosmic density field and shown using a logarithmic scale.

5.4 Evolution of massive halo structure and environment

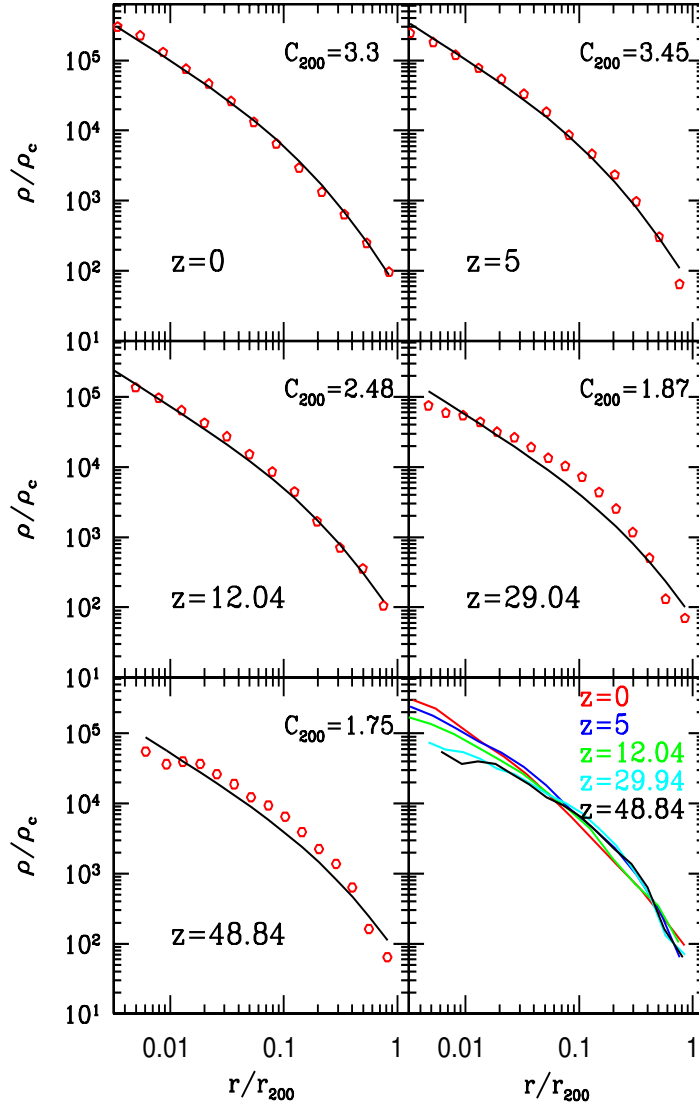


Figure 5.5: Density profiles for the final halo in each of our simulations. The open circles are the density profile measured directly from the simulations, the solid lines are the corresponding fits with the NFW profile. c_{200} , given in each panel, is the corresponding concentration parameter.

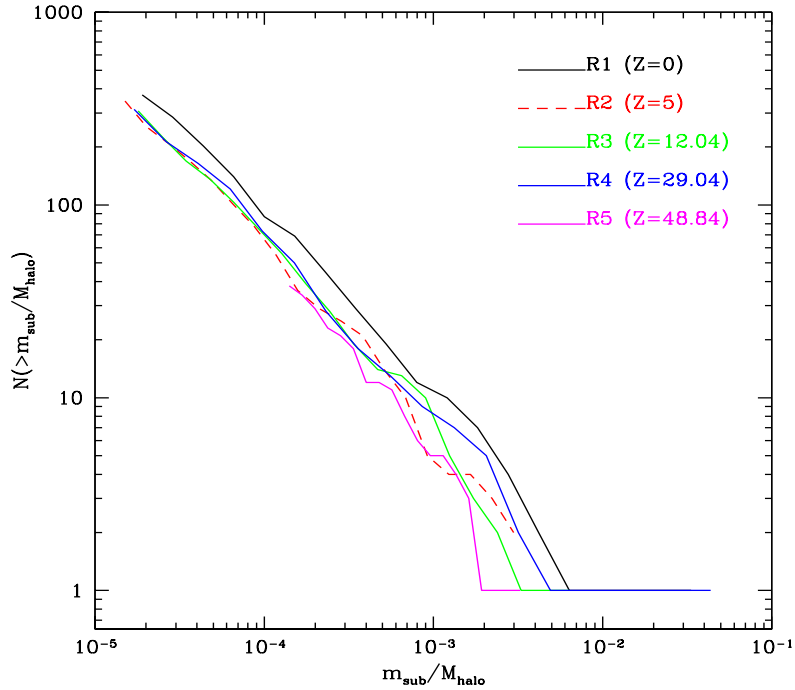


Figure 5.6: Cumulative subhalo abundance functions for the final haloes of our sequence of simulations

the correspondence between subhaloes and galaxies is a complicated one (Springel et al. 2001; Gao et al. 2004b).

In Fig. 5.6, we plot the cumulative subhalo abundance function for the final haloes in our sequence of simulations. Note that we scale subhalo mass by m_{200} of the host halo and only subhaloes within r_{200} are counted. It is remarkable that the substructure abundance is quite similar for haloes at all redshifts except $z = 0$, when subhaloes are roughly a factor of 1.5 more abundant than at earlier times. This similarity may again reflect the self-similar formation of these very massive haloes.

The radial distribution of substructures is also similar to that in low redshift counterparts. Subhaloes are significantly less centrally concentrated than the underlying mass distribution, as shown in Fig. 5.7. In this plot, all subhaloes containing at least 30 particles are counted, this is the limit to which Gao et al. (2004) considered the subhalo distribution to be insensitive to resolution effects.

5.5 Discussion

If the evolution of the primordial gas and dark matter in current hydrodynamic simulations has been followed correctly, our dark-matter-only simulations can complement their results

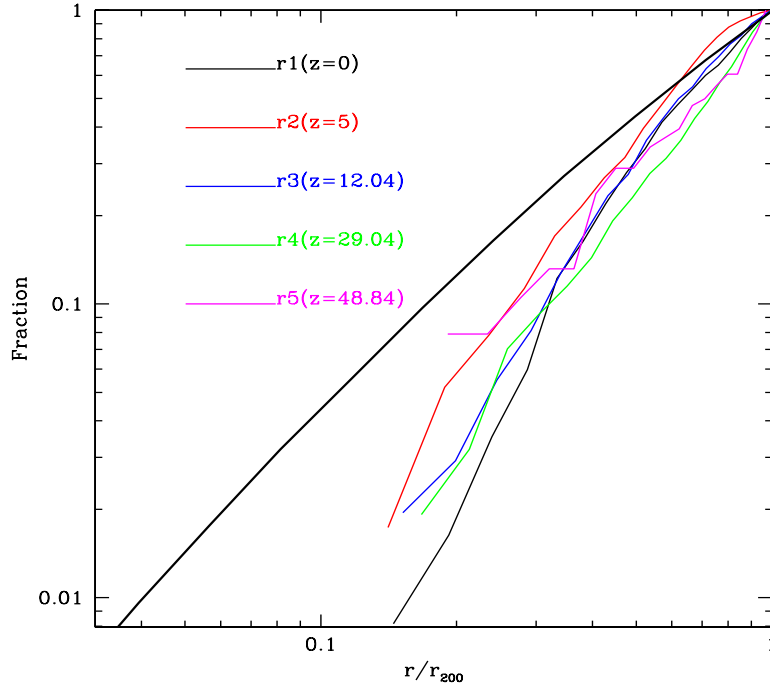


Figure 5.7: The cumulative spatial distribution of subhaloes containing least 30 particles within r_{200} for the final haloes of our sequence of simulations. The solid curve shows the total mass distribution in the $z = 0$ halo

to predict the formation time and also the abundance of the first stars.

In Fig. 5.8, we plot the M_{200} (top panel) and the virial temperature (bottom panel) of the most massive halo in the high resolution region of our sequence of simulations as a function of redshift. As can be seen from the top panel, the most massive halo resolved in our simulation has a virial mass of \sim a few $\times M_{\odot}$ at $z = 100$, $10h^{-1}M_{\odot}$ at $z = 80$, and $10^6h^{-1}M_{\odot}$ at $z = 45$. This last value corresponds to the smallest virial mass in which a star can form according to recent hydrodynamical simulations (Abel et al. 1998; Bromm, Coppi, Larson 1999; Yoshida et al. 2003). At $z \sim 26$ the most massive object has $10^8h^{-1}M_{\odot}$ corresponding to the least mass possible for the birth of a quasar (Bromm et al. 2003).

The thick line in the same plot is quite interesting. It shows the predicted mass accretion history for the R1 halo according to extended PS theory. It is remarkable that this prediction follows closely the mass of the most massive haloes in our sequence of simulations. There is at most a 10 per cent shift in the redshift direction at very early redshifts. We note that the most massive haloes don't become part of the final R1 halo. Examination shows that our R2 halo ends up as a halo of virial mass $\sim 10^{14}h^{-1}M_{\odot}$ at $z = 0$. At redshift $z = 5$, it is 15 per cent more massive than the most massive progenitor of the R1 halo. However, the R3, R4 and R5 haloes do end up as part of the R2 halo. Statistically, the most massive halo in the high resolution region of our simulations roughly tracks the whole

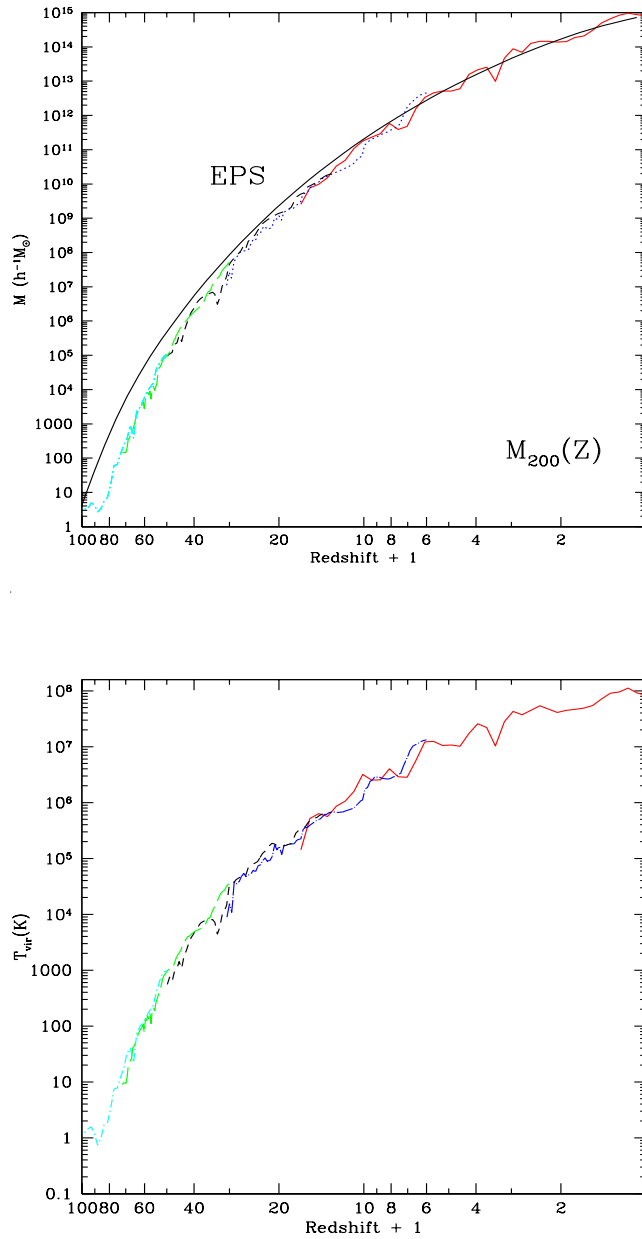


Figure 5.8: Top panel: mass of the most massive halo (define as M_{200}) in our sequence of simulations as a function of redshift. The solid line is the predicted mean mass of the most massive progenitor of the R1 halo according to extended PS theory. Bottom panel: the virial temperature (defined by using the maximum circular velocity) of the most massive halo in our simulations as a function of redshift.

mass accretion history of a rich cluster today, and is consistent with EPS theory.

Encouraged by the fact that the internal structure of dark matter haloes at high redshifts is quite similar to that of their low redshift counterparts, we estimate the virial temperature of dark haloes using the maximum circular velocity of the halo and assuming hydrostatic equilibrium:

$$T = 35.9(V_c/\text{km s}^{-1})^2\text{K} \quad (5.3)$$

The virial temperature of the most massive halo in the high resolution regions of our simulation as a function of redshift is shown in the lower panel of Fig. 5.8. A halo of virial temperature $\sim 2000\text{K}$ which is the critical temperature for the formation of the first stars suggested by current hydrodynamical simulations (Abel et al 1999, Bromm et al. 1999) collapses as early as $z = 42$. The critical temperature $\sim 10^4\text{K}$ for the effective cooling by atomic H is reached as early as $z = 35$.

Since we simulate special regions, it is important to know the global abundance of objects like those we study. As demonstrated in Fig. 5.3, EPS theory predicts halo abundance accurately at redshift $z = 48.85$ at least in high density regions. In Fig. 5.9 we show it works at $z = 30$ as well. Again, we apply conditional EPS equation (equation (1) and equation (2)) and compare it to the halo abundance in a spherical region with radius $30r_{200}$. The agreement is just as good as in Fig. 5.1. Thus, we conclude that EPS theory can be used to predict the abundance of dark haloes in dense regions over the redshift range $z = 30$ to $z = 50$. It is possible, of course, to compare EPS theory to the data at other redshifts in our simulations. However, a complete examination is out of the scope of this paper, where we are more interested in objects that collapse before redshift $z = 30$. These should host the first stars.

In Fig. 5.10, we plot the predicted abundance of massive objects in our simulations as a function of redshift over the range $[z = 29, z = 100]$ according to the PS formalism. The two thin solid lines give the number of haloes per $h^3(\text{Mpc})^{-3}$ equal to or more massive than the most massive halo in the high resolution region of our R4 and R5 simulations. Note that two effects are supposed to be responsible to the differences in this plot for the overlapping redshift range for the R4 and R5 simulations. Firstly, the most massive object in the two simulations can be different as noted in Gao et al. (2003), a massive halo at early times doesn't necessary evolve into a massive halo at later times. Secondly, the halo abundance at high redshift is very sensitive to mass, a small difference in mass can result in a large fluctuation in abundance.

It is interesting to know the abundance of the critical halo ($\sim 10^6 M_\odot$) able to host one of the first stars as a function of redshift. In Fig. 5.10, we show the number of haloes more massive than $10^6 M_\odot$ per comoving $h^3(\text{Mpc})^{-3}$. The abundance at high redshift is also sensitive to the initial linear power spectrum. In Fig. 5.10, we plot abundances according to two analytical transfer functions, those of Bond & Efstathiou (1987; BE) and Bardeen et al. (1986; BBKS), and according to the numerical one produced with CMBFAST. The last was used in our simulations. The prediction with the BE transfer function gives the smallest halo abundance, while the with BBKS transfer function give the largest. As can be seen, at fixed redshift, the dependence on transfer function can be as large as a factor 10; At fixed abundance, the difference can be 10 per cent in redshift. It is unclear yet which transfer function is more accurate on such small scales.

In order to compare the halo abundance with that at the present-day, we plot the

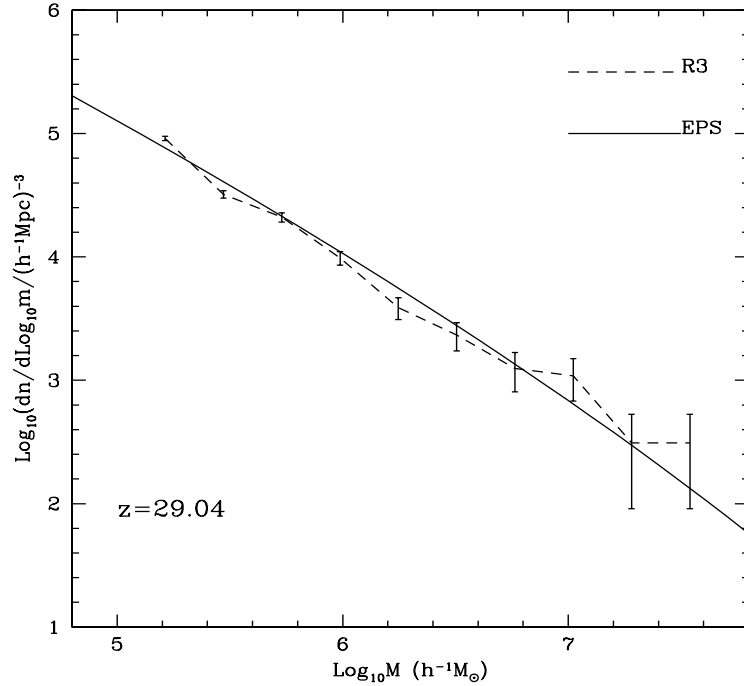


Figure 5.9: Differential mass function in a spherical region with radius $30r_{200}$ surrounding the most massive halo in our R3 simulation. The solid line is the prediction of conditional EPS theory. The error bars assumes Poission uncertainties in the counts for the R3 simulation

predicted $z = 0$ halo abundance as a function of halo mass (upper axis) in Fig. 5.10 as the thick solid line. Since the Sheth & Tormen mass function (Sheth & Tormen 1999; Sheth, Mo, Tormen 2001) is more accurate at low redshift (Jenkins et al. 2001; Reed et al. 2003; Gao et al. 2004), we compute this curve with the Sheth & Tormen formula. Comparing the abundance of critical haloes to this curve, haloes with mass $10^6 M_\odot$ at $z = 45$ which could probably house the first stars are as abundant as haloes of mass $\sim 10^{14} h^{-1} M_\odot$ today. By redshift $z = 40$ critical haloes ($\sim 10^6 M_\odot$) are as abundant as present “Milky Way” sized halo ($\sim 10^{12} M_\odot$), and by redshift $z = 30$ they are as abundant as present haloes of mass $M \sim 10^9 M_\odot$. This suggest that the first stars may be born before redshift $z = 40$. However, according to this plot, our simulation failed to find the rarest objects at high redshift with abundances similar to our R1 halo.

5.6 Concluding remarks

From repeated resimulation of the most massive halo in the high resolution regions of our sequence, we have succeeded in following realistically very massive rare haloes over the

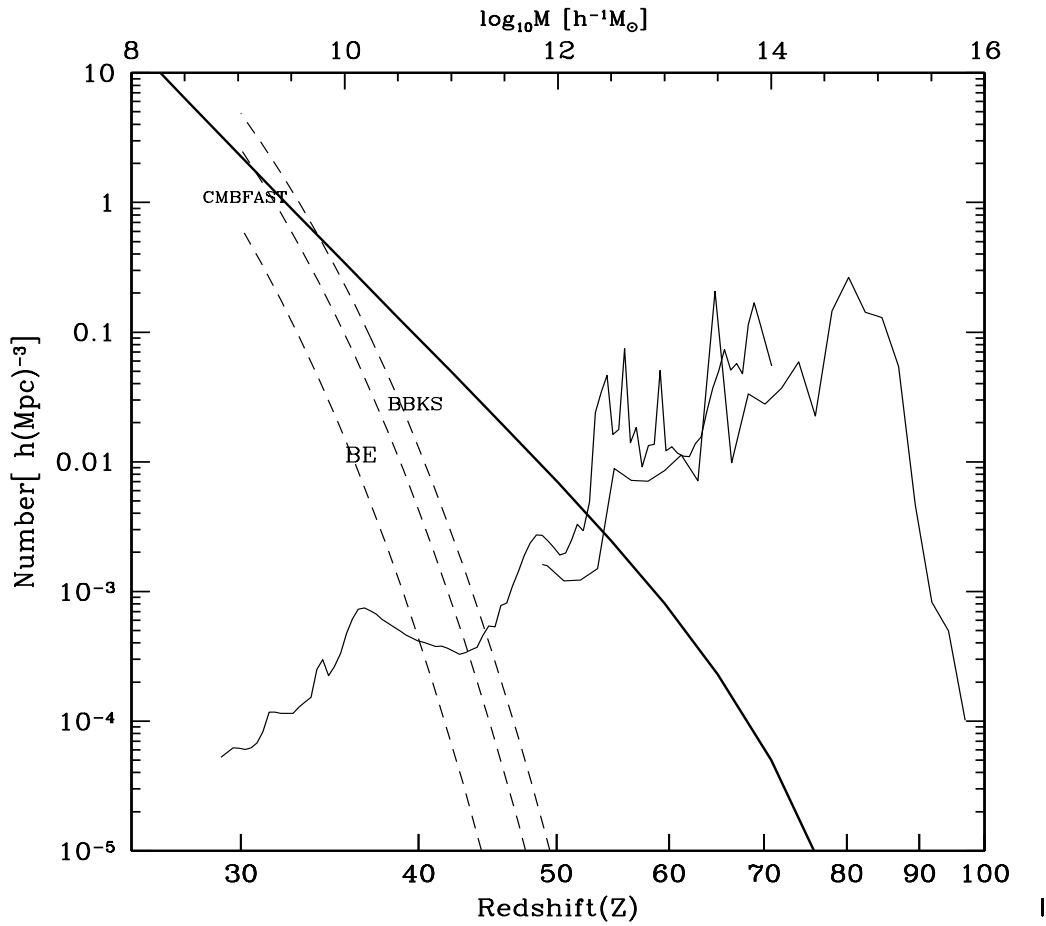


Figure 5.10: Thin solid lines: the PS-predicted abundance of haloes equal in mass to the most massive haloes in our R4 and R5 simulation as a function of redshift (bottom axis); Dashed lines: the abundance of the critical mass halo for star formation ($10^6 M_{\odot}$) as a function of redshift (bottom axis) estimated for three different transfer functions. Thick solid line: the abundance of haloes as a function of mass (upper axis) at $z = 0$

5 The first structures in a CDM Universe

range $z = 80$ to $z = 0$. Our results may be summarized as follows:

- (1) Structure formation at high redshift is extremely strongly biased to overdense regions, and the halo abundance in such overdense regions can be well reproduced by constrained Press & Schechter theory.
- (2) There is a strong trend for the strength of the filaments surrounding around a massive halo to increase with redshift.
- (3) The internal structure of dark haloes at high redshift is quite similar to that at low redshift. They are quite centrally concentrated. The properties of subhaloes within early haloes are also similar to their low redshift counterparts.
- (4) The inner slope of the density profile of haloes become shallower with redshift, while the concentration parameter c decreases with redshift.
- (5) Extended Press & Schechter theory is very accurate for predicting the halo abundance over redshift $z = 50$ to $z = 30$ in overdense regions.

In a Λ CDM universe, early massive dark matter haloes collapsed in large overdense regions. With realistic initial conditions, our simulations are able to resolve rarer and more massive haloes at any given redshift than previous work, even though we did not actually capture one of the rarest objects. The first stars should form earlier than previously thought. If the first stars did form in haloes with mass $10^6 M_{\odot}$, a large number density could be in place at $z \sim 42$.

Acknowledgements

The simulations used in this paper were carried out on Regattas supercomputer at the computing center of the Max-Planck-Society in Garching, Germany and on Cosma super computer at institute of computing Cosmology of University of Durham, England. GL thanks to Cedric Lacey, Yipeng Jing's useful discussion.

References

- Abel T., Bryan G., Norman M. L., 2000, *ApJ*, 540, 39
- Bardeen J. M., Bond J. R., Kaiser N., Szalay A. S., 1986, *ApJ*, 304, 15
- Barkana R., Loeb A., 2001, *Phys. Rep.*, 349, 125
- Barkana R., Loeb A., 2003, *ApJ* in press, preprint, astro-ph/0310338
- Bond J. R., Efstathiou, G., 1987, *MNRAS*, 226, 655
- Bond, J. R., Cole, S., Efstathiou, G., Kaiser, N., 1991, *ApJ*, 379, 440B
- Bromm, V., Larsen, R. B., 2003, preprinting, astro-ph/0311019
- Bromm, V., Coppi, P. S., Larson, R. B., 2002, *ApJ*, 564, 23
- Davis, M., Efstathiou, G., Frenk, C. S., White, S. D. M., 1985, *MNRAS*, 292, 371D
- De Lucia G., Kauffmann G., Springel V., White S. D. M., Lanzoni, B., Stoehr, F., Tormen, G., Yoshida, N., 2004, *MNRAS*, 348, 333D
- Diemand, J., Moore, B., Stadel, J., 2004, *MNRAS*, submitted, astro-ph/0403160
- Gao L., Loeb A., Peebles P. J. E., White S. D. M., Jenkins A., 2003, *ApJ*, submitted, astro-ph/0312499
- Gao L., White S. D. M., Jenkins A., Stoehr F., Springel V., 2004a, *MNRAS*, submitted, astro-ph/0404589
- Gao L., De Lucia G., White S. D. M., Jenkins A., 2004b, *MNRAS* submitted, astro-ph/0405010
- Ghigna S., Moore B., Governato F., Lake G., Quinn T., Stadel J., 2000, *ApJ*, 544, 616
- Fuller, T. M., Couchman, H. M. P., 2000, *ApJ*, 544, 6
- Jenkins A., Frenk C.S., Pearce F.R., Thomas P.A., Colberg J.M., White S. D. M., Couchman H. M. P., Yoshida N., 2001, *MNRAS*, 321, 372
- Kaiser, N., 1984, *ApJ*, 284L, 9K
- Lacey C., Cole S., 1993, *MNRAS*, 262, 627

References

- Lacey C., Cole S., 1994, MNRAS, 271, 676
- Mo H. J., White S. D. M., 1996, MNRAS, 282, 347
- Mo H. J., White S. D. M., 2002, MNRAS, 282, 347
- Moore B., Ghigna S., Governato F., Lake G., Quinn T., Stadel J., Tozzi P., 1999 ApJ, 524, 19
- Navarro J. F., Frenk C. S., White S. D. M., 1997, ApJ, 490, 493
- Power C., Navarro J. F., Jenkins A., Frenk C. S., White S. D. M., Springel V., Stadel J., Quinn T., 2003, MNRAS, 338, 14p
- Seljak U., Zaldarriaga M., 1996, ApJ, 469, 437
- Sheth R., Tormen G., 1999, MNRAS, 308, 119
- Sheth, R. K., Tormen, G., 2002, MNRAS, 329, 61S
- Smith, R. E., Peacock, J. A., Jenkins, A., White, S. D. M., Frenk, C. S., Pearce, F. R., Thomas, P. A., Efstathiou, G., Couchman, H. M. P. (The Virgo consortium), 2003, MNRAS, 341, 1311S
- Springel V., Yoshida N., White S. D. M., 2001a, New Ast. 6, 79
- Springel V., White S. D. M., Tormen G., Kauffmann G., 2001b, MNRAS, 328, 726
- White S. D. M., 1993, in schaeffer R., Silk J., Spiro M., Zinn-Justin J., eds, Cosmology and large Scale Structure, Les Houches Session LX. Elsevier, Amsterdam, P.77
- Yoshida N., Springel V., White S., Tormen G., 2000, ApJ, 544, 87
- Yoshida, N., Abel, T., Hernquist, L., Sugiyama, N., 2003, ApJ, 592, 645

Conclusion

Numerical simulation is a unique tool to explore the complexity of nonlinear systems. In this thesis, we use N -body simulations to study the formation and evolution of highly nonlinear objects in the “concordance” Λ CDM universe.

In Chapter 1, we review the most relevant theoretical framework for our studies.

The high resolution achieved by numerical simulation in recent years has allowed detailed study of the properties of the dark matter substructure (subhaloes) which is predicated by Cold Dark matter model. Since subhaloes are believed to be the carriers of galaxies, this topic has attracted increased interest both from theoretical (e.g numerical simulation) and observational (e.g. gravitational lensing) field. In Chapter 2, we use a large cosmological simulation and a variety of high resolution resimulations of individual cluster and galaxy haloes to investigate the systematic properties of subhalo populations. In contrast to the results of previous studies, we found that the subhalo populations of different haloes are not scaled copies of each other, but vary systematically with halo properties. On average, the amount of substructure increases with halo mass. At fixed mass, it decreases with halo concentration and with halo formation redshift. These trends are comparable in size to the scatter in subhalo abundance between similar haloes. Averaged over all haloes of given mass, the abundance of low mass subhaloes per unit parent halo mass is independent of parent mass. It is very similar to the abundance per unit mass of low mass haloes in the universe as a whole, once differing boundary definitions for subhaloes and haloes are accounted for. The radial distribution of subhaloes within their parent haloes is substantially less centrally concentrated than that of the dark matter. It varies at most weakly with the mass (or concentration) of the parent halo and not at all with subhalo mass. It does depend on the criteria used to define the subhalo population considered. About 90% of present-day subhaloes were accreted after $z = 1$ and about 70% after $z = 0.5$. In the mean, subhaloes accreted at $z = 1$ currently retain only about 8% of their original mass, those accreted at $z = 2$ only about 2%. Subhaloes seen near the centre of their parent typically were accreted earlier and retain less of their original mass than those seen near the edge. These strong systematics mean that comparison with galaxies in real clusters is only possible if the formation of the luminous component is modelled appropriately.

Chapter 3 is an extension of Chapter 2. In this work, we address the relation between subhaloes and galaxies by considering in detail the physical processes that regulate the baryonic evolution. In the past, the interpretation of subhalo abundance has been mostly based upon the current mass or internal structure of subhaloes without consideration of their history. This leads to some apparent contradictions between the predictions of Cold Dark Matter theory and the observations. We show in this chapter that there is no obvious contradiction but there is a rather complicated relation between subhaloes and galaxies. Thus the reported discrepancies are very likely due to inadequacies in the simple models

Conclusion

used, where the luminosity of the galaxy are simply related to the mass or (circular velocity) of the corresponding subhalo in a dark-matter-only simulation. As an example, we use a combination of 10 high resolution simulations of cluster-sized haloes and semi-analytic techniques to study the spatial distributions and the velocity dispersion profiles of galaxies and of dark matter subhalo. With reasonable assumptions about the evolution of the baryonic components, the radial distribution of model galaxies is in nice agreement with that of observed galaxies. We demonstrated that galaxies and subhaloes represent *different* populations and are not directly comparable. Evolution produces a complex and strongly position-dependent relation between subhaloes and their central galaxies. The relation can be properly modelled only by appropriate physical representation of the galaxy formation process.

In Chapter 3. we explore the assembly of the central cusps of Λ CDM haloes. In the Λ CDM cosmology, giant protogalaxies are present at redshift $z = 6$ with comoving number density (as a function of mass interior to ~ 10 kpc) that is comparable to the present number density of giant galaxies. The identity of the matter in their central regions is, however, predicted to change as major mergers bring together stars and dark matter from initially well separated sub-units. We use N-body simulations to show that these mergers push pre-existing matter outwards in the dominant galaxy, preserving the inner density profile of collisionless matter. It is plausible that the central regions of large galaxies end up dominated by stars formed in dense cores well before the last major mergers. The stability, or attractor-like, property of the collisionless matter distribution (stars and dark matter combined) under merging then suggests that the baryon loading which accompanies dissipative contraction and star formation may be erased as subsequent mergers drive the mass distribution back to a universal profile. Such suppression of the effects of baryon loading, along with the early assembly of the mass concentrations, may help resolve some apparent challenges to the CDM model for structure formation. It could in principle explain the observed absence of cusps in the central dark matter distribution of nearby galaxies and galaxy clusters.

In the final Chapter, we carry out a sequence of N -body resimulations of individual haloes at various redshifts within a *cosmological volume* $(0.68\text{Gpc})^3$ with the aim of resolving the first bound objects which could potentially host the first stars in a Cold Dark Matter dominated universe. Our simulations succeed in resolving rare but relatively massive haloes spanning a very broad redshift range [$z = 80, z = 0$] with ultra-high resolution. Our results indicate that initial structure formation was extremely strongly biased to overdense regions, and that this can be well understood within the framework of extended Press-Schechter(EPS) theory. The internal structure of these early haloes is quite similar to their low redshift counterparts, although the NFW profile does not fit as well. The halo mass function is examined at redshift $z = 50$ and $z = 30$. We find excellent agreement between the predictions and the simulations. Because our simulation volume is not a small periodic box we are able to simulate rarer and more massive halos at any given redshift than previous work. We find that bound-free cooling from atomic hydrogen can take place in haloes as early as $z = 32$ and that the comoving abundance of these halos is predicted to be the same as for $10^{14}h^{-1}M_{\odot}$ halos today. If the first stars did form in haloes with mass $\sim 10^6M_{\odot}$, a large number would be born already at $z \sim 45$ with a comoving abundance matching that of haloes with mass M_* today.

Acknowledgements

Thank you Simon, I enjoy working with you very much!

Thanks to Adrian Jenkins, without your numerous and timely correspondences, I would not have been able to finish this thesis.

Thanks to Volker Springel, Felix Stoehr, Gabriella De Lucia, Darren Croton, Manfred Kitzbichler and Lugi Iapichino for both help and friendship.

Thanks to Yipeng Jing, Gerhard Börner, and Houjun Mo for much advice and help.

Thanks to Carlos Frenk, Dorothy Jenkins, Chris Power for your hospitality during my visits to Durham

I am especially appreciative for all my Chinese friends I met in Garching: Shiyin Shen, Xiaohu Yang, Xu Kong, Xi Kang, Weipeng Lin, Donghai Zhao, Dongni Chen, Yi Fan and Guoling Li.

Thanks for the encouragment from my friend, Youming Li, and for the support from my parents and brothers. Lastly, thanks to my wife, Yaxing Xiong, and not just because of your wonderful cooking!